POLITECNICO DI TORINO

Master's Degree course
in Mechanical Engineering

Master's Degree Thesis

An adaptive and energy-maximizing control of wave energy converters using an extremum-seeking approach

Supervisor
prof. Giovanni Bracco
Co-supervisor
prof.ssa Giuliana Mattiazzo

Candidate
Luca Parrinello

Academic year 2019/2020

Ai miei genitori

Presentation

Renewable energy harvesting technologies have made tremendous progress over the last several decades, especially after the 1970s oil crisis, and are enabling us to reduce our current carbon footprint of energy production and consumption.

The most used and commercially successful forms of renewable energy harvesting are solar energy, wind energy, hydroelectricity, biomass, hydrogen and geothermal, [1]. Also, another source of renewable energy has lately seen a huge boost in its development: ocean/sea wave energy. Wave-energy conversion is one of the most promising renewable energy sources: seas and oceans occupy more than 70% of Earth's surface, and it is estimated that in terms of energy density, ocean waves give a much higher energy extraction potential than solar or wind. In terms of power density, it is calculated that ocean waves carry around 25 kW/m^2 if we consider a unitary wavelength and for 1 m of wave crest, against 1 kW/m^2 at peak insolation for solar energy or for wind at a speed of 12 m/s, [2] .

Although the unquestionable advantages of wave energy conversion, it is nowadays practically unexploited for harvesting energy from a commercial point of view: the farms in Portugal, UK, Australia and US are mainly used for experimental and research purposes, [3, 4].

Despite the fact that wave energy conversion is not a sufficient degree of maturity and economical viability, an important and concerted research effort is being made in order to achieve a commercial success. Also, the economy of scale model demonstrated for solar and wind farms, motivates future commercial wave farms. For example, the cost of a photovoltaic module dropped from \$66.1/W in 1976 to \$0.62/W in 2016. Similarly, the levelised cost of electricity generated from wind has significantly decreased over the years, with prices ranging from \$0.55/kWh in 1980 to \$0.05/kWh in 2012, [5]. Moreover, it is estimated that 2.11 ± 0.05 TW of wave energy is available globally, [6].

Nevertheless, significant progress has been made in the design and analysis of wave energy converter (WEC) devices, which convert the mechanical energy of the waves to a useful form of energy (usually electrical energy) through a power take-off (PTO) system, [7].

One of the challenging aspects of making wave energy commercially profitable is designing an optimal controller for a WEC device that maximizes its mean extracted power. Consequently, several optimal control formulations have been proposed in order to improve energy extraction from WECs. An extensive review on this topic can be found in Ringwood et al. [8, 9, 10].

ES is an adaptive control which tracks a maximum/minimum (extremum) of a performance/cost function and then drives the output of this function to its extremum [11].

The main advantages on using a model-free control law consist in the fact that there is no need to generate a model of the real device (which necessarily is a simplification of the actual device), therefore introducing an approximation on the description of the behavior of the WEC, especially when it comes to model the fluid-hull interaction. Also, a model-based control law should take into account the fact that the characteristics of the device may vary with time, due to the normal deterioration of materials in salt water, the growth of vegetation, or other reasons, and it is not possible to easily take into consideration these phenomena during the generation of the model. Another advantage of using an ES approach is that is not necessary to measure the parameters of the wave, since the force generated by the PTO can be obtained by measuring only the displacement and velocity of the oscillating body, which can be done much more easily. The main issue relative to the use of ES consists in the tuning of the controller parameters (although some of the methods used, as shown in the following of the text, have a relatively low number of parameters to tune). Another important aspect to consider when working with ES is the definition of the performance function, which is crucial for the functioning of the optimization algorithm.

Moreover, it is important to underline that an ES controller is causal, and for this reason, being only influenced by past and present information, does not require to predict the behavior of the wave in order to achieve an optimization. Also, a great advantage of ES is that it can be used directly on line, not having a computational high cost. Finally, our results demonstrate that ES achieves the optimization of the plant within a single simulation, whereas evolutionary strategies, which are also used in the problem of optimizing power extraction from WEC devices, typically require a large number of (possibly expensive) function evaluations.

ES control has been used for a variety of applications, including but not limited to, reducing thermo-acoustic instabilities in gas turbines and rocket engines [12], flight formation optimization [13], control of thermo-acoustic coolers [14], autonomous vehicles [15], and robots [16], and beam matching in particle accelerators [17]. ES control has also been widely used for wind [18, 19, 20], and solar power applications [21, 22, 23]. However, only a limited number of ES studies are available for wave energy in the literature [24, 25]. The aim of the current study is to fill this gap by testing different ES control algorithms and demonstrating their feasibility for WECs.

ES control was conceived at the beginning of the twentieth century by Leblanc [26]. The method first received considerable attention in the USSR in the 1940s [27], and then in the Western world in the 1950s and 1960s. Although ES was one of the first forms of adaptive control, it was not until 2000 that a proof of stability for a generic plant was provided by Krstić and Wang [11]. Soon after, many applications and variants of the algorithm followed in the literature. The first application of ES for WECs appeared in 2011 by Hals et al. [25], in which various control strategies, including tuning of controller parameters using perturbation-based ES were compared through simulation results. Hals et al. defined a performance function based on low pass filters and knowledge of wave excitation forces for tuning linear damping or the threshold value of latching, depending on the controller. The authors compared the controller parameters tuned through gain scheduling and ES strategies in their work [25]. In 2012, Garcia-Rosa et al. [24] used a discrete-time ES scheme to obtain performance-optimal PTO coefficients of a hyperbaric point absorber converter. In their simulation results, both reactive and resistive PTO coefficients were simultaneously optimized, without requiring the knowledge of wave excitation forces. Similar to Hals et al., the authors in [24] also used a perturbation-based ES control.

In this work, continuous-time ES control algorithms have been used to optimize the resistive and reactive PTO coefficients for a heaving submerged point absorber subject to regular and irregular waves. In particular, we test the sliding mode [28], relay [29], least-squares gradient [30], self-driving [31], and perturbation-based [11] ES schemes. The optimization results are verified against analytical solutions (for the *dry oscillator*) and the extremum of reference-to-output maps (for the submerged oscillating buoy). The numerical results show

that except for the self-driving ES algorithm, the other four ES schemes reliably converge for the two-parameter optimization problem, whereas the former is more suitable for optimizing a single-parameter. The results also show that for an irregular sea state, the sliding mode and perturbation-based ES schemes have better convergence to the optimum, in comparison to other ES schemes. The convergence of parameters towards the performance-optimal values are tested for widely different initial values, in order to avoid bias towards the extremum. We also demonstrate the adaptive capability of ES control, by considering a case, in which wave conditions are changed amidst the simulation, and the ES controller adapts to the new extremum automatically.

Finally, it is possible to summarize the contribution of the present study as follows: this study consist in a wide overview of different ES techniques available in literature, some of which have not been tested for WEC devices before, using a continuous-time approach, for a submerged WEC. Also, a novel definition for the performance function is provided, in order to ensure the effectiveness of the control law among different sea states.

Acknowledgments

I would like to thank my supervisor prof. Giovanni Bracco and my co-supervisor Giuliana Mattiazzo for giving me the great opportunity to work on such a fascinating field as wave energy conversion. A huge thanks goes to my hosting professor at San Diego State University, prof. Amneet Pal Bhalla, without whose advice, support and commitment it would not have been possible to conduct so successfully my research project.

Many thanks also to PhD student Panagiotis Dafnakis, who has provided all the materials needed for this study, and supported me patiently. I would also like to thank Kaustubh Khedkar and Ramakrishnan Thirumalaisamy, PhD students at SDSU, who gave a precious and valuable aid.

I would like to express my gratitude to Edoardo Pasta, with whom I shared my hardest times.

Finally, my deepest gratitude goes to my parents, who have always supported me, to my brother and my friends.

Contents

List of Figures

List of Tables

1. Renewable energy

The extraction of power from non-renewable energy sources, such as coal, oil or gas is still the principal form of energy production, but in the last decades, since the 1970s oil crisis, a crescent amount of resources has been invested into developing technologies that allow the exploitation of natural phenomena, including sunlight, wind, tides, waves, plant growth and geothermal heat, in order to collect energy. These natural sources of energy are also called renewable energy sources, meaning that, according to International Energy Agency [39], *energy is derived from natural processes that are replenished constantly. In its various forms, it derives directly from the sun, or from heat generated deep within the earth. Included in the definition is electricity and heat generated from solar, wind, ocean, hydropower, biomass, geothermal resources, and biofuels and hydrogen derived from renewable resources.*
The image reported in fig. 1.1 shows the worldwide consumption of energy classified by the source used to produce it from year 1965 to 2019.

It is possible to observe that the greatest amount of energy is produced using oil (33%), coal (27%) and gas (24%). The renewable energy contribution is mainly given by hydroelectricity (6.5%) and wind (2%), but the overall amount of energy produced using renewable sources amounts to about 10% (excluding nuclear energy, which is not renewable due to the fact that is based on the use of finite resources (uranium, plutonium, thorium) as nuclear fuel in the nuclear fission reaction).
Of course, the information reported in fig. 1.1 is only a synthesis of situations that vary from country to country, and may be quite different from one to another. For this reason in fig. 1.2 we report the energy consumption classified by source in two cases: USA and China. These examples have been chosen since these two countries have a great energy consumption and thus a great environmental footprint.

We have that the US energy extraction is mainly based upon the use of oil and gas, which are more available than coal. Moreover, these two fossil sources have a lower impact than coal on human health and environment. On the contrary, China makes wide us of coal, which is its primary source of energy.
On the other hand, it is possible to note that in the last years the Chinese impulse on using renewable energy sources is much greater than the American, especially on the hydroelectric field. It is also true that among all the forms of renewable energy, hydroelectricity is more strictly linked to the presence of suitable sites where to build a dam, and the number of these sites is limited.
Although the exploitation of non-renewable energy sources is still predominant, as we have just shown, some important issues related to this model are undoubtedly favouring the shift

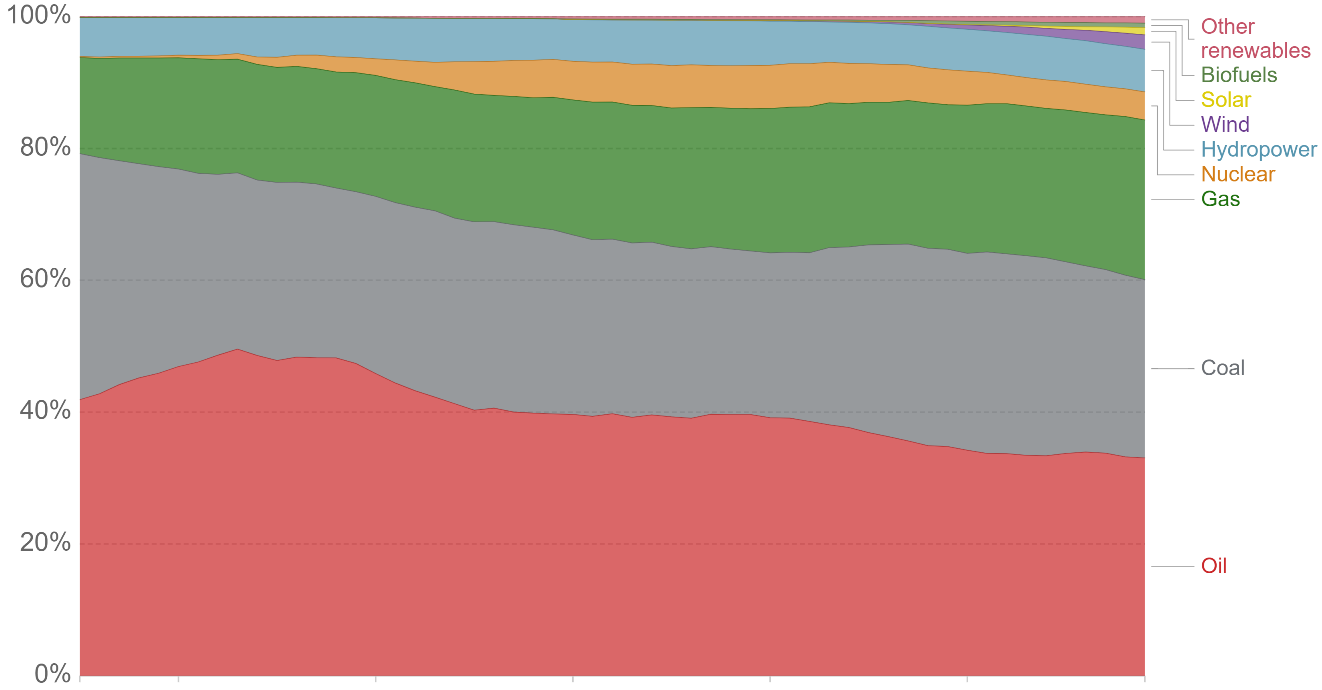

Source: BP Statistical Review of World Energy
Note: 'Other renewables' includes geothermal, biomass and waste energy.

OurWorldInData.org/energy • CC BY

Figure 1.1: Energy consumption by source: world. *Source: BP Statistical review of world energy [32].* Primary energy consumption is measured in terawatt-hours (TWh). Here an inefficiency factor (the 'substitution' method) has been applied for fossil fuels, meaning the shares by each energy source give a better approximation of final energy consumption.

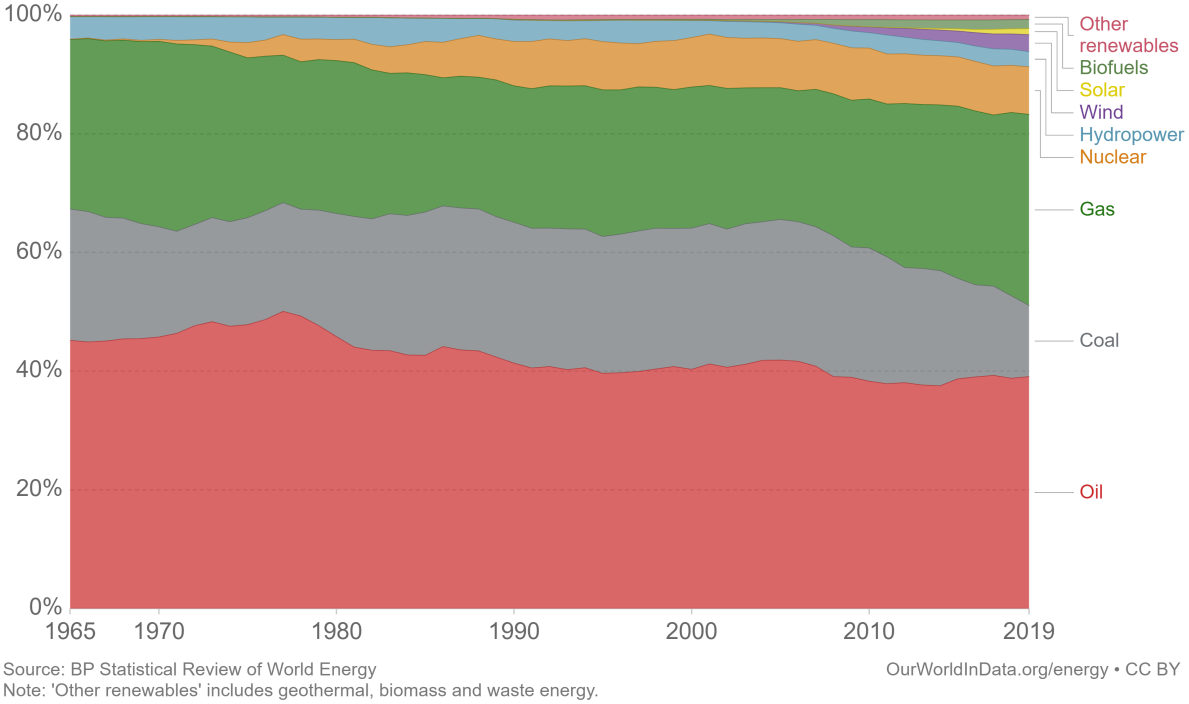

Source: BP Statistical Review of World Energy
Note: 'Other renewables' includes geothermal, biomass and waste energy.
OurWorldInData.org/energy • CC BY

(a) USA

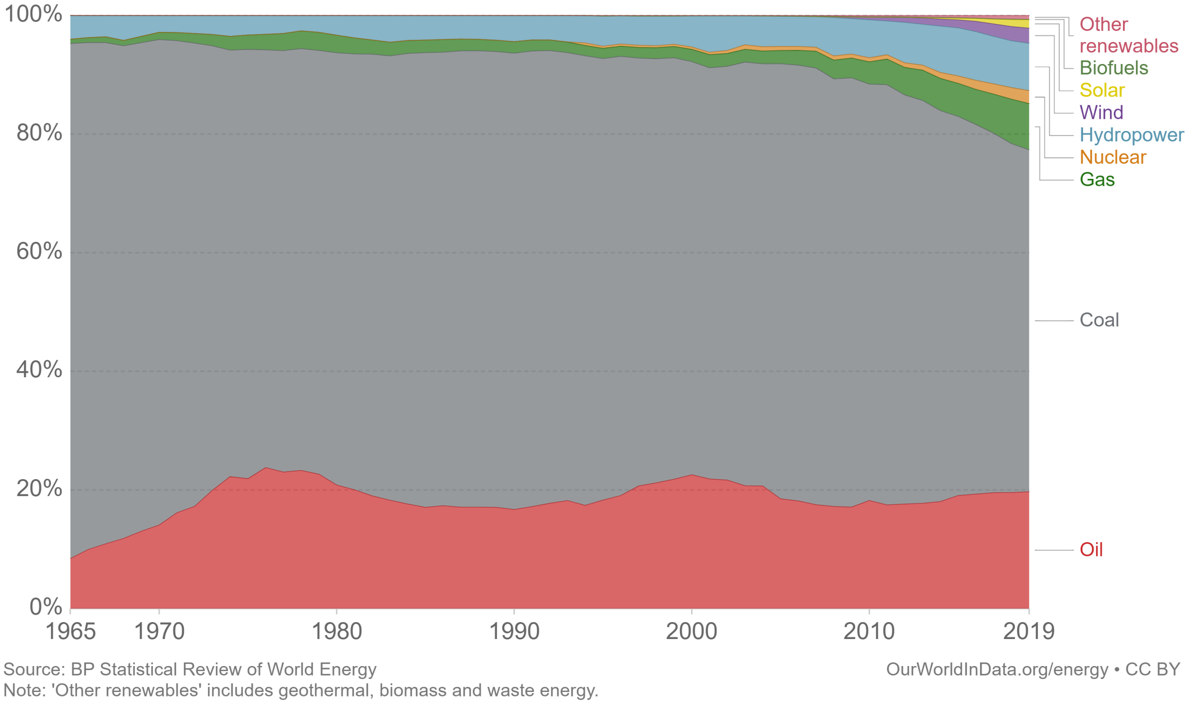

Source: BP Statistical Review of World Energy
Note: 'Other renewables' includes geothermal, biomass and waste energy.
OurWorldInData.org/energy • CC BY

(b) China

Figure 1.2: Energy consumption by source. *Source: BP Statistical review of world energy [32].* Primary energy consumption is measured in terawatt-hours (TWh). Here an inefficiency factor (the 'substitution' method) has been applied for fossil fuels, meaning the shares by each energy source give a better approximation of final energy consumption.

of the energy market to cleaner energy sources.
These issues related to the use of fossil energy sources may be summarized as follows:

- Fossil fuels are not renewable, meaning that their quantity is limited, and the formation of new deposits is really long. In fact, fossil fuels are predicted to run out in the next 50 years.
- Fossil fuels are responsible for environmental pollution. Some gas released during the combustion of these substances, such as carbon dioxide, known as greenhouse gases, lead to a rise in temperature of hearth, which leads to dramatic consequences including the melting of polar ice, the increase of the sea level, famine, desertification, etc. Also, some substances released during the combustion of fossil fuels are highly harmful to human health causing complications such as chronic asthma, low lung functioning, chronic bronchitis, cardiovascular diseases and carcinomas.
- Accidents involving fossil fuels, contrarily to the ones involving renewable energy sources, can be disastrous. For example, oil spills lead to the irremediable pollution of the coastlines and to the death of thousand of aquatic animals and birds, causing irreparable damage to the marine environment. Depending on the site of the accident, these accidents may lead to nefarious consequences also for humans, both for health and economy.
- Fossil fuels have highly variable prices and are susceptible to market manipulations. Also, being the deposits located only in certain areas, the control for these sources often leads to economical and political tensions. An advancement on the technologies that allows the exploitation of renewable energy sources may lead to lower price fluctuations and speculations. Also renewable energy sources, being related to natural phenomena such as sun, wind, etc., are available to a much larger number of countries.
- The coal power plants require huge amounts of raw materials in order to produce energy. This means that these materials need to be moved, possibly for long distance, contributing to the environmental impact of fossil fuels.
- Extraction and use of fossil fuels can be unsafe and lead to undesired consequences, including erosion, acidification of the environment, and destruction of wild lands.

On the other hand, renewable energy sources are acquiring an increasing importance and their performance is seeing a great improvement, also due to the tireless and promising research that is being conducted in the field.
The renewable energy exploitation begins in the last decades of 20th century, and has seen an important improvement in terms of efficiency and overall cost of the energy produced, especially for the technologies that utilize wind and solar energies. The global investment in renewable energies is constantly growing and has seen an important boost in the last couple of decades, as shown in fig. 1.3.

The figure shows that the increasing awareness of the public opinion, the international agreements for the decrease of the global warming (such as Rio 1992, Kyoto 1997 and Paris 2016) and the studies indicating the dangers of a temperature increase are leading to growing

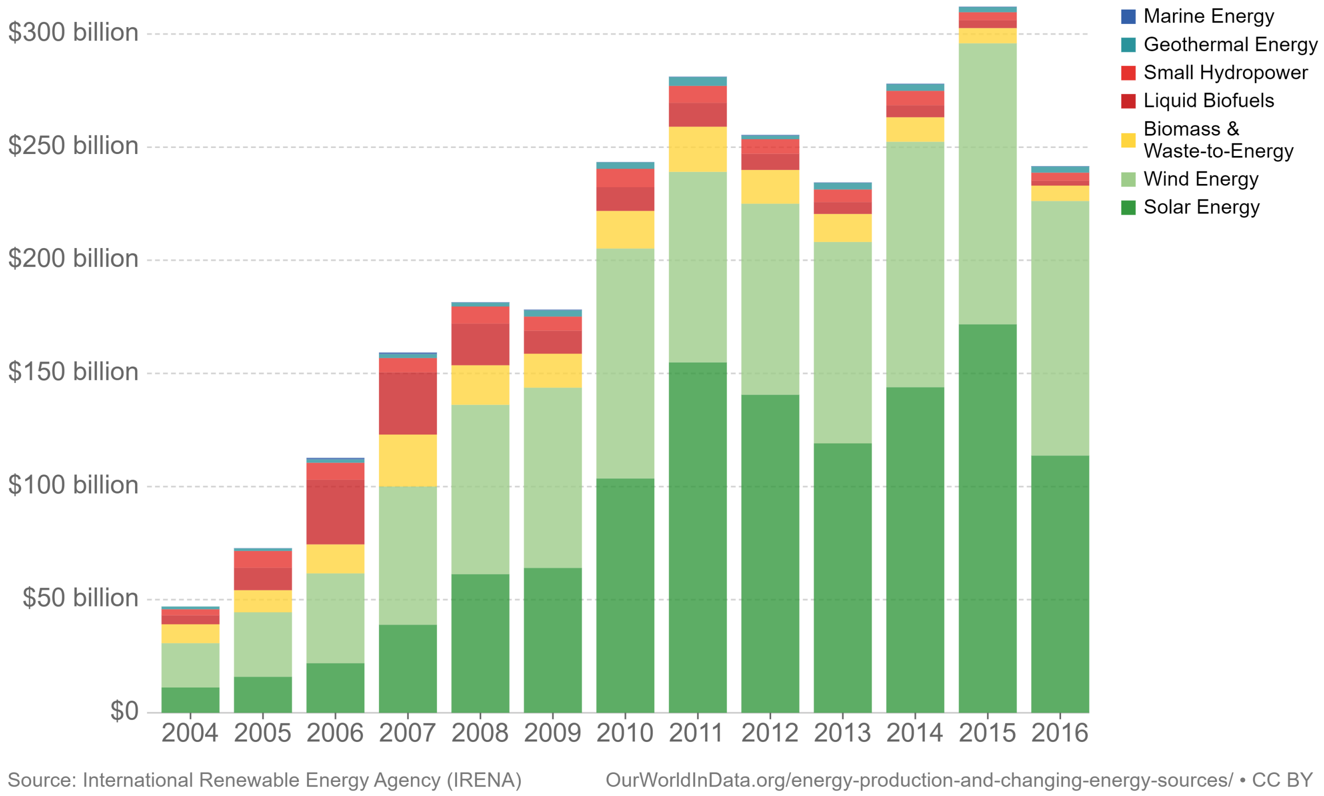

Figure 1.3: Global investment in renewable energy technologies measured in USD. Large hydropower plants are excluded. *Source: Frankfurt School-UNEP Centre/BNEF (2017). Global Trends in Renewable Energy Investment 2017* [33].

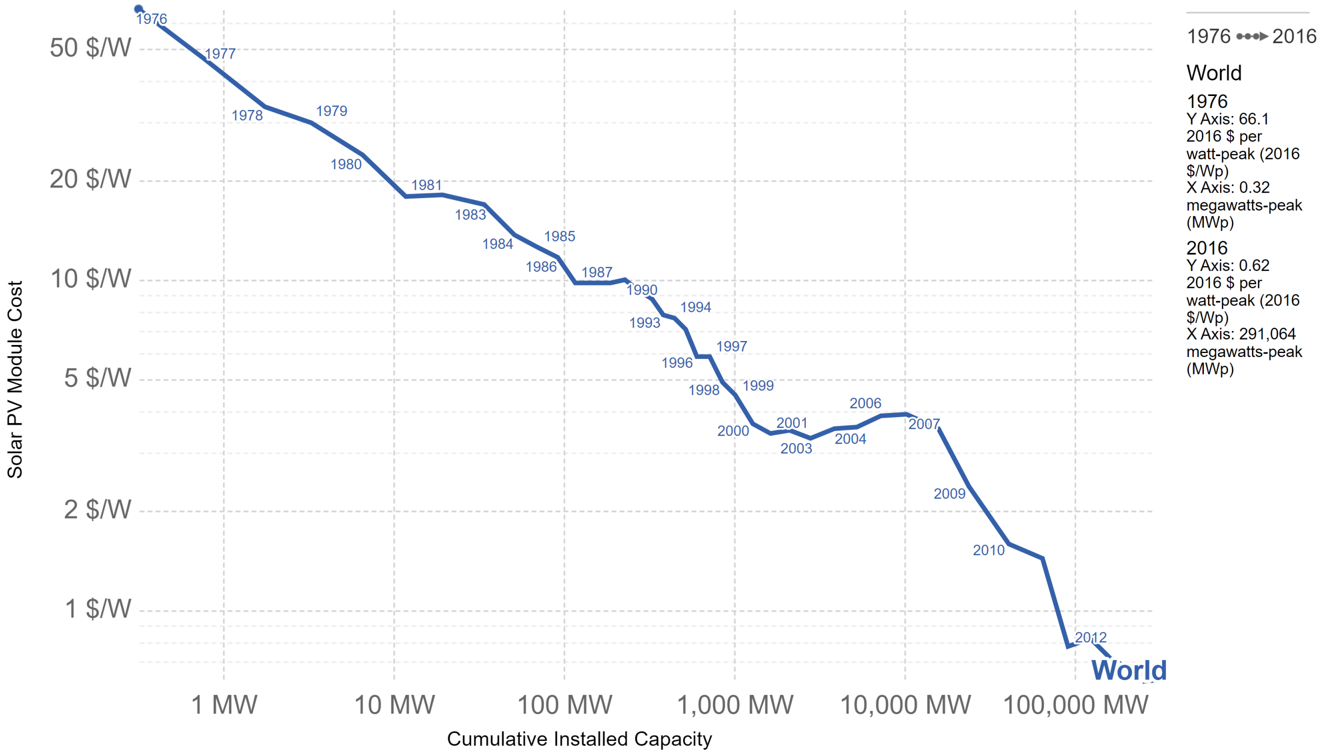

Source: Lafond et al. (2017); IRENA; SolarServer

OurWorldInData.org/renewables • CC BY

Figure 1.4: Cost of PV panels vs global installed capacity. *Source: Lafond et al. (2017). How well do experience curves predict technological progress? A method for making distributional forecasts.* [34]

investments in the field of renewable energies, especially in the wind and solar energies, that have reached a greater industrial and commercial maturity, allowing to reduce significantly the cost of energy.
On this matter, in fig. 1.4 we propose an analysis on the reduction of the cost of the energy produced using photovoltaic (PV) panels from 1976 to 2016.

It is possible to observe how the price of PV energy has decreased of about two orders of magnitude in the last 40 years. This curve, called *learning curve* is applicable to other technologies, for example wind energy, which data are not reported for brevity, but it is possible to state that the levelised cost of electricity generated from wind has significantly decreased over the years, with prices ranging from \$0.55/kWh in 1980 to \$0.05/kWh in 2012 [5].
This advancement on these two technologies is most likely related to the fact that the major investments are made in the fields of PV or wind energy. On the other hand, it is estimated that 2.11 ± 0.05 TW of wave energy is available globally [6]. And the power density of ocean waves is much higher than the power density of solar irradiation or wind: it is estimated that ocean waves carry around 25 kW/m^2 if we consider a unitary wavelength and for 1 m of wave crest, against 1 kW/m^2 at peak insolation for solar energy or for wind at a speed of 12 m/s, [2]. Another extimate, presented by McCormick [40], states that the power density

in ocean waves is 8.42 kW/m^2, while the wind power density generated by a wind of 10m/s is 0.58 kW/m^2 and the solar radiation has a power density of just 0.17 kW/m^2 at a latitude of 15° N.

Regardless of the estimate, we have that the power density of ocean waves is about 20 times larger than solar or wind energies. This consideration, combined with the fact that oceans and waves cover about 70% of the surface of earth, lead to an enormous energy potential contained in ocean waves, which is not yet exploited, due also to relatively low investments compared to other technologies (see fig. 1.3).

Before describing more in detail the field of *wave energy*, it is important to dwell on the advantages of using renewable sources for producing energy.

Briefly, the main advantages are:

- Renewable energy harvesting technologies exploit spontaneous natural phenomena to collect energy. Thus, the production of energy is not associated to the generation of polluting substances such as greenhouse gases, which are responsible for global warming or other undesired effects such as acid rains.
- Renewable energy sources do not deplete over time, as may happen to resources contained in natural deposits such as oil, coal or gas. This means that technologies based on the exploitation of renewable energy sources are more reliable in a long-time perspective, contrarily to the technologies based on the burnt of fossil fuels, that will become obsolete as soon as the combustibles will be depleted.
- Renewable energies are more widely available than fossil fuels, which deposits are located in specific areas. The major availability of renewable energy for a vast number of countries reduces speculations on energy and prevents economical and political tensions.
- Renewable energies lead to new job creation: experts affirm that with new countries embracing renewable energy sources, thousands of stable jobs will be created (see [41]).
- Renewable energy sources stabilize the energy market, since the cost of the energy produced is related mainly to the initial cost of installation, while an energy economy based on fossil fuels is subject to possibly high price fluctuations based on the current inflation and availability of the resource.
- Technologies based on the exploitation of renewable energy sources require a reduced amount of overall maintenance compared to traditional energy generators that use fossil fuels. PV panels or wind turbines, having less critical and stress-loaded parts, have lower costs for maintenance: this leads to a faster return of the investment and a reduced price of energy.
- Renewable energy sources are much less harmful to human health than traditional energy sources, since they drop substantially the generation of dangerous of noxious substances. The reduction of the number of people subject to diseases such as chronic asthma, low lung functioning, chronic bronchitis, cardiovascular diseases and carcinomas leads to a great reduction on sanitary expenses, that allow governments to make more profitable investments.

- Renewable energies, being available in wide areas, require a less complex infrastructure, since it is not necessary to reach remote areas from the energy production facilities. Energy can be produced locally. This also eliminates the transportation of raw materials (coal, gas, etc.) to the combustion plants, which contributes to the production of polluting substances.

- Over time, renewable energy technologies become cheaper with the improvement of the production and installation techniques. Also, renewable energies are available in many forms (solar radiation, wind, geothermal, etc.) so it is likely that in every area there is a possibility for producing energy using at least one of the existing technologies.

- For their availability, renewable energy sources can reduce the reliance on foreign energy sources.

- In certain cases renewable energy sources allow to recycle wasted products, as in the case of biomass energy. Also, it is possible to recycle components of solar panels or wind turbines, allowing multiple uses for the same materials.

- Accidents with renewable energy technologies are not as harmful as the ones involving fossil fuels (such as oil spills, explosions, etc.).

After having analyzed the general features of renewable energy, we focus on *wave energy*, on which this study is based.

1.1 Wave energy

The origins of the use of wave energy with modern technology date back to 1940, when Y. Masuda, a former commander in Japanese imperial Navy, developed a device which used the principle of the *oscillating water column*. For this reason, Masuda is regarded as the father of modern wave power technology.
It was not until 1963 oil crisis that wave energy gained new momentum with the work of S. H. Salter, who developed a device called the *Salter duck*, which was capable of converting 90% of wave motion into electricity, with a remarkable 80% efficiency (see Salter [42]).
After the oil crisis, when the price of oil decreased, the governments reduced drastically the funding for research in the wave energy field. Nevertheless, a first generation of devices had been already conceived and tested. Nowadays, with the increasing awareness of global warming and the raised attention towards the environment, new opportunities and a growing interest is given to the world of wave energy. Nevertheless, a huge gap with other renewable energy technologies such as solar or wind energies must be recovered.
In general, wave energy is derived from ocean or sea waves, where the motion of the free surface of the water contains a great amount of kinetic energy that can be converted into a commercially valuable form of energy (usually electrical). Waves are generated by wind blowing on the water free surface, transferring energy and producing waves of variable strength. Wind, in turn, is generated by differences of pressure in the atmosphere, due to the differences of temperatures in different parts of the globe, and also to currents, which are ultimately generated by the warming action of the sun. Thus, it is possible to affirm that wave energy

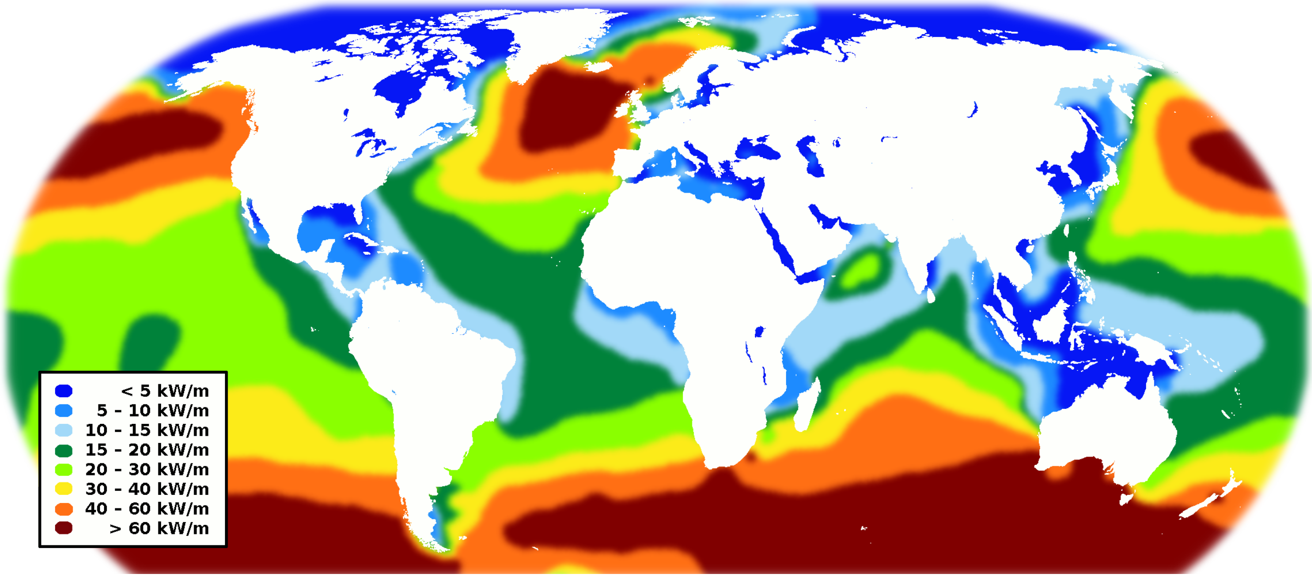

Figure 1.5: World map showing wave energy flux in kW per meter wave front. *Source: Ingvald Straume* [35]

is a form of concentrated energy produced by the sun.

Waves can be described with parameters like wavelength, wave height, wave speed, etc. In general the stronger the waves are, the more energy are capable to produce.

Waves observed in a specific site can be generated mainly in two ways: they can be generated far away from strong perturbations (*far-field waves*) or they can be formed by nearby weather systems (*near-field waves*). The former are usually long and regular, while the latter are usually shorter and irregular. The mathematical description of sea states is conducted in Sec. 3.3.

As previously stated, wave energy is highly available all over the world, and waves have a much higher power density than solar radiation or wind. This factors contribute to the rising interest in wave power, and justify the growing investment made in this field. For instance, the European Marine Energy Center (EMEC) was established in 2003 in Scotland, and has since then contributed to the development of new technologies capable of exploiting the energy of waves and tidal.

As said, the energy potential given by ocean/sea waves is about 2.11 ± 0.05 TW available globally [6]. Despite the considerable amount of available energy, its distribution is not homogeneous.

In fig. 1.5 is shown how the average power density of waves varies throughout the entire globe.

It is possible to observe that the locations with the most energy potential are the western seaboard of Europe, the northern coast of the UK, and the Pacific coastlines of North and South America, Southern Africa, Australia, and New Zealand. The north and south temperate zones have the best characteristics for wave power extraction. Also, in this sites the best period for energy harvesting is winter, when westerlies blow strongest.

Also, estimates have been made in order to evaluate how wave energy can contribute to

satisfy the energetic demand in different countries. For example, the National Renewable Energy Laboratory (NREL) has estimated that in the US wave power can contribute to generate about 1170 TWh per year, which is about 10 TWh per citizen, about 5% of the annual overall energy consumption of each citizen, including transport, heating, industry, etc.
On the other hand, about 50% of this energy would be extracted in Alaska, so there would be the necessity to install a proper infrastructure, nullifying some of the advantages of using a renewable form of energy.
NREL has shown that the technology used for collecting wave energy is capable of reaching an efficiency of 50%, which is much higher compared to the other technologies (such as solar or wind).

Together with the already discussed undeniable advantages of wave energy, there are also some important aspects regarding the environmental impact of such technologies on the marine environment.
Some of the aspects to consider are:

- the risk that marine animals are hit by underwater moving parts (such as turbine blades);
- the often unknown effects of the electromagnetic fields and noise generated by the devices operating underwater on fish and other animals;
- the physical presence of the devices themselves, which can alter life and behavior of marine animals, birds and fish either by attracting or repelling them;
- the effect of the presence of the devices on the transportation of sediments, substances or micro organisms;
- impact on human activities such as fishing or navigation;
- the effects of energy harvesting from waves, that may produce undesired effects on the shoreline or in coastal areas.

All of these aspects are currently being studied and solutions are being found in order to prevent or reduce drawbacks related to this technology, and also to reduce the cost of the energy and the investment necessary to build and place such devices.

2. Wave Energy Converters

In the course of the last decades, a number of devices that exploit the energy content of seas and oceans has been proposed. Seas and oceans contain energy in a great variety of forms: salinity or temperature differentials, tidal, marine currents and wave energy are among the most important. In this study we are going to focus on the conversion of the energy transported by waves.
A Wave Energy Converter (WEC) is a device capable of harvesting energy from the sea/ocean waves, converting it into a more useful or commercially valuable form of energy, usually electrical energy. Such devices make use of different functioning principles and present a wide variety of configurations.

Classification for site of installation

The first classification that is possible to operate, divides the device according to their site of installation. We have:

- **Onshore WECs:** which are built on shorelines. This kind of plants have a great impact on the environment since their construction requires the concreting of large sections of coastline both below and out of the water. Beside the environmental impact of the construction, these kind of plants often produce a very intense noise (given for example by the turbines that are used to produce energy) that can be detrimental for both fauna and people leaving nearby. Also, a great initial investment is associated to the construction of such plants.

- **Nearshore WECs:** which are placed in shallow waters near the coast. These devices are often submerged, so the visual impact on the shoreline is limited, but they may interfere with human activities such as fishing or navigation, and the energy harvesting from waves so close to the shore may have environmental implications that need to be further investigated.

- **Offshore WECs:** which are placed in the open seas or oceans. This type of devices can be both floating or submerged, but the distance from the shoreline eliminates the factor of the visual impact. Nonetheless, these devices may interfere with the life of sea birds or marine animals, and the mooring systems can damage the bottom of the sea if not properly conceived. Finally, these devices are subject to extreme weather condition and, especially if they are floating, they may suffer damages from severe perturbations.

Classification for functioning principle

Another classification that is possible to make, regards the functioning principle on which the device is based. The most common are:

- Oscillating water column: on this principle was based on of the first WECs conceived in the last century. Y. Masuda, regarded as the father of the modern wave energy technology designed the first device in the 1940s. This type of devices can be located onshore or in deeper water, offshore, and are characterized by the presence of an air chamber. The air in the chamber is compressed by the rising level of the water due to the waves: the swelling of the water forces the air through an air turbine in order to create electricity. The turbine can produce a great amount of noise, potentially harming birds and animals. Also, fish and other marine animals may be trapped inside the air chamber. For a schematic of the device in his onshore configuration refer to fig. 2.1(a).

- Oscillating wave surge converter: these devices are typically characterized by structure fixed on the seabed, and an oscillating part connected to the structure. Energy is collected from the relative motion of the oscillating part respect to the fixed structure. The oscillating part can be constituted by floats, flaps or membranes. The environmental issues of this kind of devices include the possibility of collisions, of artificial reefing on the fixed part, of the presence of electromagnetic fields underwater and the impact of energy harvesting in the transportation of sediments or micro organisms. Some of these devices use a parabolic deflector to focus the energy of the wave in the point of extraction. For a schematic of a typical oscillating wave surge converter, refer to fig. 2.1(b).

- Overtopping device: these type of devices are characterized by a long structure that uses waves to fill a water reservoir which is located to a higher position respect to the sea level. The potential energy of the water contained in the reservoir is then exploited by low-head turbines. This class of devices can be found either onshore or offshore. Environmental risks of these devices include the impact of the mooring system on the seabes and the organisms living in it, and the electromagnetic field produced. Other concerns regard the noise produced by the turbines and the effect of subtracting energy from the waves on the marine environment. For a schematic of an onshore overtopping device, refer to 2.1(c).

- Submerged pressure differential: this class of devices has been developer relatively recently respect to other WEC technologies. These devices use flexible membranes in order to exploit the difference of pressure at different locations below a wave. This pressure differential is then utilized in a closed power take-off (PTO) fluid system, producing a fluid flow that drives a turbine and then an electrical generator. The membranes are then used as a surface between the ocean and the PTO system. These membranes are characterized by a large rigidity and a low mass, allowing the frequency content of the waves to be fully transferred to the fluid of the PTO system. Moreover, membranes can be tuned in order to avoid excessive loads in case of unfavourable weather conditions or to tune the performance of the system for specific wave conditions. A submerged converter of this type can be placed both in midwater or on the seafloor, where the influence of the waves is attenuated. For this reason is opportune to find an optimal depth to place the device in order to find a trade-off between power extraction and the protection of the device. In fig 2.1(d)-(e) it is possible to observe two possible configurations of this wide class of devices: the first presents a fixed structure tethered to the seabed and an oscillating part that exploits the difference of pressure generated by the travelling waves, while the second presents a long flexible conducts on which the differential of pressure generated by the wave causes a water flux that passes through a low-head turbine on the bow of the device. This second type of device is also called *bulge wave*.

- Floating in-air converters: this class of devices offers an improved reliability since most of the machinery parts are located above the free surface of water, where they can be easily inspected and repaired. These kind of devices are characterized by a floating vessel with a damped pendulum which is tuned according to the incident wave characteristics. Some of these devices include turbines in compartments containing sloshing fresh water. The concernings regarding the use of such devices include the effect on marine animals, the presence of EM fields and the impact of the mooring system.

- Point absorber (PA) buoy: these devices float on the free surface of the ocean or are placed underwater. They can be placed both nearshore or offshore and are held in position by a mooring sustem connected to the seabed. The wave energy is absorbed by radiating a wave with destructive interference to the incoming waves (see Todalshaug [43]). A PTO system uses the movement of the buoy in order to extract energy. The production of electrical energy can be achieved via linear generators or via generators driven by mechanical linear-to-rotary converters or hydraulic pumps. EM fields generated bu such deices may be harmful for marine organism or seabirds, also the presence of floating devices may be cause of collisions or affect the behavior of fish and other species. Also, potential issues for marine environment may be related to the mooring system and the energy removed from the waves may affect the shoreline. Thus, the recommendation that sites remain a considerable distance from the shore. In fig. 2.1(f) it is schematized a floating PA.

- Surface attenuator: these devices behave similarly to floating point absorbers, but are constituted by a number of floating bodies connected to one another. This *chain* of floating bodies orients itself to the same direction of the incoming wave, and a flexing motion is generated by the waves on the system. This motion drives hydraulic pumps, ultimately generating electricity. Environmental issues are similar to the ones regarding the point absorbers, with the additional concern that animals can be pinched between the floating bodies. Fig. 2.1(g) reports the scheme of a surface attenuator.

- Rotating mass generators: these device are usually floating and are constituted by a vessel in which one ore more rotating masses are found. The coupling between the rotation of the mass and the movement of the hull produced by the waves lead to the generation of a gyroscopic torque, which is used by a rotary PTO to extract energy. The environmental issues are similar to the ones related to the point absorber. In fig. 2.1(h) is depicted the scheme of a rotating mass generator.

For the purposes of this study, we are going to consider a submerged PA, although it is conceivable to use ES algorithms for controlling other classes of devices.
Finally, after the description of the most common classes of WEC devices (see fig. 2.1), we are going to present more in detail the class of devices used for the purposes of the present study, the point absorber.

2.1 Point Absorber

A point absorber, as specified in the previous section, is an oscillating device that floats on the free surface of the water or beneath it. Such devices are able to absorb energy from every direction of the incoming waves, and can move according to three DOF: heave, surge and pitch, as shown schematically in fig. 2.2.

It is important to underline that the motion of the PA is described as a planar motion since the device is designed to have an axial symmetry along the vertical axis.
Moreover, for the purposes of our study, since the motion that generates practically all the collectable energy is the heaving motion, the PA has been modeled as a 1 DOF body (see Dafnakis et al. [44]).
A schematic of a PA is provided in fig. 3.2: in this case the PTO is assumed to be linear, following a proportional-derivative law for generating its force, as described in Sec. 3. Other PTO technologies exploit the motion of the buoy to compress a gas or a liquid contained in a tank, and then convert the fluid energy into rotational movement of the power generator. Regardless of the PTO technology, it is possible to conclude that the relative motion between the floating body and the fixed part is used to generate energy.
Point absorbers have nowadays reached a remarkable degree of maturity in terms of technology and commercial availability, although they have not already reached a wide diffusion, and are mainly used on research and experimental projects. One of the best known PA devices is probably PowerBuoy© developed by Ocean Power Technologies (OPT) [45]: this is a PA floating on the free surface of water, capable of generating up to 8.4 kWh/day, with an height of 13 m, a float diameter of 2.65 m and a weight of 8.300 kg.
Another PA device, called CETO, has been Australian Carnegie Wave Energy Limited [46]. CETO is a submerged PA that has already been tested in various sites all over the world, such as in the australian areas of Albany, Perth and Garden Island, and in Cornwall (UK).
Also, Wavebob Ltd. has developed a PA, called Wavebob [47], which consists of two oscillating structures controlled by a damping system that adjusts the system response according to predicted wave height, wave power and frequency. A semi-submerged tank filled with sea water provides the inertia to the system: the use of sea water to generate inertia allows to reduce significantly the cost of structural materials.
Some of the most important wave farm featuring PA devices, built for research projects are:

- Wave Hub, located off the coast of Hayle, UK. The hub was installed in 2010, and has

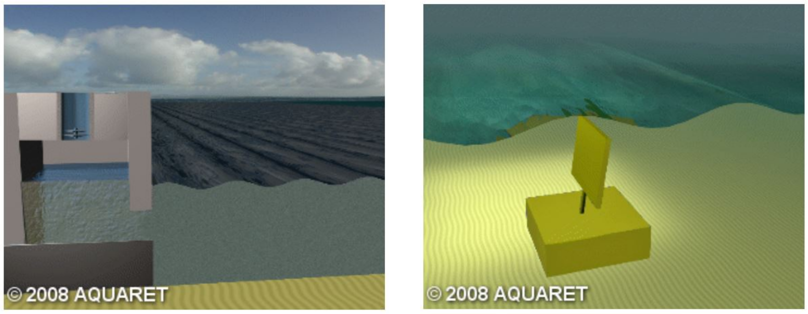

(a) Oscillating water column (b) Oscillating wave surge converter

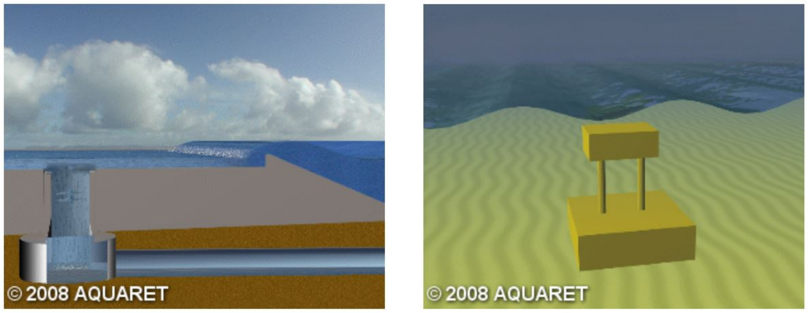

(c) Overtopping device (d) Submerged pressure differential 1

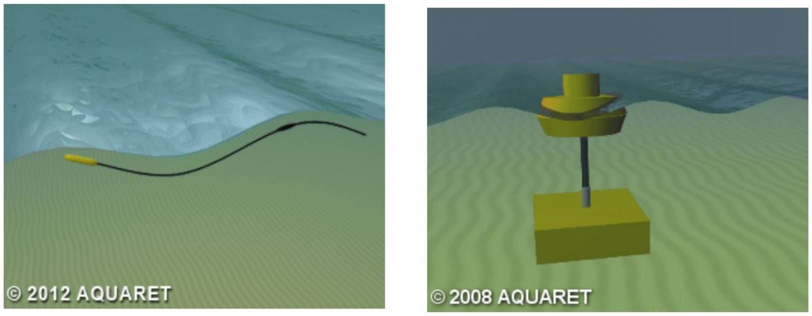

(e) Submerged pressure differential 2 (f) Point absorber

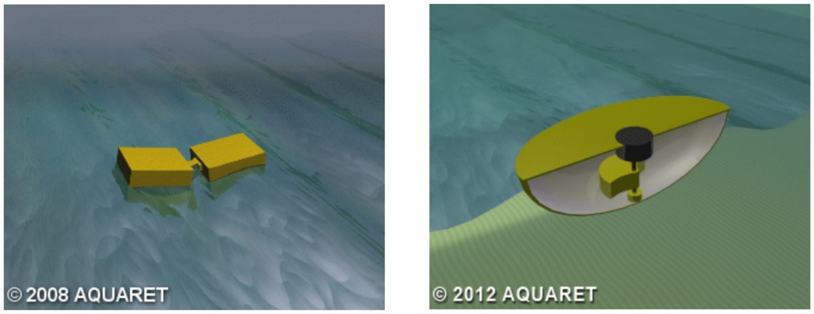

(g) Surface attenuator (h) Rotating mass generator

Figure 2.1: Schematics of some of the most common WEC devices. *Source: European Marine Energy Center (EMEC)* [36].

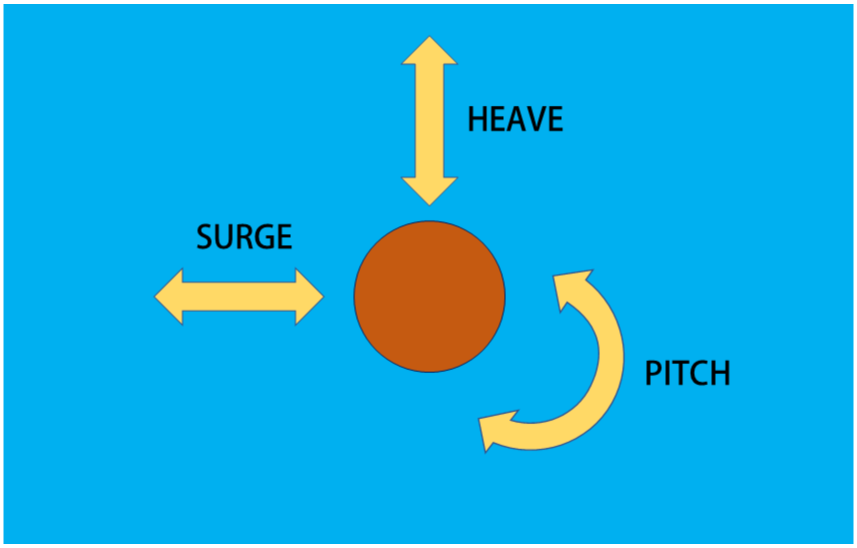

Figure 2.2: Schematics of the three DOF used for describing the motion of a PA.

a declared capacity of 20 MW. The estimated cost of the project is about £28 million (see [48]).

- HMAS Stirling naval base, located in western Australia, implements two fully submerged buoys capable of generating 2 MW. The project was started in 2015 for a cost of $100 million (see [49]).
- In Portland, Australia, a new 19 MW wave power has been funded AU$66.5 million from the Federal Government of Australia (see [50]).
- In Reedsport, Oregon, US, a 1.5 MW wave farm has been funded by the Federal government (see [51]).
- In Kaneohe Bay Oahu, Hawaii, US at Navy's Wave Energy Test Site (WETS) the Azura wave power device is currently been tested. The Azura wave power device is 45-ton wave energy converter located at a depth of 30 metres (98 ft) in Kaneohe Bay (see [52]).

The mathematical discussion of the behavior of a PA is conducted in Sec. 3.2. For an insight on the process of designing a PA, refer to Dafnakis et al. [53] and Pecher and Kofoed [54].

3. Mathematical models

In this chapter are discussed the equations describing the motion of energy-harvesting oscillators operating in air (dry oscillator) and in water (point absorber) environments.
Although the objective of the current work is to maximize the power extraction of point absorber devices using extremum-seeking control, it has also been decided to use the model of a dry oscillator. The purpose of studying such a system is the possibility to verify the convergence of the ES algorithms used; for this reason we have the necessity to test them for simpler systems, for which we are able to calculate analytically the optimal value of the plant input, and then confront the results of optimization via ES with the analytical values. In order to do so, it was necessary to model a system that was simple enough to consent a convenient analytical treatment, but maintain the main characteristics of the system we finally want to optimize through ES, this system being a Point Absorber Wave Energy Converter. Moreover, the analytical study allows to have a physical perspective of the power extraction optimization we aim to achieve.
The Point Absorber can be seen as a floating mass subject to a periodical force generated by incident sea/ocean waves. The movement of the mass is hampered by the hydrodynamic resistance given by water, which acts like a damper. If we consider a floating point absorber, it reaches its rest position when the gravity force given by its mass is balanced by the buoyancy force given by the submerged part of the hull. If the hull is moved from its equilibrium position, the buoyancy forces tend to return the mass into its original position, thus acting like a spring. If the Point Absorber is submerged, then the stiffness associated to the buoyancy forces is zero.
Moreover, we have that the point absorber is linked to a power take-off (PTO) by means of a mooring. The PTO exerts a force on the Point Absorber, and this force is used to extract power from the system, so it usually has a component related to the hull velocity. Another component of the force exerted by the PTO is related to the movement of the Point Absorber, thus being modeled as an additional stiffness of the system.
Given all the considerations made above, the natural simplification of the described system consists in a Mass-Spring-Damper system subject to a periodic external force, and connected to a PTO for power extraction.

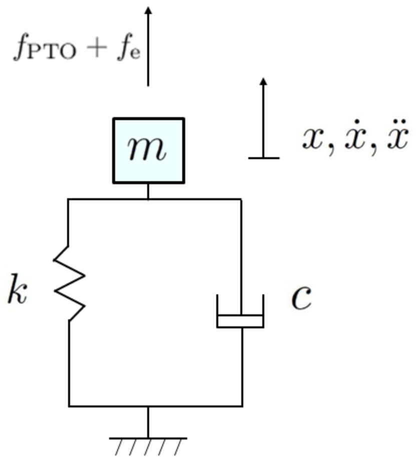

Figure 3.1: Schematic of an energy-harvesting mass-spring-damper system

3.1 Dry oscillator

The dry oscillator, or mass-spring-damper (MSD) system, can be schematized as shown in fig. 3.1.

The mass is subject to a deflection from its original position indicated by x, a velocity $\dot{x}$ and an acceleration $\ddot{x}$. The spring stiffness is indicated by k an the damping coefficient of the damper is c. One end of both the spring and the damper is linked to the mass, the other end is fixed.
Moreover, the mass is subject to an external force $F(t)$ which is due to both the sinusoidal perturbation and the PTO. We can then write

$$F(t) = f_{\mathrm{PTO}}(t) + f_{\mathrm{e}}(t). \tag{3.1}$$

Applying the Newton law $m\ddot{x} = \sum_i f_i$ to the system, in which $\sum_i f_i$ is the sum of the generic forces applied to the object and m is the mass of the object, we obtain the following equation

$$m\ddot{x}(t) + c\dot{x}(t) + kx(t) = F(t) = f_{\mathrm{PTO}}(t) + f_{\mathrm{e}}(t). \tag{3.2}$$

As previously discussed, the PTO force has a component which is responsible for the extraction of the power from the system, described as a damper, and a component related to the displacement of the mass, similarly to a spring. In general, as discussed in Bubbar and Buckham [55], the PTO force can also contain a component related to the acceleration of the body, in the form of $-A\ddot{x}$, defined as *inertance*. For the purposes of our study, this component has been neglected. We can then assume that the PTO force is given by

$$f_{\mathrm{PTO}}(t) = -C\dot{x} - Kx. \tag{3.3}$$

Equation (3.2) then becomes

$$m\ddot{x} + (c + C)\ \dot{x} + (k + K)\ x = f_\mathrm{e}(t). \tag{3.4}$$

This second order, linear differential equation with constant coefficients, describes the temporal behavior of the system. Not to lose the physical meaning of the description of the system, conditions $c + C \geq 0$ and $k + K \geq 0$ must be met.
The sinusoidal force can be generally described by $f_\mathrm{e}(t) = f_0 \sin(\omega t + \Phi)$, but for simplicity we choose to use a complex form $\bar{f}_\mathrm{e}(t) = \bar{f}_0 e^{i\omega t}$, with $f_\mathrm{e} = \Re\left(\bar{f}_0 e^{i\omega t}\right)$. $\bar{f}_0$ is in general a complex quantity, and is written as $\bar{f}_0 = \bar{f}_0(i\omega)$, and contains information about the amplitude and the phase of the force $\bar{f}_\mathrm{e}(t)$.
The deflection of the mass can equivalently written in the form $x(t) = \Re\left(\bar{x}(i\omega)e^{i\omega t}\right)$, with $\bar{x}(i\omega)$ containing information on both amplitude and phase of displacement. The frequency of displacement and the frequency of the external force are the same. We can then rewrite equation (3.4) in its complex form:

$$\left(-\omega^2 m + i\omega(C + c) + (K + k)\right) \bar{x}(i\omega)e^{i\omega t} = \bar{f}_0(i\omega)e^{i\omega t} \tag{3.5}$$

which being an equation relating the values of complex quantities, can be reduced to two equations: one regarding the amplitude and the other regarding the phase. Thus, we obtain

$$|\bar{x}(i\omega)| = \left|\frac{\bar{f}_0(i\omega)}{(K + k - \omega^2 m) + i\omega(C + c)}\right| \tag{3.6}$$

$$\tan\varphi = \frac{\omega(C + c)}{K + k - \omega^2 m} \tag{3.7}$$

being φ the phase delay of the displacement respect to the external force, and $|\bar{x}(i\omega)|$ the amplitude of the displacement oscillations.
The power supplied by the external force over one period $T = \frac{2\pi}{\omega}$ can be written as

$$P_\mathrm{in} = \frac{1}{T}\int_t^{t+T} f_e(t)\dot{x}(t)\ \mathrm{d}t = \frac{1}{2}\omega\left|\bar{f}_0\right||\bar{x}|\sin\varphi \tag{3.8}$$

while the power extracted by the PTO can be calculated as

$$P_\mathrm{out} = \frac{1}{T}\int_t^{t+T} C\dot{x}^2(t)\ \mathrm{d}t = \frac{1}{2}\omega^2 C\left|\bar{x}\right|. \tag{3.9}$$

Since the mass and the spring are not able to absorb energy, we can conclude that all the power supplied by the external force during the course of the period, is both dissipated by the damper and extracted by the PTO, possibly in different amounts.
From equation (3.8) we notice that the power supply to the system is maximum when $\sin\varphi = 1$, or equivalently, when the delay between the external force and the displacement is $\varphi = \pi/2$. This condition is reached when the system is in resonance with the external force, or its natural frequency ω_n equals the force frequency. In order to have the maximum supply of power to the system, taking into account also the influence of the PTO stiffness, we thus need to have

$$\omega_n = \sqrt{\frac{K+k}{m}} = \omega. \tag{3.10}$$

Although a substantial amount of research is conducted in the field of "geometry control" for the point absorbers, which aims to change the inherent characteristics of the system (see Bubbar et al. [56], Gradowski et al [57], Price et al. [58], Todalshaug et al. [59] and Tom et al. [60]), for the purposes of our study we focus on the optimization of the PTO parameters, an easy operation that can be conducted interfacing the controller with the driver of the PTO. Since in our case the inherent parameters of the system are constant, the PD (proportional-derivative) control law of the PTO allows the control designer only to adjust the reactive and resistive PTO coefficients K and C respectively, to optimize the system performance for varying external forces and disturbances.

Aiming to calculate the optimal values for the PTO coefficients, we can rewrite (3.10) in order to obtain the optimal value of the PTO stiffness:

$$K_{\text{opt}} = \omega^2 m - k. \tag{3.11}$$

Substituting (3.11) in (3.6) and (3.7), we obtain

$$|\bar{x}(i\omega)| = \frac{\left|\bar{f}_0(i\omega)\right|}{\omega(C+c)} \tag{3.12}$$

and

$$\varphi = \pi/2. \tag{3.13}$$

It is now possible to rewrite equation (3.9) according to (3.12), obtaining

$$P_{\text{out}} = \frac{C\left|\bar{f}_0(i\omega)\right|^2}{2(C+c)^2}. \tag{3.14}$$

Since our aim is to maximise the power extracted by the PTO, we can calculate the derivative $\frac{\mathrm{d}P_{\text{out}}}{\mathrm{d}C}$ and find the extremum point. We then have:

$$\frac{dP_{out}}{dC} = \frac{\left|\bar{f}_0(i\omega)\right|^2}{(C+c)^2}(C^2 - c^2) = 0 \tag{3.15}$$

which leads to the condition

$$C_{\text{opt}} = c. \tag{3.16}$$

It is important to notice that in the optimal conditions $(K_{\text{opt}}, C_{\text{opt}})$, the power extracted by the PTO equals the power dissipated by the damping.

Having obtained the optimal values of parameters C and K, it is possible to evaluate the performance of the ES methods.

For further insight on the topic, refer to Ringwood and Korde [61]. Finally, we remark that in some other optimal control formulations, for example in model predictive control of converters [62], the objective is to find the energy-maximizing control force f_{PTO} directly.

The average-power extracted by the system over a time period $\mathcal{T}$ is expressed as

$$\bar{P} = \frac{1}{\mathcal{T}} \int_{t}^{t+\mathcal{T}} -f_{\mathrm{PTO}}\, \dot{x}\, \mathrm{d}t. \tag{3.17}$$

For a PD control law, Eq. (3.17) is equivalent to Eq. (3.9)

$$\begin{aligned}\bar{P} &= \frac{1}{\mathcal{T}} \int_{t}^{t+\mathcal{T}} -f_{\mathrm{PTO}}\, \dot{x}\, \mathrm{d}t \\ &= \frac{1}{\mathcal{T}} \int_{t}^{t+\mathcal{T}} (Kx + C\dot{x})\, \dot{x}\, \mathrm{d}t \\ &= \frac{1}{\mathcal{T}} \int_{t}^{t+\mathcal{T}} K \frac{\mathrm{d}}{\mathrm{d}t}\left(\frac{x^2}{2}\right) \mathrm{d}t + \frac{1}{\mathcal{T}} \int_{t}^{t+\mathcal{T}} C\dot{x}^2\, \mathrm{d}t, \end{aligned} \tag{3.18}$$

as the first term in Eq. (3.18) vanishes under the time-periodic motion of the device. Appendix A.1 numerically verifies that the inclusion of the reactive component of power in the performance function, does not affect the final optimized values of PTO coefficients using ES. Therefore, we use only the resistive component of power or Eq. (3.9) for defining the performance function.

3.2 Point Absorber model

The Point Absorber, as discussed in the introduction to Chapter 3, can be seen as a floating mass subject to a periodic excitation due to the sea waves. The mass is also subject to a dissipation of energy due to the resistance provided by the water, known as drag force. The movement of the mass also produces perturbations on the fluid, generating waves: thus, part of the mass energy is lost in generating these waves. The mass is therefore subject subject to other dissipative forces called radiation forces. Finally the floating mass is linked to a power take-off (PTO), which is the responsible for the extraction of power from the system, being the extraction of power from the sea waves the main purpose of the system itself.

The PTO exerts a force which has the two components described in Sec. 3.1: one is proportional to the hull velocity, and is responsible for the extraction of power, while the other component is proportional to the displacement of the hull. The two components can therefore be modeled respectively as a damper and a spring.

Another aspect of the model is that while moving in the fluid, the body drags in its motion a certain quantity of the fluid, which has then an impact on the inertial behavior of the hull itself. For this reason an *added mass* due to the fluid has to be considered in the modelization of the problem.

Finally, it is important to underline that the hydrodynamic part of the model is resolved using the Potential Flow Theory, which is based on the assumption of irrotational flow of the fluid. This Theory allows to simplify the calculation of the hydrodynamic actions, which under suitable assumptions constitutes an acceptable approximation of the real flow of the fluid around the object.

The device can be schematized as shown in fig. 3.2.

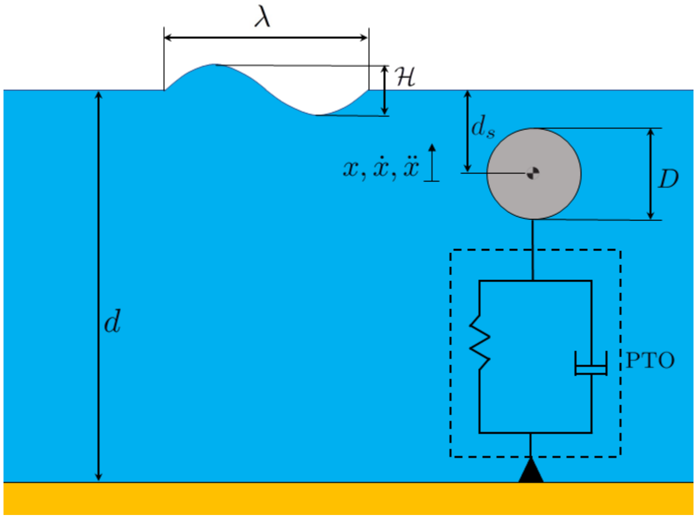

Figure 3.2: Schematic of a fully-submerged point absorber wave energy converter.

The equation of motion of a fully-submerged point absorber with a single degree of freedom (see Fig. 3.2) reads as

$$m\ddot{x}(t) = f_{\mathrm{w}}(t) + f_{\mathrm{r}}(t) + f_{\mathrm{v}}(t) + f_{\mathrm{PTO}}(t), \tag{3.19}$$

in which, m is the mass of the point absorber, f_{w} is the Froude-Krylov wave excitation force, f_{r} is the radiation force, f_{v} is the viscous drag force, and f_{PTO} is the PD control force applied by the PTO mechanism, as given in Eq. (3.3). The physical origin of radiation force stems from the energy dissipation mechanism of a moving body that emanates waves during its motion in water. Using the Cummins equation [63], the radiation force is expressed as

$$f_{\mathrm{r}}(t) = -A_{\infty}\ddot{x} - \int_0^t h_{\mathrm{r}}(t-\tau)\dot{x}(\tau)\,\mathrm{d}\tau, \tag{3.20}$$

in which, A_{∞} is the infinite-frequency added mass, and $h_{\mathrm{r}}(t)$ is the radiation impulse response function that contains the fluid-memory effect. The radiation force can also be obtained from the inverse Fourier transform of $H_{\mathrm{r}}(j\omega)$

$$H_{\mathrm{r}}(j\omega) = B(\omega) + j\omega\left(A(\omega) - A_{\infty}\right), \tag{3.21}$$

$$h_{\mathrm{r}}(t) = \frac{1}{\pi}\int_0^{\infty} H_{\mathrm{r}}(j\omega)e^{j\omega t}\,\mathrm{d}\omega, \tag{3.22}$$

in which, the frequency-dependent added mass $A(\omega)$, and the frequency-dependent radiation damping $B(\omega)$, can be obtained using boundary element method (BEM)-based codes like WAMIT [64] or ANSYS AQWA [65]. For computational efficiency, as well as for representational convenience, the radiation convolution integral in Eq. 3.20 can be approximated by an equivalent state-space formulation [66, 67]

$$k_{\mathrm{r}}(t) = \int_0^t h_{\mathrm{r}}(t-\tau)\dot{x}(\tau)\,\mathrm{d}\tau \simeq \begin{cases} \dot{\boldsymbol{\zeta}}_{\mathrm{r}}(t) = \boldsymbol{\mathcal{A}}_{\mathrm{r}}\boldsymbol{\zeta}_{\mathrm{r}}(t) + \boldsymbol{\mathcal{B}}_{\mathrm{r}}\dot{x}(t), & \boldsymbol{\mathcal{A}}_{\mathrm{r}} \in \mathbb{R}^{n_{\mathrm{r}}\times n_{\mathrm{r}}}, \boldsymbol{\zeta}_{\mathrm{r}} \in \mathbb{R}^{n_{\mathrm{r}}\times 1} \\ k_{\mathrm{r}}(t) = \boldsymbol{\mathcal{C}}_{\mathrm{r}}\boldsymbol{\zeta}_{\mathrm{r}}(t), & \boldsymbol{\mathcal{C}}_{\mathrm{r}} \in \mathbb{R}^{1\times n_{\mathrm{r}}} \end{cases} \tag{3.23}$$

in which, $\boldsymbol{\mathcal{A}}_{\mathrm{r}}, \boldsymbol{\mathcal{B}}_{\mathrm{r}}$, and $\boldsymbol{\mathcal{C}}_{\mathrm{r}}$ are the state-space matrices, and n_{r} is the approximation-order of $H_{\mathrm{r}}(j\omega)$ in the frequency-domain or $h_{\mathrm{r}}(t)$ in the time-domain. In this work, we also follow the state-space approach to approximate the radiation convolution integral. Combining Eqs. (3.19) and (3.23), the system of equations for the fully-submerged point absorber heaving in $x-$direction reads as

$$(m + A_\infty)\ddot{x}(t) + \boldsymbol{\mathcal{C}}_{\mathrm{r}}\boldsymbol{\zeta}_{\mathrm{r}}(t) = f_{\mathrm{w}}(t) + f_{\mathrm{v}}(t) - Kx(t) - C\dot{x}(t), \tag{3.24}$$

$$\dot{\boldsymbol{\zeta}}_{\mathrm{r}}(t) = \boldsymbol{\mathcal{A}}_{\mathrm{r}}\boldsymbol{\zeta}_{\mathrm{r}}(t) + \boldsymbol{\mathcal{B}}_{\mathrm{r}}\dot{x}(t). \tag{3.25}$$

The viscous drag force in Eq. (3.24) is modeled using a Morrison formulation as

$$f_{\mathrm{v}}(t) = -\frac{1}{2}\rho_{\mathrm{w}} C_{\mathrm{d}} S_x |\dot{x}|\dot{x}, \tag{3.26}$$

in which, $\rho_{\mathrm{w}} = 1025$ kg/m^3 is the density of sea water, C_{d} is the drag coefficient, and S_x is the planar cross-section area normal to the force.

3.2.1 Impedance-matching control for PA

As done for the *dry oscillator*, it is possible to calculate the optimal values of the PTO coefficients. This operation can be conducted only for a regular sea state (sinusoidal wave) and using a CFD approach, thus not being particularly useful for a system subject to a real sea state. Nevertheless, this theory is useful to evaluate the results obtained with the reference-to-output maps in the case of regular waves. This *maps* have been used to calculate the optimal values for the PTO parameters for both regular and irregular sea states.

In a regular sea, the point absorber system is mathematically equivalent to the mechanical oscillator of the previous section, if one replaces the damping coefficient c with the radiation damping $B(\omega)$, mass of the oscillator m with the total mass $(m + A(\omega))$, and the spring stiffness k with the hydrostatic stiffness k_{hydro}, which is zero for a fully-submerged body. Therefore, using the impedance-matching control theory, the energy-maximizing PTO parameters can be found as

$$K_{\mathrm{opt}} = \omega^2 \left(m + A(\omega)\right), \tag{3.27}$$

$$C_{\mathrm{opt}} = B(\omega). \tag{3.28}$$

We remark that if an additional viscous drag force is included in the equations of motion, as done in this work, then the optimal PTO resistive coefficient C_{opt} would be higher than $B(\omega)$, as shown by Beatty et al. [68], who introduce an equivalent drag coefficient $D(\omega)$ that is included in the calulation of C_{opt}. We make use of Eqs. (3.27) and (3.28) to verify the results of ES algorithms.

For an irregular sea state, the optimal PTO parameters cannot be found analytically as multiple frequencies are present in the point absorber velocity $\dot{x}$ (and other state variables), which is used to evaluate the $\bar{P}$ expression in Eq. (3.9). Therefore, to verify the optimal solution obtained from ES algorithms, we create a performance map of the system using a brute-force search of parametric space.

3.3 Wave models

In this section are discussed the models used to describe the sea states for regular and irregular sea states. The information regarding the temporal evolution of the wave profile obtained from the following sections is then utilized to calculate the time-series of the forces acting on the oscillating buoy, according to the formulation discussed in 3.4.

3.3.1 Waves for regular sea states

For regular waves, we indicate an ideal sea state characterized by waves having a sinusoidal profile, with a period $\mathcal{T}$, height $\mathcal{H}$ and wavelength η. Thus the wave profile can be expressed as

$$\eta(y,t) = a\cos(\kappa y - \omega t + \phi) \tag{3.29}$$

where κ is the wave number, calculated as $\kappa = 2\pi/\eta$, $\omega = 2\pi/\mathcal{T}$ is the wave angular frequency, ϕ is the wave phase and $a = \mathcal{H}/2$ is the wave amplitude. With y we indicate the coordinate of the direction of propagation of the wave, assuming that the wave propagates in the positive direction of y.

In this case, the power carried by the sinusoidal wave travelling in deep water is expressed by eq. (3.30), according to [42].

$$P_w = \frac{\rho g^2}{32\pi}\mathcal{H}^2\mathcal{T}\left[\frac{W}{m}\right]. \tag{3.30}$$

In eq. (3.30) the power is expressed per unit of crest length. Also, ρ is the density of the fluid and g is the gravitational acceleration.

The dependency of the available power on $\mathcal{H}^2$ leads to a wide variation of the power available depending on the sea state, while the range of variation of $\mathcal{T}$ is usually limited and depends on the geography of the site.

3.3.2 Waves for irregular sea states

Irregular waves describe in a more realistic way the sea states in which the system operates when installed. A way of modeling an irregular wave is by superposition of regular waves, as shown in eq. (3.31).

$$\eta(y,t) = \sum_{i=1}^{N} a_i cos(\kappa_i y - \omega_i t + \phi_i) \tag{3.31}$$

This equation is equivalent to a superposition of N regular waves, each described by eq. (3.29). Thus we have that every component of the irregular wave has an amplitude a_i, a wave number κ_i, a frequency ω_i and a phase ϕ_i. We also suppose that every phase ϕ_i is picked randomly in the interval $[0, 2\pi]$. In this case we have that the energy carried by the whole wave is given by the sum of the energies carried by every single component.
Moreover, if N tends to infinity, it is possible to define a continuous spectral density function $S(\omega)$, so the energy carried by the wave is associated to the area underlying the curve.
In order to generate the wave, a JONSWAP spectrum has been used, which leads to eq. (3.32).

$$S(\omega) = 320 \cdot \frac{\mathcal{H}_s^2}{\mathcal{T}_p^4} \cdot \omega^{-5} \cdot \mathrm{e}^{-\frac{1950}{T_p^4}\cdot\omega^{-4}} \cdot \gamma^A \tag{3.32}$$

where $\mathcal{H}_s$ is the significant wave height, and $\mathcal{T}_p$ is the period associated to the highest spectral peak. The peakedness factor γ is chosen to be $\gamma = 3.3$. The parameter A is given by

$$A = \mathrm{e}^{-\left(\frac{\frac{\omega}{\omega_p}-1}{\sigma\sqrt{2}}\right)^2} \tag{3.33}$$

where $\omega_p = 2\pi/T_p$ and

$$\sigma = \begin{cases} 0.07 & \text{if } \omega \leq \omega_p \\ 0.09 & \text{if } \omega > \omega_p \end{cases} \tag{3.34}$$

It is possible to express the amplitude a_i of each sinusoidal contribution to the spectrum as follows:

$$a_i = \sqrt{2S(\omega_i)\mathrm{d}\omega_i} \tag{3.35}$$

in which $\mathrm{d}\omega_i$ is the width of each frequency interval associated to ω_i in the discretization of the frequency domain.

In order to preserve the stability of the algorithms and reduce computational time, it has been chosen to eliminate from the spectrum the frequencies associated to very rare waves, and thus the very high wave frequencies and the close to zero frequencies. It can be shown that this simplification preserves the overall energy carried by the wave, thus not jeopardizing the validity of the study.

In this case it is possible to show that the power carried by the wave per unit of crest length is obtained as

$$P_w = \rho g \left(\int_0^\infty S(\omega) d\omega \right) c_g \approx \rho g \left(\sum_{i=1}^{N} \frac{a_i^2}{2} \right) c_g \tag{3.36}$$

in which c_g represents the group velocity, defined as

$$c_g = \frac{\lambda_s}{2T_p}\left(1 + \frac{2\kappa_s d}{\sinh(2\kappa_s d)}\right) \tag{3.37}$$

where the subscript s indicates the significant quantity of the spectrum, and d the water depth.
Finally, for deep water limit, we obtain

$$P_w \approx 0.49\mathcal{H}_s^2\mathcal{T}_p \left[\frac{kW}{m}\right] \tag{3.38}$$

which is approximately a half of the power carried by a regular wave characterized by the same value of height and period. For further analysis of the wave generation, refer to [69], [42].

3.4 Hull-fluid interaction

For the calculation of the interaction forces between the fluid and the hull, we can apply the effect-superposition, thanks to the fact that a linear theory has been used.
For this reason, we first focus on the calculation of the fluid-hull interaction for the case of a regular sea state, after which it is possible to solve the irregular wave case.
For the sinusoidal wave, the free surface profile is based on linear wave theory for a given wave height, wave frequency, and water depth. The regular wave excitation force is obtained from

$$F_{\text{ext}}(t) = \Re\left[R_f(t)\frac{\mathcal{H}}{2}\bar{F}_{\text{ext}}(\omega,\theta)e^{i\omega t}\right] \tag{3.39}$$

where $\Re$ denotes is the *Real part* operator, R_f is a ramp function which value grows linearly from 0 to 1 in a time interval t_{R}, $\mathcal{H}$ is the wave height, $\bar{F}_{\text{ext}}$ is the frequency dependent complex wave-excitation amplitude vector, and θ is the wave direction.
For irregular waves, the free surface elevation is constructed from a linear superposition of a number of regular wave components. Each regular wave component is extracted, as shown in Sec. 3.3.2, from a wave spectrum, (ω), which describes the wave energy distribution over a range of wave frequencies, generally characterized by a significant wave height and peak wave period. The irregular excitation force can be calculated as the real part of an integral term across all wave frequencies as follows

$$F_{\text{ext}}(t) = \Re\left[R_f(t)\sum_{j=1}^{N}\bar{F}_{\text{ext}}(\omega_j,\theta)e^{i(\omega_j t+\phi_j)}\sqrt{2S(\omega_j)\mathrm{d}\omega_j}\right] \tag{3.40}$$

where ϕ is the randomized phase angle and N is the number of frequency bands selected to discretize the wave spectrum. It is also possible to note that according to eq. 3.35, 3.40 can be rewritten as follows

$$F_{\text{ext}}(t) = \Re\left[R_f(t)\sum_{j=1}^{N}\bar{F}_{\text{ext}}(\omega_j,\theta)e^{i(\omega_j t+\phi_j)}a_j\right] = \Re\left[R_f(t)\sum_{j=1}^{N}\bar{F}_{\text{ext}}(\omega_j,\theta)e^{i(\omega_j t+\phi_j)}\frac{\mathcal{H}_j}{2}\right] \tag{3.41}$$

which structure is similar to eq. 3.39.

4. Extremum Seeking Control

The principle underlying the functioning of an ES algorithm is relatively simple: it aims to estimate how a performance function J varies when the parameters ϑ on which the function itself depends are varied. In other words, by means of varying the parameter ϑ, is possible to estimate the gradient of the function $J(\vartheta)$ and therefore use this information to maximize (or minimize) the value of the performance (cost) function, by varying ϑ according to the estimated value of the gradient of $J(\vartheta)$. In this work, we use *model-free* ES (also referred to as *black-box* ES) algorithms to enhance the power absorption of periodically oscillating systems, such as wave energy converter devices. The ES algorithms used in this work belong to the class of *derivative-based* optimization methods, which aim to determine the optimal value of the performance function J by estimating the derivative $\mathrm{d}J/\mathrm{d}\vartheta$, in order to obtain the value of the parameter ϑ^* which maximizes (minimizes) the performance (cost) function. Extremum-seeking control problems are typically formulated as unconstrained optimization problems, as done in this work and in prior works that used ES for WECs [24, 25]. In order to include inequality constraints on the plant parameters, the performance/cost function can be augmented with penalty functions [70, 71]. However, constraints on the state variables and performance indicators cannot be imposed in general, because the state of the plant and an explicit relationship between the plant parameters and performance indicators is not known a priori. Since a model-free ES algorithm is oblivious to the underlying system dynamics, its success depends upon the definition of the performance function, which the control designer is free to define. For energy harvesting systems, a natural choice of performance function is the amount of energy absorbed by the device over a period of time. An ES algorithm then finds the maxima of this concave (performance) function with respect to the PTO parameters.

4.1 Preliminary assumptions

Extremum-seeking (ES) control is an adaptive optimization technique that derives the values of the input of the controlled plant which maintain the plant output to its extremum, without requiring an explicit knowledge of the plant dynamics.

ES control can be applied to both linear and nonlinear systems, in which the extremum of a performance function is achieved and maintained by obtaining the gradient information with respect to the control inputs. For the purpose of description, we consider a single-input single-output (SISO) nonlinear system with the following characteristics:

1. an unknown dynamical plant $\dot{x} = f(x, u)$, with $x \in \mathbb{R}^n$ and $u \in \mathbb{R}$;

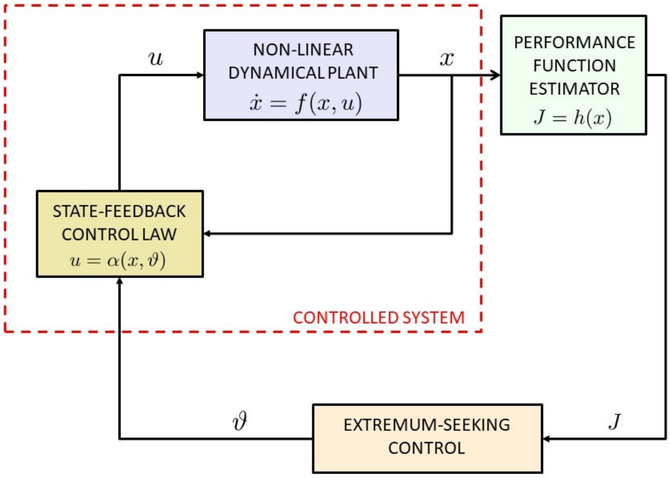

Figure 4.1: Extremum-seeking control scheme for a general SISO nonlinear system [37, 38].

2. a performance function $J = h(x)$, with $J \in \mathbb{R}$; and
3. a state-feedback control law $u = \alpha(x, \vartheta)$, with $\vartheta \in \mathbb{R}$.

Here, x represents the state of the plant, u is the control input, and J is the performance (cost) metric/function which needs to be maximized (minimized) over a period of time. The function $f(x, u)$ governing the evolution of the plant dynamics is not explicitly required for the ES algorithm. Fig. 4.1 shows a schematic representation of the plant with an embedded ES controller. The following assumptions are made for the extremum-seeking controlled plant [37, 72, 73, 28, 74]:

- **Assumption 1:** The control law $u = \alpha(x, \vartheta)$ is smooth, parametrized by ϑ, and stabilizes the plant.
- **Assumption 2:** There exists a smooth function $x_{\text{eq}}(\vartheta)$, such that

$$\dot{x} = f(x, \alpha(\vartheta, x)) = 0 \ \leftrightarrow x = x_{\text{eq}}(\vartheta). \tag{4.1}$$

- **Assumption 3:** The functions $f : \mathbb{R}^n \times \mathbb{R} \longrightarrow \mathbb{R}^n$ and $h : \mathbb{R}^n \longrightarrow \mathbb{R}$ are smooth.
- **Assumption 4:** The static performance behavior of the system at the equilibrium point $x_{\text{eq}}(\vartheta)$ can be expressed by

$$J_{\text{eq}} = h(x_{\text{eq}}(\vartheta)) = F(\vartheta), \tag{4.2}$$

  in which, $F(\vartheta)$ is a smooth function and admits a unique maximum or minimum at $\vartheta = \vartheta^*$.

- **Assumption 5:** The parameter ϑ evolves much more slowly than the dynamics of the plant; the latter is assumed to be in equilibrium (Eq. 4.1). Being the plant in equilibrium respect to the dynamics of ϑ, it is possible to neglect the dynamics of the plant in our analysis. This assumption leads to an optimization of the PTO parameters which does not take into account the fast dynamics of the wave, therefore leading to an "averaged" optimal value which is suitable for the whole periodical evolution of the wave, instead of searching for an "instantaneous" optimal value. Moreover, if the assumption of the plant equilibrium is not satisfied, meaning that the plant and the controller have a comparable time-scale, the stability and convergence of the control algorithm is not ensured. Given these operating conditions, we are aiming towards achieving a steady-state optimization of the plant. It then follows that the time derivative of the performance function of the *stabilized plant* can be expressed as

$$\dot{J}_{\text{eq}} = \frac{\mathrm{d}J_{\text{eq}}}{\mathrm{d}t} = \frac{\mathrm{d}J_{\text{eq}}}{\mathrm{d}\vartheta}\frac{\mathrm{d}\vartheta}{\mathrm{d}t} = \frac{\mathrm{d}F(\vartheta)}{\mathrm{d}\vartheta}\dot{\vartheta}. \tag{4.3}$$

Under the same set of aforementioned assumptions, it is also possible to extend the ES analysis to a multiple-input single-output (MISO) system, in which $\vartheta \in \mathbb{R}^m$. The objective here is to optimize m parameters simultaneously. For stability analysis of ES control of a SISO system, we refer the readers to Krstić and Wang [11], and of a MISO system, the readers are referred to [75, 76, 77, 78, 79, 15, 16].

4.2 Performance function definition

The performance/cost function defined for an ES algorithm should be time-invariant, and remain constant, if the parameter ϑ remains constant [31]. During the steady-state operation of a WEC device, the absorbed energy is a time-varying periodic function with a non-zero mean. Therefore, it is important to work with mean powers rather than instantaneous powers in the performance function, in order to satisfy Assumption 5 given in Sec. 4.1.

This observation can be used to define the mean of the absorbed power over a couple of wave periods. There are two advantages of using this definition: (i) firstly, it ensures that the device dynamics are much faster than the performance function variation; and (ii) secondly, ES control remains adaptive in presence of changing wave conditions. The adaptive capability of ES is maintained because typically the wave climate changes over several hundred wave periods, while the performance function is (re-)defined over the last few (wave) periods.

Specifically in this work, the performance function J for ES algorithms is defined to be a composite function of the instantaneous power $P(t)$ absorbed by the PTO unit as shown in Fig. 4.2. The composition consists of (i) a low-pass filter (LPF); (ii) a moving average defined over last few wave periods; and (iii) a logarithmic function. The signal $P(t)$, depending on the PTO machinery and on the formulation of the optimization problem, can be defined either as only the real (resistive) damping power captured by the PTO, or the sum of the two contributions given by the resistive power and the reactive power. The general purpose of the PTO optimization is to maximize the extraction of power from the system adjusting the coefficient related with the real (resistive) component of the power, while keeping the system response in resonance with the wave, by varying the coefficient related to the reactive part of the power.

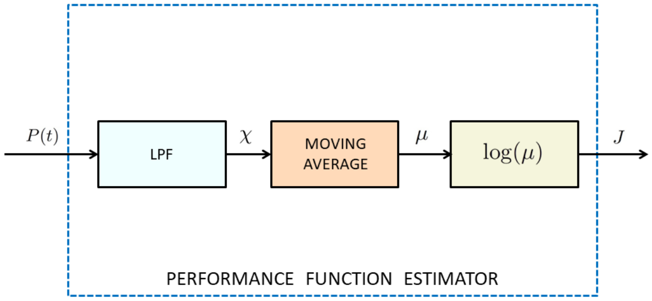

Figure 4.2: Block-diagram scheme to obtain the performance function J for ES algorithms using instantaneous power $P(t)$ absorbed by the PTO unit. A first-order low-pass filter of the form $\frac{\omega_\mathrm{L}}{s+\omega_\mathrm{L}}$ is used, in which ω_L is the cut-off frequency.

Irrespective of its definition, the power signal $P(t)$ is characterized by two main frequency contents: the first, which is at a higher value, is characterized by the fast dynamics of the plant itself, and the second, at a lower value, is characterized by the slow variation of the parameter ϑ provided by ES. The purpose of the low-pass filter is to eliminate the higher frequency content from the performance metric, while that of moving average is to evaluate the steady-state performance of the plant (see Haring [31] for more discussion). The signal μ which is the output of the first two operators, can be used to assess the device performance as a function of ϑ parameter. However, the plant or the device could be operating under wide variability of conditions (such as changing wave heights or periods), and the resulting power can vary in different orders of magnitude. As suggested by Ciri et al. [80], the purpose of the logarithmic function is to limit the variation of the performance metric drastically, which avoids re-tuning ES hyper-parameters for changing operating conditions of the plant. The drawback of using a logarithm is the reduced sensitivity of the response of the controller, but this can be nevertheless improved by a proper tuning of the controller parameters.

In fig. 4.3 is depicted how the signal representing the instantaneous power is elaborated according to the definition of the performance function, and how every operation impacts on the characteristics of the signal J used by the ES algorithms to optimize the performance of the plant.

The figure shows the different steps carried out while processing the signal of the instantaneous power $P(t)$: the low-pass filter (LPF) reduces drastically the oscillations of the signal $P(t)$, providing a signal which represents the DC component of the instantaneous power. Nevertheless, also the signal $\chi(t)$ presents important oscillations, since it is not possible to eliminate completely the oscillations from the original signal using a LPF without altering heavily (phase delay and attenuation) the original signal. Thus, has been chosen to regularize the behavior of the signal by eliminating any remaining frequency content related to the wave period: this is achieved by means of a moving average which covers the last

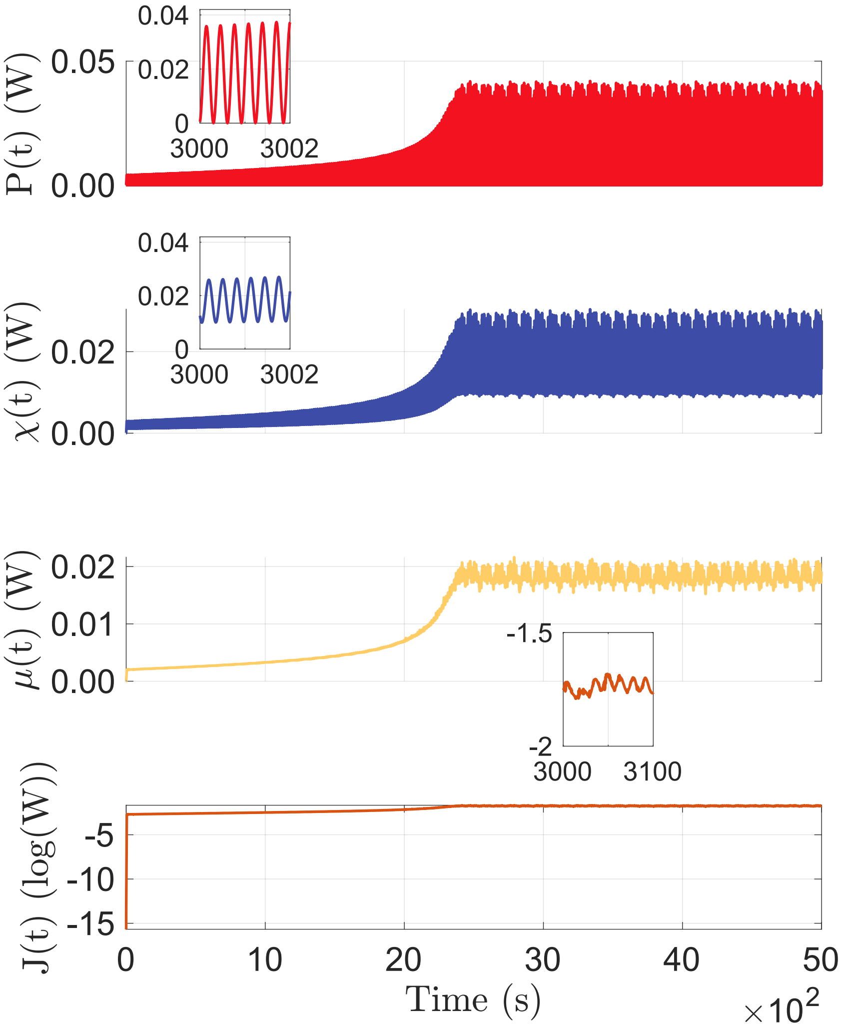

Figure 4.3: Analysis of the operations followed to obtain the performance function J for ES algorithms using instantaneous power $P(t)$ absorbed by the PTO unit.

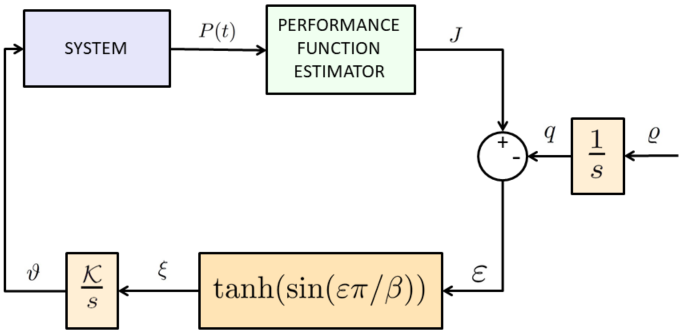

Figure 4.4: Block diagram of sliding mode extremum-seeking control system [28].

two periods of the wave. Finally, in order to eliminate any relation between the behavior of the optimizing algorithm and the conditions in which the system operates, the signal is processed through a logarithm, which normalizes the value of the performance function J. The signals shown are obtained for a cylindrical buoy in regular wave condition *Reg.1*, using the perturbation-based method (see the following of the text for further insight).

4.3 ES algorithms

In this section are discussed the different ES algorithms adopted in the present study in order to optimize the power extraction of the WEC device. For each algorithm a formal definition and the corresponding block-diagram is shown; it is then provided a stability study and finally some indications for the tuning of the parameters that characterize each algorithm.

4.3.1 Sliding mode ES

The sliding mode extremum-seeking control (SM-ES) is a nonlinear control method that by means of providing the plant with a suitable control signal, forces the system to move (or "slide") in a section of the state-space of the system. The state-feedback control law is not continuous in time, as it can switch from a continuous structure to another, based on the position of the system in the state-space. These control structures are designed so that the system can move from one region to another with a different control structure, *sliding* along the boundaries of the different regions. The Sliding Mode Extremum Seeking Control presents a structure that can be described as in Fig. 4.4.

Equivalently, the SM-ES can be described by the following set of equations:

$$\text{SM-ES} = \begin{cases} \dot{q} = \varrho, & \varrho > 0 \\ \varepsilon = J - q, & \\ \xi = \tanh\left(\sin\left(\varepsilon\pi/\beta\right)\right), & \beta > 0 \\ \dot{\vartheta} = \mathcal{K}\xi. & \mathcal{K} > 0 \end{cases} \tag{4.4}$$

Having defined the SM-ES, an analysis of its stability is provided.

Analysis of SM-ES

The stability of Sliding Mode ESC algorithm is discussed according to the studies conducted in [81, 28, 29].

In Fig. 4.4 the sliding variable $\varepsilon(t)$ is defined as

$$\varepsilon(t) = J(t) - q(y) \tag{4.5}$$

where $q(t)$ is a monotonically increasing function of derivative $\varrho = const > 0$. In order to use a more compact notation, the time dependency of the functions may be implicit in the following of the text.

The parameter ϑ is defined so that

$$\dot{\vartheta} = \mathcal{K}\ \tanh(\sin(\varepsilon\pi/\beta)) \tag{4.6}$$

being both $\varrho, \beta > 0$.

The derivative of the sliding variable is given by

$$\frac{\mathrm{d}\varepsilon}{\mathrm{d}t} = \dot{\varepsilon} = \dot{J} - \dot{q} = \frac{\mathrm{d}J}{\mathrm{d}\vartheta}\ \dot{\vartheta} - \varepsilon = \Phi\left(\vartheta\right)\ \mathcal{K}\ \tanh(\sin(\varepsilon\pi/\beta)) - \varrho \tag{4.7}$$

where $\Phi\left(\vartheta\right) = \frac{\mathrm{d}J}{\mathrm{d}\vartheta} = \frac{\mathrm{d}F(\vartheta)}{\mathrm{d}\vartheta}$.

If there exists a constant c such that the reaching condition

$$(\varepsilon - c)\frac{\mathrm{d}(\varepsilon - c)}{\mathrm{d}t} < 0 \tag{4.8}$$

is satisfied, then sliding modes will happen at $\varepsilon(t) = c$. When $\varepsilon(t) = c$, the performance function $J(t)$ increases with the increasing of the reference function $q(t)$, and the system moves towards the optimum point given by $\vartheta = \vartheta^*$.

According to trigonometric identities, it is possible to write

$$\sin\left(\frac{\pi}{\beta}\varepsilon\right) = 2\ \sin\left(\frac{\pi}{2\beta}\varepsilon\right)\ \cos\left(\frac{\pi}{2\beta}\varepsilon\right)\ . \tag{4.9}$$

We proceed defining the switching functions

$$\eta_l = \sin\left(\frac{\pi}{2\beta}\varepsilon\right) \tag{4.10}$$

and

$$\eta_r = \cos\left(\frac{\pi}{2\beta}\varepsilon\right)\ . \tag{4.11}$$

The sliding mode is

$$\frac{\varepsilon}{\beta} = \begin{cases} 2n, & \eta_l = 0 \\ 2n+1, & \eta_r = 0 \end{cases} \tag{4.12}$$

with $n \in \mathbb{Z}$, with $\mathbb{Z}$ set of integer numbers.

We first analyze the switching function η_l, which time-derivative is

$$\dot{\eta}_l = \frac{\pi}{2\beta} \cos\left(\frac{\pi}{2\beta}\varepsilon\right) \frac{\mathrm{d}\varepsilon}{\mathrm{d}t} = \frac{\pi}{2\beta}\eta_r \frac{\mathrm{d}\varepsilon}{\mathrm{d}t}. \tag{4.13}$$

It is then possible to write

$$\eta_l\ \dot{\eta}_l = \frac{\pi}{2\beta}\sin\left(\frac{\pi}{2\beta}\varepsilon\right)\ \cos\left(\frac{\pi}{2\beta}\varepsilon\right) \frac{\mathrm{d}\varepsilon}{\mathrm{d}t} = \frac{\pi}{4\beta}\sin\left(\frac{\pi}{\beta}\varepsilon\right)\ \ \left(\Phi\left(\vartheta\right)\ \mathcal{K}\tanh\left[\sin\left(\varepsilon\ \pi/\beta\right)\ \right]\ -\varrho\ \right) \tag{4.14}$$

From that we can conclude that

a) if $\sin\left(\frac{\pi}{\beta}\varepsilon\right)\ > 0$ and $\Phi\left(\vartheta\right) < \frac{\varrho}{\mathcal{K}}$, then $\eta_l\ \dot{\eta}_l < 0$

b) if $\sin\left(\frac{\pi}{\beta}\varepsilon\right)\ < 0$ and $\Phi\left(\vartheta\right) < -\frac{\varrho}{\mathcal{K}}$, then $\eta_l\ \dot{\eta}_l < 0$

In case a) we have $\dot{\varepsilon} \leq \Phi\left(\vartheta\right)\ \mathcal{K} - \varrho$ and $\Phi\left(\vartheta\right) < \frac{\varrho}{\mathcal{K}}$, so we get $\dot{\varepsilon} < 0 \iff \frac{\varepsilon}{\beta}\ \to 2n$.
In case b) we have $\dot{\varepsilon} \geq -\Phi\left(\vartheta\right)\ \mathcal{K} - \varrho$ and $\Phi\left(\vartheta\right) < -\frac{\varrho}{\mathcal{K}}$, so we get $\dot{\varepsilon} > 0 \iff \frac{\varepsilon}{\beta}\ \to 2n+2$.

We follow the same procedure for the switching function η_r, where we obtain

$$\dot{\eta}_r = -\frac{\pi}{2\beta}\sin\left(\frac{\pi}{2\beta}\varepsilon\right) \frac{\mathrm{d}\varepsilon}{\mathrm{d}t} = \frac{\pi}{2\beta}\eta_l \frac{\mathrm{d}\varepsilon}{\mathrm{d}t} \tag{4.15}$$

and

$$\eta_r\ \dot{\eta}_r = -\frac{\pi}{2\beta}\sin\left(\frac{\pi}{2\beta}\varepsilon\right)\ \cos\left(\frac{\pi}{2\beta}\varepsilon\right) \frac{\mathrm{d}\varepsilon}{\mathrm{d}t} = -\frac{\pi}{4\beta}\sin\left(\frac{\pi}{\beta}\varepsilon\right)\ \ \left(\Phi\left(\vartheta\right)\ \mathcal{K}\tanh\left[\sin\left(\varepsilon\ \pi/\beta\right)\ \right]\ -\varrho\ \right). \tag{4.16}$$

Similarly to the previous case, we can conclude that

c) if $\sin\left(\frac{\pi}{\beta}\varepsilon\right)\ > 0$ and $\Phi\left(\vartheta\right) > \frac{\varrho}{\mathcal{K}}$, then $\eta_l\ \dot{\eta}_l < 0$

d) if $\sin\left(\frac{\pi}{\beta}\varepsilon\right)\ < 0$ and $\Phi\left(\vartheta\right) > -\frac{\varrho}{\mathcal{K}}$, then $\eta_l\ \dot{\eta}_l < 0$

In case c) we have $0 < \dot{\varepsilon} \leq \Phi\left(\vartheta\right)\ \mathcal{K} - \varrho$ and $\Phi\left(\vartheta\right) > \frac{\varrho}{\mathcal{K}}$, so we get $\dot{\varepsilon} > 0 \iff \frac{\varepsilon}{\beta}\ \to 2n+1$.
In case d) we have $0 > \dot{\varepsilon} \geq -\Phi\left(\vartheta\right)\ \mathcal{K} - \varrho$ and $\Phi\left(\vartheta\right) > -\frac{\varrho}{\mathcal{K}}$, so we get $\dot{\varepsilon} < 0 \iff \frac{\varepsilon}{\beta}\ \to 2n+1$.

Trough the above analysis, all the sliding modes have been given. The convergence process can be divided into three stages as follows, depending on whether the system trajectory is in the sliding modes:

I Convergence stage: in this stage the system trajectory converges to the sliding mode form the initial value;

II Forced tracking stage: in this stage the system trajectory converges to the extremum point identified by $\vartheta = \vartheta^*$ while in sliding mode;

III Steady-state oscillation: in this stage the system trajectory remains at a vicinity of the extremum point with an oscillation. When the system reaches the optimum value, it can be shown [81, 28] that $\Phi(\vartheta) \in (-\varrho\mathcal{K},\ \varrho\mathcal{K})$

Proof of convergence for SM-ES

In this section is presented a proof of convergence for the sliding mode ES.

Theorem 1 *For a system which verifies all the assumptions made in section 4.1, controlled by the Sliding Mode Extremum Seeking Controller described, and given an initial condition* $\vartheta(t=0)$, *if the parameters* $\mathcal{K}$ *and* ϱ *satisfy*

$$|\Phi(\vartheta(\mathrm{t}=0))| \gg \frac{\varrho}{\mathcal{K}} \tag{4.17}$$

then one of the sliding surfaces

$$\begin{cases} \eta_l = \sin\left(\frac{\pi}{2\beta}\varepsilon\right) = 0, & \Phi(\vartheta(t)) < -\frac{\varrho}{\mathcal{K}}, \\ \eta_r = \cos\left(\frac{\pi}{2\beta}\varepsilon\right) = 0, & \Phi(\vartheta(t)) > \frac{\varrho}{\mathcal{K}} \end{cases} \tag{4.18}$$

must be reached in a finite time.

Proof: Since the sliding modes are described in two cases, we will prove the time-finite reachability, respectively when $\Phi(\vartheta(\mathrm{t}=0)) < -\frac{\varrho}{\mathcal{K}}$ and when $\Phi(\vartheta(\mathrm{t}=0)) > \frac{\varrho}{\mathcal{K}}$.

We first consider $\Phi(\vartheta(\mathrm{t}=0)) < -\frac{\varrho}{\mathcal{K}}$, and prove the finite-time reachability of sliding modes $\eta_l = 0$.

We remember that

$$\eta_l\ \dot{\eta}_l = \frac{\pi}{4\beta}\left|\sin\left(\frac{\pi}{\beta}\varepsilon\right)\right|\ (\Phi(\vartheta)\ \mathcal{K}\tanh(\sin(\varepsilon\ \pi/\beta)\ ) - \varrho) = -\frac{\pi\delta}{2\beta}\left|\sin\left(\frac{\pi}{2\beta}\varepsilon\right)\right|\left|\cos\left(\frac{\pi}{2\beta}\varepsilon\right)\right| \tag{4.19}$$

where $\delta(t) = -\Phi(\vartheta)\ \mathcal{K} + \varrho\tanh(\sin(\varepsilon\ \pi/\beta)\ ) > 0$.

Proceeding, we obtain

$$\eta_l\ \dot{\eta}_l = -\frac{\pi\delta}{2\beta}\left|\eta_l\right|\sqrt{1-\eta_l^2} < -\frac{\delta}{\beta}\left|\eta_l\right|\sqrt{1-\eta_l^2}. \tag{4.20}$$

If we define a function V such that

$$V = \frac{1}{2}\eta_l^2 < \frac{1}{2} \tag{4.21}$$

the derivative of V is

$$\dot{V} = \eta_l\ \dot{\eta}_l < -\frac{\delta}{\beta}\ \sqrt{2V}\sqrt{1-2V}, \tag{4.22}$$

which is equivalent to

$$\frac{\dot{V}}{\sqrt{2V}\sqrt{1-2V}} < -\frac{\delta}{\beta}. \tag{4.23}$$

If we assume that the initial condition is $V(0) = V_0$ and at the moment $t = T$ the sliding modes are reached, and that $\frac{\varrho}{\mathcal{K}}$ is small enough to satisfy $\left|\Phi\left(\vartheta\left(\mathrm{T}\right)\right)\right| > \frac{\varrho}{\mathcal{K}}$, there exists a time $\overline{t} \in [0, T)$ such that for all $0 < t < T$, the relation $0 < \overline{\delta} \leq \delta(t)$ is established, with $\overline{\delta} = \delta\left(\overline{t}\right)$. Then we can write

$$\int_{V_0}^{0} \frac{\mathrm{d}V}{\sqrt{2V}\sqrt{1-2V}} < \int_{0}^{T} -\frac{\overline{\delta}}{\beta}\ \mathrm{d}t \tag{4.24}$$

and we obtain

$$T < \frac{\beta}{\overline{\delta}}\int_{0}^{V_0} \frac{\mathrm{d}V}{\sqrt{2V}\sqrt{1-2V}} = \frac{\beta}{\overline{\delta}}\mathrm{arcsin}\sqrt{2V}\ \ < \infty \tag{4.25}$$

The finite-time reachability of sliding modes $\eta_l = 0$ has thus been proved.

For the case $\Phi\left(\vartheta\left(\mathrm{t}=0\right)\right) > \frac{\varrho}{\mathcal{K}}$ and sliding modes $\eta_r = 0$ we have

$$\eta_r\ \dot{\eta}_r = -\frac{\pi}{4\beta}\sin\left(\frac{\pi}{\beta}\varepsilon\right)\left(\Phi\left(\vartheta\right)\ \mathcal{K}\ \tanh\left(\sin\left(\varepsilon\ \pi/\beta\right)\ \right) - \varrho\ \right) = -\frac{\pi\varepsilon}{2\beta}\left|\sin\left(\frac{\pi}{2\beta}\varepsilon\right)\right|\left|\cos\left(\frac{\pi}{2\beta}\varepsilon\right)\right| \tag{4.26}$$

where $\epsilon = \Phi\left(\vartheta\right)\ \mathcal{K} + \varrho\ \tanh\left(\sin\left(\varepsilon\ \pi/\beta\right)\ \right)\ > 0$.
We can then write

$$\eta_r\ \dot{\eta}_r = -\frac{\pi\epsilon}{2\beta}\left|\eta_r\right|\sqrt{1-\eta_l^2} < -\frac{\epsilon}{\beta}\left|\eta_r\right|\sqrt{1-\eta_l^2} \tag{4.27}$$

As in the previous case, we define

$$V = \frac{1}{2}\eta_r^2 > \frac{1}{2} \tag{4.28}$$

and calculate its derivative

$$\dot{V} = \eta_r \ \dot{\eta}_r < -\frac{\epsilon}{\beta}\sqrt{2V} \ \sqrt{1-2V}. \tag{4.29}$$

If we assume that the initial condition is $V(0) = V_0$ and at the moment $t = T$ the sliding modes are reached, and that $\frac{\varrho}{\mathcal{K}}$ is small enough to satisfy $|\Phi(\vartheta(\mathrm{T}))| > \frac{\varrho}{\mathcal{K}}$, there exists a time $\bar{t} \in [0, T)$ such that for all $0 < t < T$, the relation $0 < \bar{\epsilon} \leq \epsilon(t)$ is established, with $\bar{\epsilon} = \epsilon\left(\bar{t}\right)$.

We obtain

$$\frac{\dot{V}}{\sqrt{2V}\sqrt{1-2V}} < -\frac{\bar{\epsilon}}{\beta} \tag{4.30}$$

and

$$T < \frac{\beta}{\bar{\epsilon}} \int_0^{V_0} \frac{\mathrm{d}V}{\sqrt{2V}\sqrt{1-2V}} = \frac{\beta}{\bar{\epsilon}} \mathrm{arcsin}\sqrt{2V} \ < \infty \tag{4.31}$$

The finite-time reachability of sliding modes $\eta_r = 0$ has thus been proved.

Stability of SMESC

According to [81], it is hereby presented a proof of stability for Sliding Mode ESC algorithm.
Proof: With Theorem 1, it has been proved the finite-time reachability of the sliding modes: the next step is to prove the convergence of the algorithm while in sliding modes.

The control law is synthetically expressed by eq. 4.4. If

$$\frac{\mathrm{d}}{\mathrm{d}t} \sin\left(\frac{\pi}{\beta}\varepsilon\right) = 0 \tag{4.32}$$

we can obtain

$$\nu_{eq} = \dot{\vartheta} = \frac{\varrho}{\Phi(\vartheta)} \tag{4.33}$$

in sliding modes. Moreover, since the optimum value ϑ^* is a constant (or varies extremely slowly compared to the others time-scales involved in the system), we can write

$$(\vartheta - \vartheta^*)\frac{\mathrm{d}}{\mathrm{d}t}(\vartheta - \vartheta^*) = (\vartheta - \vartheta^*)\frac{\varrho}{\Phi(\vartheta)} \tag{4.34}$$

Since ϑ^* is a maximum point, based on the way the performance function is defined, we have $(\vartheta - \vartheta^*)\Phi(\vartheta) < 0$ if $\vartheta \neq \vartheta^*$, so

$$(\vartheta - \vartheta^*)\frac{\mathrm{d}}{\mathrm{d}t}(\vartheta - \vartheta^*) < 0 \tag{4.35}$$

which means that the scheme is convergent in sliding modes.
When the system reaches the condition $|\Phi(\vartheta)| \leq \varrho/\mathcal{K}$ we have the finish of the sliding modes and

$$\dot{\varepsilon}(t) = \Phi(\vartheta)\mathcal{K}\tanh\left[\sin\left(\frac{\pi}{\beta}\varepsilon\right)\right] - \varrho < 0 \tag{4.36}$$

Since

$$\dot{\vartheta} = \mathcal{K}\tanh\left[\sin\left(\frac{\pi}{\beta}\varepsilon\right)\right] \tag{4.37}$$

once we have $|\Phi(\vartheta)| \leq \varrho/\mathcal{K}$ from the sliding surface $\varepsilon(t) = (2n+1)\beta$, we have

$$2n\beta < \varepsilon(t) < (2n+1)\beta \tag{4.38}$$

and

$$\dot{\vartheta} = \mathcal{K} > 0. \tag{4.39}$$

So we have an increment in the value of ϑ. Since then we can have two cases:

I If $\varrho/\mathcal{K}$ is small, before the system reaches $\varepsilon = 2n\beta$, it will cross the condition $|\Phi(\vartheta)| \leq \varrho/\mathcal{K}$ and reach $|\Phi(\vartheta)| > \varrho/\mathcal{K}$. In this region, the conditions of sliding modes will come into existence, and the system will reach the sliding surface $\varepsilon = 2n\beta$, on which we obtain $|\Phi(\vartheta)| \leq \varrho/\mathcal{K}$.

We then have

$$(2n-1)\beta < \varepsilon < 2n\beta \tag{4.40}$$

and

$$\dot{\vartheta} = -\mathcal{K} < 0 \tag{4.41}$$

The parameter ϑ will therefore decrease until the system gets to $|\Phi(\vartheta)| \leq \varrho/\mathcal{K}$. After the convergence to the sliding surface $\varepsilon = (2n-1)\beta$, there will be an increasing of ϑ. We can conclude that the system will oscillate around the value $\vartheta = \vartheta^*$.

II If $\varrho/\mathcal{K}$ is large, the system will remain in the region $|\Phi(\vartheta)| \leq \varrho/\mathcal{K}$ and will reach $\varepsilon = 2n\beta$, then (4.40) and (4.41) are reached and the system changes the sign of $\dot{\vartheta}$. When (4.38) and (4.39) are satisfied, the sign of the variation of ϑ changes again, and the system will oscillate around the optimum value, as showed in the previous case.

Being the system in either the first or the second of the above mentioned cases, we have proved the stability of SM-ES.

Parameter Selection for SMESC

Regarding the criteria to follow for the choice of the parameters of Sliding Mode ES, we refer Pan et al [28], and [81]. In particular the following general considerations have to be followed while tuning the Controller:

- The ratio $\beta\mathcal{K}/2\varrho$ affects the convergence rate to attain the performance-optimum value ϑ^*. A value too small slows down the convergence rate, whereas an extremely large value can be detrimental for the system stability.

- $\varrho/\mathcal{K}$ and β have to be chosen small enough to ensure that the trajectory of the system in the state-space reaches a condition when it slides along the boundaries of adjacent regions, which is called *sliding mode.*

- To satisfy the Assumption 5 of Sec. 4.1, the variation of the parameter ϑ needs to be much slower than the dynamics of the plant, the parameters $\mathcal{K}$ and ϱ need to be smaller than β. In order to guarantee both stability and convergence of the algorithm, a ratio β/ϱ of around 10^2 has proven to be suitable to achieve a good behavior of the controller, as shown in the following of the text.

4.3.2 Self driving ES

A self-driving extremum-seeking control scheme, like the sliding mode extremum-seeking control, does not require perturbations to estimate the gradient of the performance function. As no perturbations are used, the algorithm avoids the time scale associated with the perturbations, which may potentially allow for a faster convergence towards the optimum. Another peculiarity of this method is that the estimate of the gradient of the performance function is obtained through the definition of the auxiliary functions m_1, Q_1 and Q_2. This allows not only to avoid the use of perturbation signals to estimate the aforesaid gradient, but also the numerical instabilities that can be related to the use of a least-squares method to estimate the gradient itself (for example when the optimum is reached and the variation of ϑ is negligible). This leads to reduced oscillations of the optimized parameters when the optimum is reached, as shown in the following of the text.
Although self-driving systems were part of ES algorithms surveyed by Sternby [82] in 1980, they have since not gained much popularity compared to the perturbation-based ES methods. However, lately they are receiving a renewed attention in the literature; see Haring [31] and references therein. Here, we follow Haring to present a block diagram of a self-driving ES control system, as shown in Fig. 4.5.

The controller can be equivalently described by the following set of equations:

$$\text{Self-driving ES} = \begin{cases} \dot{m}_1 = \eta(J - m_1), & \eta > 0 \\ \dot{m}_2 = \eta Q_1 Q_2 (J - m_1 - Q_1 m_2) - \sigma\eta Q_2 m_2, & \sigma \geq 0 \\ \dot{Q}_1 = -\eta Q_1 + \dot{\vartheta}, & \\ \dot{Q}_2 = \eta Q_2 - \eta Q_1^2 Q_2^2 - \sigma\eta Q_2^2, & \\ \dot{\vartheta} = \lambda\eta m_2, & \lambda > 0 \end{cases} \tag{4.42}$$

Succinctly, the *observer* block estimates the gradient of the performance function, $m_2 \approx \mathrm{d}J/\mathrm{d}\vartheta$, and the *optimizer* block steers the parameter ϑ towards the performance-optimal value ϑ^*.

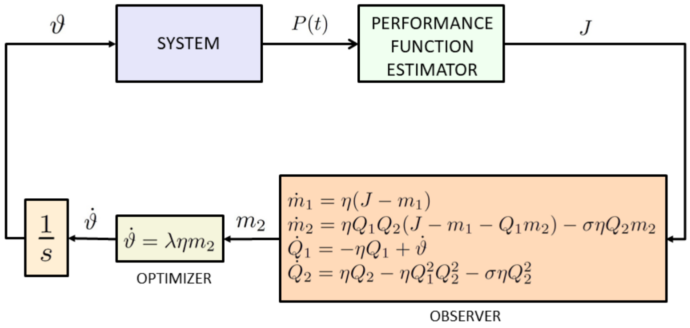

Figure 4.5: Block diagram of self-driving extremum-seeking control system [31].

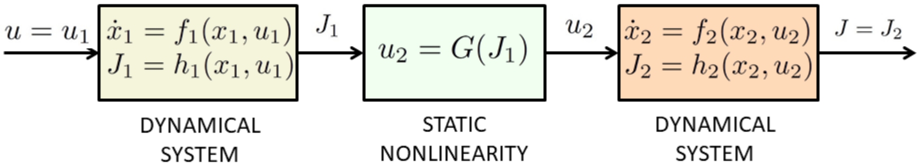

Figure 4.6: Generalized Hammersmtein-Wiener model of the Plant

Stability Analysis of Self Driving ESC

The following considerations are made in accordance with Haring [31].
First we assume that the plant can be described through a generalized Hammerstein-Wiener model, where the dynamical systems are allowed to have nonlinearities, as described in Fig. 4.6.

This way we are able to decompose the relation $J = \mathcal{F}(u)$ into three different components: two non linear dynamical systems and a static nonlinearity. If the Assumptions 1-5 in section 4.1 are met, recalling that $x(t) \in \mathbb{R}^n$ is the state of the plant and $u(t) \in \mathbb{R}$ is the plant input, we can define a map function $X : \mathbb{R} \mapsto \mathbb{R}^n, x = X(u)$.
Also, being the plant in equilibrium, we have that $u = \alpha(\vartheta, x_{\text{eq}})$, and it is ultimately possible to write $x = X(u) = X(\alpha(\vartheta, x_{\text{eq}}))$. In this section we are going to investigate the properties of the control algorithm which relates the signals u and J, but being the function $\alpha(\vartheta, x_{\text{eq}})$ smooth, and being valid the assumptions of Sec. 4.1, all the properties that are going to be analyzed, are also valid for the function $J = F(\vartheta) = F(u(\vartheta))$.

First, we define the two maps X_1 and X_2 such that $x_1 = X_1(u_1)$ and $x_2 = X_2(u_2)$. The maps $X_i(u_i)$, with $i = 1, 2$ are assumed to be smooth, like functions f and h (Assumption 3, Sec. 4.1).
We define the following functions, which describe the plant and its steady-state behavior

$$\begin{cases} M_1(t) = F(\vartheta(t)) - Q_1 \frac{\mathrm{d}F(\vartheta(t))}{\mathrm{d}t} \\ M_2(t) = \frac{\mathrm{d}F(\vartheta(t))}{\mathrm{d}t} \end{cases} \tag{4.43}$$

It is then possible to define the following coordinate transformation:

$$\begin{cases} \tilde{x}_1(t) = x_1(t) - X_1(u(t)) \\ \tilde{x}_2(t) = x_2(t) - X_2(u(t)) \\ \tilde{m}_1(t) = m_1(t) - M_1(t) \\ \tilde{m}_2(t) = m_2(t) - M_2(t) \\ \tilde{Q}_1(t) = Q_1(t) + \lambda \frac{dF(u(t))}{dt} \\ \tilde{Q}_2(t) = Q_2^{-1}(t) - \left(\lambda \frac{dF(u(t))}{dt}\right)^2 \\ \tilde{u}(t) = u(t) - u^* \end{cases} \tag{4.44}$$

The following transformations are also introduced

$$\begin{cases} \tilde{x}_1^u = \frac{\tilde{x}_1}{\tilde{u}} \\ \tilde{x}_2^u = \frac{\tilde{x}_2}{\tilde{u}^2} \\ \tilde{m}_1^u = \frac{\tilde{m}_1}{\tilde{u}^2} \\ \tilde{m}_2^u = \frac{\tilde{m}_2}{\tilde{u}} \\ \tilde{Q}_1^u = \frac{\tilde{Q}_1}{\tilde{u}} \\ \tilde{Q}_2^u = \frac{\tilde{Q}_2}{\tilde{u}^2} \end{cases} \tag{4.45}$$

We note that the last transformation is well defined if $\tilde{u} \neq 0$. We then specify the time domain in which the transformation is well defined, which is $t \in [0, t_f)$, with t_f defined as follows

$$t_f = \max\left\{\tau \in \mathbb{R}_{\geq 0} \cup \{\infty\} : \tilde{u}(t) \neq 0, \forall t \in [0, \tau)\right\}. \tag{4.46}$$

It is now important to demonstrate that the quantities introduced in (4.46) remain arbitrarily small under suitable initial conditions and parameter tuning.
We first show that the solutions of (4.45) reach input-to-state stability in an infinite t_f time, then we focus on the stability of the solutions of (4.45) and on the fact that the bounds on the solutions of $\tilde{m}_2^u$ can be made arbitrarily small given suitable tuning of the parameters and initial conditions.

Theorem 2 *If the system satisfies Assumptions 1-5 of Section 4.1 there exist constants* $c_{x11}, c_{x12}, c_{x13}, c_{x21}, c_{x22}$*,* c_{x23}*,* c_{x24}*,* c_{Q11}*,* c_{Q12}*,* c_{Q13}*,* c_{Q21}*,* c_{Q22}*,* c_{Q23}*,* c_{Q24}*,* c_{m21}*,* c_{m22}*,* c_{m23}*,* c_{m24}*,* c_{m25}*,* c_{m26}*,* c_{m27}*,* ρ_λ*,* $\rho_\eta \in \mathbb{R}_{>0}$ *such that for any* $0 \leq t_1 \leq t_f$ *the following relations hold*

$$\sup_{0\leq t<t_1} \|\tilde{x}_1^u\| \leq \max\left\{c_{x11}\|\tilde{x}_1^u(t=0)\|, \lambda\eta c_{x12}\right\}, \tag{4.47}$$

$$\sup_{0\leq t<t_1} \|\tilde{x}_2^u\| \leq \max\left\{c_{x21}\|\tilde{x}_2^u(t=0)\|, c_{x22}\sup_{0\leq t<t_1}\|\tilde{x}_1^u\|, c_{x23}\sup_{0\leq t<t_1}\|\tilde{x}_1^u\|^2, \lambda\eta c_{x24}\right\}, \tag{4.48}$$

$$\sup_{0\leq t<t_1} \left|\tilde{Q}_1^u\right| \leq \max\left\{c_{Q11}\left|\tilde{Q}_1^u(t=0)\right|, \lambda c_{Q12}\sup_{0\leq t<t_1}|\tilde{m}_2^u|, \lambda^2 c_{Q13}\right\}, \tag{4.49}$$

$$\sup_{0\leq t<t_1} \left|\tilde{Q}_2^u\right| \leq \max\left\{c_{Q21}\left|\tilde{Q}_1^u(t=0)\right|, c_{Q22}\sup_{0\leq t<t_1}\left|\tilde{Q}_1^u\right|^2, \lambda c_{Q23}\sup_{0\leq t<t_1}\left|\tilde{Q}_1^u\right|, \lambda^3 c_{Q24}\right\}, \tag{4.50}$$

$$\begin{aligned}\sup_{0\leq t<t_1} |\tilde{m}_2^u| \leq \max\Bigg\{&\frac{1}{\lambda}c_{m21}|\tilde{m}_1^u(t=0)|, c_{m22}\sup_{0\leq t<t_1}|\tilde{m}_2^u(t=0)|, \frac{1}{\lambda}c_{m23}\sup_{0\leq t<t_1}\|\tilde{x}_1^u\|,\\ &\frac{1}{\lambda}c_{m24}\sup_{0\leq t<t_1}\|\tilde{x}_1^u\|^2, \frac{1}{\lambda}c_{m25}\sup_{0\leq t<t_1}\|\tilde{x}_2^u\|, \frac{1}{\lambda}c_{m26}\sup_{0\leq t<t_1}\left|\tilde{Q}_1^u\right|, \lambda c_{m27}\Bigg\}\end{aligned} \tag{4.51}$$

for all $\lambda < \rho_\lambda$ *and all* $\eta < \rho_\eta$ *, if*

$$|\tilde{m}_2^u| < 1 \quad \textit{and} \quad \left|\tilde{Q}_2^u\right| < \lambda^2\frac{L_{F1}^2}{2} \tag{4.52}$$

for all $0 \leq t < t_1$*, where* L_{F1} *satisfies*

$$\frac{dF}{du}(u-u^*) \geq L_{F1}|u-u^*|^2. \tag{4.53}$$

For the proof of this theorem, refer to Haring [31].
The following theorem shows that the gradient estimate m_2 remains arbitrarily close to the gradient $M_2 = \frac{dF}{du}$ for appropriate tuning conditions and initial values.

Theorem 3 *If the system satisfies Assumptions 1-5 of Section 4.1 , there exist constants* ε_{x1} , ε_{x2}, ε_{m1}, ε_{m2}, ε_{Q1}, ε_{xQ2}, ε_η, $\varepsilon_\lambda, \in \mathbb{R}_{>0}$ *such that*

$$\sup_{0\leq t<t_f} |\tilde{m}_2^u| \leq C \tag{4.54}$$

for any $\|\tilde{x}_1^u(t=0)\| < \lambda\varepsilon_{x1}$*, any* $\|\tilde{x}_2^u(t=0)\| < \lambda\varepsilon_{x2}$*, any* $|\tilde{m}_1^u(t=0)| < \lambda\varepsilon_{m1}$*, any* $|\tilde{m}_2^u(t=0)| < \varepsilon_{m2}$*, any* $\left|\tilde{Q}_1^u(t=0)\right| < \lambda\varepsilon_{Q1}$*, any* $\left|\tilde{Q}_2^u(t=0)\right| < \lambda^2\varepsilon_{Q2}$*, any* $\eta < \varepsilon_\eta$ *and any* $\lambda < \varepsilon_\lambda$*.*

Also for the proof of Theorem 3, refer to Haring [31].

Theorem 3 has shown that under suitable conditions, the gradient estimate $m_2(t)$ is arbitrarily close to the gradient $M_2(t)$, which means that the gradient optimizer

$$\dot{u} = \lambda\eta m_2 \tag{4.55}$$

in (4.42) steers the input u to its optimum value u^*. For the system described in Section 4.1, we have equivalently that ϑ converges to ϑ^*.
The following theorem shows that exponential convergence of the plant input to the optimal value is obtained for a sufficiently small constant C, for $t_f \to \infty$.

Theorem 4 *If the system satisfies Assumptions 1-5 of Section 4.1 there exist constants* $\mu_u, \varepsilon_{x1}, \varepsilon_{x2}, \varepsilon_{m1}, \varepsilon_{m2}, \varepsilon_{Q1}, \varepsilon_{xQ2}, \varepsilon_\eta, \varepsilon_\lambda, \in \mathbb{R}_{>0}$ *such that*

$$\tilde{u} \leq |\tilde{u}(t=0)|\, e^{-\lambda\eta\mu_u t} \tag{4.56}$$

for all $t \geq 0$*, all* $\tilde{u}(t=0) \in \mathbb{R} - \{0\}$*, all* $\|\tilde{x}_1(t=0)\| < \lambda\varepsilon_{x1}\, |\tilde{u}(t=0)|$*,*
all $\|\tilde{x}_2(t=0)\| < \lambda\varepsilon_{x2}\, |\tilde{u}(t=0)|^2$*, all* $|\tilde{m}_1(t=0)| < \lambda\varepsilon_{m1}\, |\tilde{u}(t=0)|^2$*,*
all $|\tilde{m}_2(t=0)| < \varepsilon_{m2}\, |\tilde{u}(t=0)|$*, all* $\left|\tilde{Q}_1(t=0)\right| < \lambda\varepsilon_{Q1}\, |\tilde{u}(t=0)|$*,*
all $\left|\tilde{Q}_2(t=0)\right| < \lambda^2\varepsilon_{Q2}\, |\tilde{u}(t=0)|^2$*, all* $\eta < \varepsilon_\eta$ *and all* $\lambda < \varepsilon_\lambda$*.*

For the proof of this theorem refer to Haring [31] and Khalil [83].
From theorem 4 and (4.45), we obtain that for every $u(T=0) \neq u^*$, the plant input u converges exponentially to the optimal value u^*, or equivalently, ϑ converges to ϑ^*. Moreover, the closer $u(0)$ is to u^* and the smaller is λ, the closer the initial guesses of $x_i(0)$, $m_i(0)$, $Q_i(0)$ for $i = 1, 2$ are required to be to the real values in the plant to obtain exponential convergence.

Parameter Selection for Self Driving ESC

In this section will be discussed some general indications regarding the choice of the control parameters.
Firstly, we note that if $m_2(0)$ and $Q_1(0)$ are equal to zero, the parameter u will remain constant and not converge to the optimal value.
For increasing the convergence speed, high values of the parameters λ, η could be chosen. However, if this values are chosen to be excessively high, stability issues may occur. In order to improve the initial guess of the initial values, it is possible to keep the plant parameters constant for a sufficiently long period of time, and then activate the ESC.
In order to reduce instability of the controller due to high values of Q_2, it is possible to introduce non null values of $\sigma \in \mathbb{R}_{\geq 0}$ in (4.42), but compromising the accuracy of the estimate of u^*. For this reason, in order to obtain a balance between accuracy and stability, values of σ around 10^{-11} are chosen.
As will be shown in the next sections, this algorithm as is described in this section is not particularly suitable in the case one wants to optimize more than one parameter at the same time (MISO systems). On the other hand, one of the greatest advantages of this method is the avoidance of oscillations of parameter u, or equivalently ϑ (see section 4.1), during the optimization process for SISO systems.

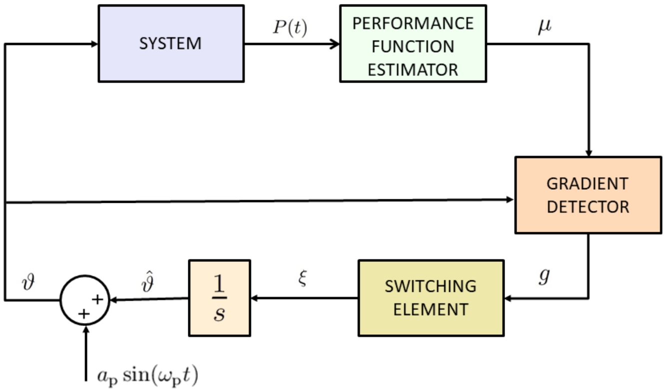

Figure 4.7: Block diagram of relay extremum-seeking control system [29].

4.3.3 Relay ES

A relay extremum-seeking control [29] provides an estimation of plant optimum, based upon the sign of the gradient. This feature is particularly useful when the controller is applied to a plant operating under widely varying conditions, which can cause the gradient value to vary in different orders of magnitude, as discussed in Sec. 4.2. In this case, using a logarithmic function in the functional composition of the performance metric is redundant, and the performance metric μ (instead of J) can be used directly for the relay ES. However, a drawback of discarding the gradient magnitude (keeping only the sign of g), is that the parameter ϑ keeps oscillating in the neighborhood of the optimal value ϑ^*, where the gradient norm is $|\mathrm{d}\mu/\mathrm{d}\vartheta|_{\vartheta^*} \approx 0$. Nevertheless, acceptable oscillations can be achieved with a proper tuning of the relay ES parameters [29].

Fig. 4.7 shows a block diagram of relay ES control system, which is described by the following set of equations:

$$\text{Relay ES} = \begin{cases} g = \frac{\delta\mu}{\delta\vartheta}, \\ \xi = \xi_0 \ \mathrm{signum}(g), \qquad \xi_0 > 0 \\ \dot{\hat{\vartheta}} = \xi, \\ \vartheta = \hat{\vartheta} + a_\mathrm{p}\sin(\omega_\mathrm{p}t), \quad a_\mathrm{p} > 0 \end{cases} \tag{4.57}$$

in which, $\delta\mu/\delta\vartheta$ is the estimation of the gradient $\mathrm{d}\mu/\mathrm{d}\vartheta$ obtained using a least-squares gradient estimation method, and the quantity $\Delta_\mathrm{p}(t) = a_\mathrm{p}\sin(\omega_\mathrm{p}t)$ is a small perturbation/dither added to the parameter ϑ in order to avoid numerical issues related to least-squares gradient estimation which, for example, may be given by an almost constant value of ϑ when the optimum is reached. The gradient g estimation is performed by generating two buffers of length n_buff, which contain the last n_buff values of performance metric μ and parameter ϑ, as

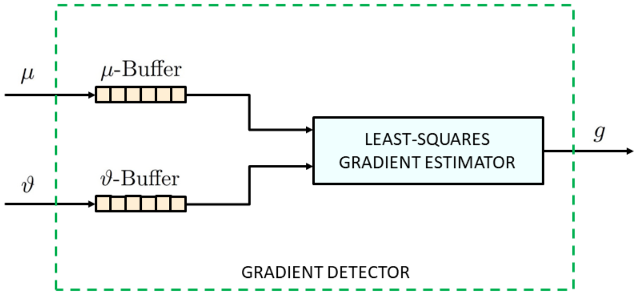

Figure 4.8: Least-squares gradient estimation for relay ES.

shown in Fig. 4.8. Given these two buffers, it is possible to estimate $\mathrm{d}\mu/\mathrm{d}\vartheta$ through applying the least-squares method, as explained in Hunnekens et al. [30].

Since the gradient estimation of the performance function is performed without a dither signal (as done in classical *perturb and observe* ES methods), the convergence speed of relay ES does not depend on the time scale of the external perturbation signal, which potentially allows for a faster convergence of relay ES systems.

Finally, the signum operator is defined as follows:

$$\text{signum}(g) = \begin{cases} 1, & \text{if} \quad g \geq 0 \\ -1 & \text{if} \quad g < 0 \end{cases} \tag{4.58}$$

From the fact that ξ is always different than zero, we have that the algorithm keeps oscillating around the optimal value of ϑ once the optimization process is complete: for this reason the choice of the parameter ξ_0 has a great relevance for the behavior of the algorithm, as discussed in the following of the text.

Stability analysis of Relay ES

The following considerations are conducted referring to [84].
Firstly, we assume that the system satisfies all the assumptions made in section 4.1. Since our purpose is to demonstrate that the equilibrium point is stable, we introduce the function $V(\vartheta(t))$, defined in a concave domain of $\mu(\vartheta)$, which means that the plant admits only one optimal value of the parameter ϑ (see Assumption 4 in section 4.1). We have:

$$V = \frac{1}{2}\left(\frac{\mathrm{d}\mu}{\mathrm{d}\vartheta}\right)^2. \tag{4.59}$$

Deriving (4.59) we obtain

$$\dot{V} = \frac{\mathrm{d}\mu}{\mathrm{d}\vartheta}\frac{\mathrm{d}^2\mu}{\mathrm{d}\vartheta^2}\frac{\mathrm{d}\vartheta}{\mathrm{d}t} \tag{4.60}$$

Since $\vartheta = \hat{\vartheta} + a_{\mathrm{p}} \sin(\omega_{\mathrm{p}} t)$, we have

$$\frac{\mathrm{d}\vartheta}{\mathrm{d}t} = \frac{\mathrm{d}\hat{\vartheta}}{\mathrm{d}t} + \frac{\mathrm{d}}{\mathrm{d}t} \left(a_{\mathrm{p}} \sin(\omega_{\mathrm{p}} t)\right) \tag{4.61}$$

Assuming that a_{p} and ω_{p} are sufficiently small, in order not to jeopardize accuracy and stability of the controller, we can write

$$\frac{\mathrm{d}\hat{\vartheta}}{\mathrm{d}t} \gg \frac{\mathrm{d}}{\mathrm{d}t} \left(a_{\mathrm{p}} \sin(\omega_{\mathrm{p}} t)\right) = a_{\mathrm{p}}\ \omega_{\mathrm{p}} \cos(\omega_{\mathrm{p}} t) \tag{4.62}$$

and thus

$$\frac{\mathrm{d}\vartheta}{\mathrm{d}t} \simeq \frac{\mathrm{d}\hat{\vartheta}}{\mathrm{d}t} \tag{4.63}$$

during the convergence process.
We can then rewrite (4.60) as follows

$$\dot{V} = \frac{\mathrm{d}\mu}{\mathrm{d}\vartheta} \frac{\mathrm{d}^2\mu}{\mathrm{d}\vartheta^2} \frac{\mathrm{d}\hat{\vartheta}}{\mathrm{d}t} = \frac{\mathrm{d}\mu}{\mathrm{d}\vartheta} \frac{\mathrm{d}^2\mu}{\mathrm{d}\vartheta^2} \left(\xi_0 \ \mathrm{signum}(g)\right) \tag{4.64}$$

according to (4.57).
The concavity of $\mu(\vartheta)$ implies

$$\frac{\mathrm{d}^2\mu}{\mathrm{d}\vartheta^2} < 0, \qquad \xi_0 \ \mathrm{signum}(g) > 0 \tag{4.65}$$

with $\xi_0 \in \mathbb{R}_{>0}$.
Considering (4.65) and (4.64), we can conclude that $\dot{V}(t) < 0$, which demonstrates the global stability of the Relay ESC algorithm.
For further insight on the algorithm, refer to Olalla et al. [29], Frantsuzova [85], Hunnekens et al. [30] and Levya et al. [84].

Parameter selection for Relay ES

In our empirical testing, we observed that by adopting excessively small buffer size, makes the controller more reactive, but decreases the stability of the algorithm, introducing a strong sensibility on noises and fast oscillations, which may jeopardize reaching and maintaining the optimal value. On the contrary, using large buffer size makes the controller more stable but less reactive, and leads to a poor estimation of the gradient. The size of the buffer also depends on the time step size adopted for acquiring data; if the step size is extremely small, the buffers need to be larger and vice-a-versa. In our tests, we maintain a buffer size sufficient enough to store the history of system performance over the last couple of wave periods. We remark that for the algorithm to converge during the initial phase of the simulation, we initialize ϑ-buffer with some non-constant values, and keep the controller inactive. The μ-buffer is filled as the simulation proceeds forward within this initial phase.

The parameters a_{p} and ω_{p} of the sinusoidal perturbation, should be set such that the time scale of the perturbation is larger than the time scale of the plant; ω_{p} must be chosen small enough for this reason. The perturbation amplitude a_{p} is also kept small to preserve the

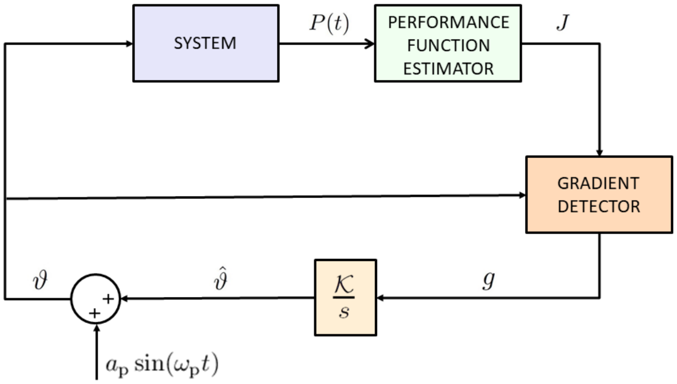

Figure 4.9: Block diagram of least-squares gradient estimation-based extremum-control system [30].

stability of the ES algorithm, as well as to reduce the oscillations around the performance-optimal value ϑ^*. In contrast, if a_p value is too small, then inaccuracies stemming from least-squares gradient estimation can cause a numerical instability.

The parameter ξ_0 is selected large enough to grant an appreciable variation of the parameter ϑ, which accelerates the convergence of the algorithm. In contrast, an extremely large value of ξ_0 causes excessive oscillations, and possibly numerical instabilities. For these reasons the value of the constant ξ_0 must be chosen to achieve a suitable behavior of the controller, being crucial for both the convergence speed and the accuracy of the algorithm.

4.3.4 Least-squares ES

The least-squares gradient estimation-based extremum-seeking control algorithm (LSQ-ES), is an extension of the relay ES, in which both the sign and magnitude of the estimate of the gradient of the performance function $\mathrm{d}J/\mathrm{d}\vartheta$ is used to derive ϑ to its performance-optimal value. A block diagram of LSQ-ES control system is shown in Fig. 4.9.

The algorithm is equivalently described by the following set of equations:

$$\text{LSQ-ES} = \begin{cases} g = \frac{\delta J}{\delta \vartheta}, & \\ \dot{\hat{\vartheta}} = \mathcal{K} g, & \mathcal{K} > 0 \\ \vartheta = \hat{\vartheta} + a_\mathrm{p} \sin(\omega_\mathrm{p} t), & a_\mathrm{p} > 0 \end{cases} \tag{4.66}$$

in which, $\delta J/\delta\vartheta$ is the least-squares gradient estimation of the performance function $\mathrm{d}J/\mathrm{d}\vartheta$, as described in Hunnekens et al. [30]. Here, we use J instead of μ as a performance metric, as was done in the Relay ES method. This difference is due to the fact that a logarithm is present in the definition of the performance function J, in order to compensate the wide variety of orders of magnitude of J itself, due to the different working conditions to which the plant is subject, following the logic presented in Ciri et al. [80].

After having obtained the value of $\hat{\vartheta}$, we obtain the plant input by adding a sinusoidal signal, which frequency is much slower than the frequency given by the plant dynamics, in order to verify assumption 5 in section 4.1.
It is important to underline that the function of the sinusoidal signal is to avoid numerical issues during the calculation of the gradient $g(t)$.
The calculation of the estimate of the gradient $\frac{\mathrm{d}F}{\mathrm{d}\vartheta}$ is conducted similarly to the Relay ESC method, by following the scheme shown in fig. 4.8.
The two buffers contain the last n_{buff} values of the quantities $J(t)$ and $\vartheta(t)$, measured each sample-time. The influence of the size of the buffers is also discussed in section 4.3.3.
Moreover, as for the Relay ES method, the absence of an external dither signal in the calculation of the gradient of the performance function, makes the convergence time independent respect to the time scale of the external signal, and thus possibly faster.

Stability analysis of LSQ-ES

In this discussion, we presume that all the assumptions made in section 4.1 are verified, and that the function $J = F(\vartheta)$ is concave.
From these assumptions, according to [30], we have that

$$\frac{\mathrm{d}J}{\mathrm{d}\vartheta}(\vartheta^*) = 0; \tag{4.67}$$

and

$$\frac{\mathrm{d}^2 J}{\mathrm{d}\vartheta^2}(\vartheta^*) < 0, \tag{4.68}$$

having for $\vartheta = \vartheta^*$ the maximum of $J(\vartheta)$. Moreover we have

$$\frac{\mathrm{d}J}{\mathrm{d}\vartheta}(\vartheta) > 0 \tag{4.69}$$

for every $\vartheta \in \mathbb{R}^+ - \{\vartheta^*\}$.
If the time-step of the system is Δt, then the buffers contain an information related to a time period $T = n_{\text{buff}}\Delta t$. This way if we are considering the system at a time t, the buffers contain information for the time interval $[t-T, t]$. It is then possible to define the following quantity:

$$\Delta\vartheta = \max_{\tau\in[-T,0]} \vartheta(t+\tau) - \min_{\tau\in[-T,0]} \vartheta(t+\tau) = \vartheta_{max} - \vartheta_{min}. \tag{4.70}$$

Theorem 5 *If we consider a system controlled as shown in fig. 4.9, that satisfies the assumptions made in section 4.1, and the conditions in (4.68), and if we choose an initial condition* $\vartheta_0 \in \Theta_0 \subset \Omega$, *with*

$$\Theta_0 = \left\{ \vartheta_0 \in \Omega | \max_{\tau\in[-T,0]} |\vartheta(\tau) - \vartheta^*| \leq \rho_\vartheta, \Delta\vartheta(0) > 0 \right\} \tag{4.71}$$

where Ω *is the Banach space defined as* $\Omega = \Omega\left([-T,0],\mathbb{R}\right)$ *containing continuous finctions mapping the interval* $[-T,0]$ *into* $\mathbb{R}$, *and* $\rho_\vartheta > 0$. *Then, the error in the gradient estimate*

$$\epsilon = \frac{\delta J}{\delta \vartheta} - \frac{\mathrm{d}J}{\mathrm{d}\vartheta} \tag{4.72}$$

can be upper-bounded as follows:

$$|\epsilon| \leq \mathcal{K}T \max_{\tau \in [-T,0]} \left| \frac{d^2 J}{d\vartheta^2}(\vartheta(t+\tau)) \right| \max_{\tau \in [-2T,0]} \left| \frac{\mathrm{d}J}{\mathrm{d}\vartheta}(\vartheta(t+\tau)) \right| \tag{4.73}$$

A proof of this theorem is provided in Hunnekens et al. [30].
Given the results of Theorem 5, it is possible to demonstrate the following theorem:

Theorem 6 *Consider a system controlled as shown in fig. 4.9, that satisfies the assumptions made in section 4.1. Then, for any initial condition $\vartheta_0 \in \Theta_0 \subset \Omega$, with Θ_0 as in (4.71) and $\rho_\vartheta > 0$, there exists a product $\mathcal{K}T$ of the gain $\mathcal{K}$ and the history time lapse T small enough such that*

$$\lim_{t \to \infty} \vartheta(t) = \vartheta^* \tag{4.74}$$

and

$$\sup_{t \geq 0} |\vartheta(t) - \vartheta^*| \leq \rho_\vartheta. \tag{4.75}$$

The result of theorem 6 proofs the asymptotic convergence of the algorithm (4.74), and its stability (4.75), under the assumptions of a static plant. In the case of non negligible plant dynamics, the convergence of the algorithm is not exact.
A proof for theorem 6 is provided in [30] for a system without a sinusoidal perturbation added to $\hat{\vartheta}$. In our case we can suppose that during the convergence

$$\dot{\vartheta} = \dot{\hat{\vartheta}} + \frac{\mathrm{d}}{\mathrm{d}t}\left(a_\mathrm{p} \sin(\omega_\mathrm{p} t)\right) = \dot{\hat{\vartheta}} + a_\mathrm{p}\, \omega_\mathrm{p} \cos(\omega_\mathrm{p} t) \simeq \dot{\hat{\vartheta}} \tag{4.76}$$

being the parameters a_p and ω_p chosen to be small enough.

Parameter selection for LSQ ESC

Following theorems 5 and 6 we can observe that an important parameter for the behavior of the algorithm is $\mathcal{K}T$, which should be chosen small enough in order to guarantee convergence and stability of the algorithm.
The magnitude of the parameter T depends on the time-step Δt of the algorithm and on the size n_buff of the buffers. It is important to consider that adopting excessively small buffers would make the controller more reactive, but decreases the stability of the algorithm, introducing a strong sensibility on noises and fast oscillations, which may jeopardize reaching and maintaining the optimal value. On the contrary, using large buffer size makes the controller more stable but less reactive, and leads to a poor estimation of the gradient. Parameter $\mathcal{K}$ should then be chosen accordingly to the magnitude of T, in order to achieve the stability of the algorithm.
Regarding the parameters a_p and ω_p of the sinusoidal perturbation, we underline that the

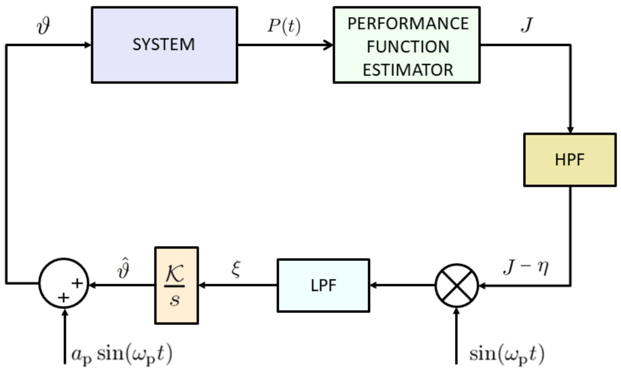

Figure 4.10: Block diagram of perturbation-based extremum-seeking control system [37]. First-order low-pass and high-pass filters of the form $\frac{\omega_L}{s+\omega_L}$ and $\frac{s}{s+\omega_H}$, respectively, are used.

time scale of the sinusoidal signal must be much larger than the time scale given by the dynamics of the plant, so ω_p must be chosen small enough. Also a_p has to be chosen small enough in order to maintain a stable algorithm and reduce oscillations around the optimal value ϑ^*. Choosing small values for the parameters a_p and ω_p also results in the validity of condition (4.76), which leads to a good behavior of the system in terms of convergence and stability, as shown in theorem 6. On the other hand, a_p cannot be chosen too small to maintain the stability of the least-squares algorithm.

4.3.5 Perturbation-based ES

Perturbation-based extremum-seeking control is historically the first ES control algorithm. In 1922, Leblanc first applied a perturbation-based ES to maximize the power transfer from an overhead electrical transmission line to a tram car [26]. The method underwent several extensions and modifications till 1960s, after which it had lost popularity in lieu of other control schemes at that time. This was mainly because of the difficulty to generalize the algorithm for a large class of plants. In 2000, Krstić and Wang [11] proved the stability of perturbation-based extremum-seeking control scheme for a generic plant satisfying certain properties, as listed in Sec. 4.1. This publication has reignited the interest of the research community in ES methods, and since then, many variants and applications based on extremum-seeking control algorithms have been considered, some of which were discussed in the previous sections.

Fig. 4.10 shows a block diagram of perturbation-based ES control system. The scheme can be equivalently described by the following set of equations:

$$\text{Perturbation-based ES} = \begin{cases} \dot{\eta} = \omega_{\mathrm{H}}(J - \eta), & \omega_{\mathrm{H}} > 0 \\ \dot{\xi} = \omega_{\mathrm{L}}\left((J - \eta)\sin(\omega_{\mathrm{p}} t) - \xi\right), & \omega_{\mathrm{L}} > 0 \\ \dot{\hat{\vartheta}} = \mathcal{K}\xi, & \mathcal{K} > 0 \\ \vartheta = \hat{\vartheta} + a_{\mathrm{p}} \sin(\omega_{\mathrm{p}} t). & a_{\mathrm{p}} > 0 \end{cases} \tag{4.77}$$

An intuitive working principle of perturbation-based ES can be explained as follows. A perturbation signal $\Delta_{\mathrm{p}}(t) = a_{\mathrm{p}} \sin(\omega_{\mathrm{p}} t)$ is added to the current estimate of the parameter ϑ and passed into the plant. The plant's performance J is measured/calculated for the updated parameter. If the output signal J can be linearized around the current estimate of ϑ, then the change in J due to the perturbation signal can be obtained using a Taylor-series expansion

$$J - \eta \approx \frac{\mathrm{d}J}{\mathrm{d}\vartheta}\Delta_{\mathrm{p}}, \tag{4.78}$$

in which, η is the DC component of the signal that can be subtracted from J by passing it through a high-pass filter (HPF) of cut-off frequency ω_{H}. The change in the performance function due to the added perturbation is then multiplied by another perturbation signal to yield the following quantity:

$$(J - \eta)\Delta_{\mathrm{p}} \approx \frac{\mathrm{d}J}{\mathrm{d}\vartheta}\Delta_{\mathrm{p}}^2. \tag{4.79}$$

The resultant of this operation contains an information of the derivative of the performance function respect to the parameter ϑ, and an oscillating signal of frequency 2ω. The whole signal is therefore passed through a low-pass filter (LPF) of cut-off frequency ω_{L} which allows the elimination of the oscillating component Δ_{p}^2, leaving only the information about the gradient of the performance function, indicated by $\xi \approx \mathrm{d}J/\mathrm{d}\vartheta$ with the correct sign [1]. Following the gradient estimation, an integrator with gain $\mathcal{K}$ updates the ϑ parameter, and the optimization process is repeated until convergence is obtained.

The plant input is obtained adding a sinusoidal signal $a_{\mathrm{p}} \sin(\omega_{\mathrm{p}} t)$ to the estimate $\hat{\vartheta}$ of the optimal parameter. The oscillation of ϑ produces an oscillation of the performance function J, thus allowing a demodulation of J itself. The influence of the amplitude a_{p} of the sinusoidal signal will be discussed in section 4.3.5.

Stability Analysis of Perturbation Based ESC

The following discussion is made accordingly to Powell [86] and Krstić and Wang [11].

Under the assumptions made in section 4.1, using a sinusoidal perturbation, we can define the following state-space summary, being $x \in \mathbb{R}^n$ the state of the plant:

---

[1] As Δ_{p}^2 is a positive quantity, the sign of the signal is decided by the gradient of the performance function $\mathrm{d}J/\mathrm{d}\vartheta$.

$$\begin{bmatrix}\dot{x}\\ \dot{\hat{\vartheta}}\\ \dot{\xi}\\ \dot{\eta}\end{bmatrix} = \begin{bmatrix} f\left(x, \alpha(x, \hat{\vartheta} + a_{\mathrm{p}} \sin(\omega_{\mathrm{p}} t)\right) \\ \mathcal{K}\xi \\ \omega_L\left((J-\eta)\sin(\omega_{\mathrm{p}} t) - \xi\right) \\ \omega_H(J-\eta) \end{bmatrix} \tag{4.80}$$

We define the error in the estimation of the optimal value as $\tilde{\vartheta} = \hat{\vartheta} - \vartheta^*$, while the error on the DC component of the performance function respect to the optimal performance is defined as $\tilde{\eta} = \eta - J(\vartheta^*)$.

We furthermore proceed in giving the following definitions:

$$\omega_H = \omega_{\mathrm{p}}\omega_h = \omega_{\mathrm{p}}\delta\omega_h' \tag{4.81}$$

$$\omega_L = \omega_{\mathrm{p}}\omega_l = \omega_{\mathrm{p}}\delta\omega_l' \tag{4.82}$$

$$\mathcal{K} = \omega K = \omega_{\mathrm{p}}\delta K' \tag{4.83}$$

where $\omega_{\mathrm{p}}, \delta, \omega_h', \omega_l', K' \in \mathbb{R}_{>0}$.

It is then possible to define a new time scale for the system, $\tau = \omega_{\mathrm{p}} t$. The space-state of the system can be rewritten as

$$\omega_{\mathrm{p}}\frac{\mathrm{d}x}{\mathrm{d}\tau} = f\left(x, \alpha(x, \tilde{\vartheta} + \vartheta^* + a_{\mathrm{p}}\sin\tau)\right) \tag{4.84}$$

and

$$\frac{\mathrm{d}}{\mathrm{d}\tau}\begin{bmatrix}\tilde{\vartheta}\\ \xi\\ \tilde{\eta}\end{bmatrix} = \begin{bmatrix} K'\xi \\ \omega_l'[(J(x(\vartheta)) - J(\vartheta^*) - \tilde{\eta})a_{\mathrm{p}}\sin\tau - \xi] \\ \omega_h'[(J(x(\vartheta)) - J(\vartheta^*) - \tilde{\eta}] \end{bmatrix}. \tag{4.85}$$

From here we can apply an averaging analysis of the model. Being the variation of ϑ extremely slower than the time scale given by the plant dynamics, we can write $x = l(\vartheta) = l(\vartheta^* + \tilde{\vartheta} + a_{\mathrm{p}}\sin\tau)$.
Substituting into equation (4.85), we obtain the space-state of the reduced system, described by $\tilde{\vartheta}_r$, ξ_r and $\tilde{\eta}_r$:

$$\frac{\mathrm{d}}{\mathrm{d}\tau}\begin{bmatrix}\tilde{\vartheta}_r\\ \xi_r\\ \tilde{\eta}_r\end{bmatrix} = \begin{bmatrix} K'\xi_r \\ \omega_l'[(v - \tilde{\eta}_r)a\sin\tau - \xi_r] \\ \omega_h'(v - \tilde{\eta}_r) \end{bmatrix}, \tag{4.86}$$

where $v = v(\tilde{\vartheta}_r + a_{\mathrm{p}}\sin\tau)$. Recalling that $J = h(x)$, as defined is section 4.1, we can write

$$v = h(l(\vartheta^* + \tilde{\vartheta}_r + a_{\mathrm{p}}\sin\tau)) - h(l(\vartheta^*)). \tag{4.87}$$

The average model, described by $\tilde{\vartheta}^a_r$, ξ^a_r and $\tilde{\eta}^a_r$ can be written as

$$\frac{d}{d\tau}\begin{bmatrix}\tilde{\vartheta}^a_r\\ \xi^a_r\\ \tilde{\eta}^a_r\end{bmatrix} = \begin{bmatrix} K'\xi^a_r \\ \omega'_l[-\xi^a_r + \frac{a}{2\pi}\int_0^{2\pi}(v_a \sin\sigma \mathrm{d}\sigma)] \\ \omega'_h(-\tilde{\eta}^a_r + \frac{1}{2\pi}\int_0^{2\pi}(v_a \mathrm{d}\sigma)]) \end{bmatrix}, \tag{4.88}$$

with $v_a = v(\tilde{\vartheta}^a_r + a_\mathrm{p}\sin\sigma)$.
The average equilibrium of the system is then described by the following condition:

$$\begin{bmatrix}0\\0\\0\end{bmatrix} = \begin{bmatrix} \xi^{a,e}_r \\ \int_0^{2\pi}\Big(v(\tilde{\vartheta}^{a,e}_r + a_\mathrm{p}\sin\sigma)\sin\sigma \mathrm{d}\sigma\Big)] \\ \frac{1}{2\pi}\int_0^{2\pi}\Big(v(\tilde{\vartheta}^{a,e}_r + a_\mathrm{p}\sin\sigma)\mathrm{d}\sigma\Big) - \tilde{\eta}^{a,e}_r \end{bmatrix} \tag{4.89}$$

where the superscript $(^e)$ denotes the equilibrium value of the state variable.
We now assume that $\tilde{\vartheta}^{a,e}_r$ can be approximated with $\tilde{\vartheta}^{a,e}_r = b_1 a_\mathrm{p} + b_2 a_\mathrm{p}^2 + H$, with H indicating a collection of higher order powers of a_p.
Applying the techniques described in Krstić and Wang [11], it is possible to obtain the following solution:

$$\begin{bmatrix}\tilde{\vartheta}^{a,e}_r\\ \xi^{a,e}_r\\ \tilde{\eta}^{a,e}_r\end{bmatrix} = \begin{bmatrix} -\frac{v'''(0)}{8v''(0)}a_\mathrm{p}^2 + H \\ 0 \\ \frac{v''(0)}{4}a_\mathrm{p}^2 + H \end{bmatrix}. \tag{4.90}$$

If we calculate the Jacobian $\mathcal{J}^a_r$ of the averaged system from equation (4.88), we can conclude that the system is stable only if

$$\int_0^{2\pi}\Big(v'(\tilde{\vartheta}^{a,e}_r + a_\mathrm{p}\sin\sigma)\sin\sigma\ \mathrm{d}\sigma\Big) < 0. \tag{4.91}$$

From equation (4.91), calculating the determinant of the Jacobian $\mathcal{J}^a_r$, we obtain that the system is exponentially stable for values of a_p suitably small, and therefore the system has a stable periodic solution.
For the in-depth procedure, refer to Krstić and Wang [11].

Parameter selection for Perturbation-based ES

Regarding the adequate choice for the parameters of the controller, we start from the parameters characterizing the sinusoidal perturbation, on which the entire algorithm relies for its functioning.
The amplitude a_p of the signal must be chosen small enough to guarantee convergence, as discussed in section 4.3.5. Moreover a small value of a_p results in limited oscillation of the parameter ϑ during the convergence. On the other hand, greater values of a_p result in a greater value of the amplitude of the oscillation of the performance function J and following of the demodulated signal, and thus of ξ, resulting in a faster convergence of the algorithm.
The angular frequency ω_p of the signal must be slower than the characteristic frequencies given by the plant dynamics, in order to guarantee the validity of assumption 5 in section

4.1.
The cutoff frequency ω_H of the High-Pass Filter should be chosen such as the frequency content given by the sinusoidal perturbation is allowed to pass through, while the DC component of the signal J must be blocked in order to extract only the oscillations of J provoked by the dither signal.
The cutoff frequency ω_L of the Low-Pass Filter should be chosen instead small enough to let through only the lower frequencies, thus blocking the oscillations given by the frequency ω_{p}, in order to obtain a smooth temporal evolution of the parameter $\hat{\vartheta}$.
Finally, the integration gain $\mathcal{K}$ needs to be small enough to guarantee the stability of the algorithm, although too small values can result in a extremely slow convergence.

5. Device and wave characteristics

In this section are described the sea states analyzed for the present study, and the hulls used for the simulations: in particular there have been chosen three regular waves and three irregular waves. For each regular sea state, characterized by a value of $\mathcal{T}$ and $\mathcal{H}$, there is a corresponding irregular wave characterized by the same values of $\mathcal{T}_\mathrm{p}$ and $\mathcal{H}_\mathrm{s}$ and vice versa. For each sea state we present the optimal values of the PTO parameters obtained through a reference-to-output map (brute force search of the optimum) confronted with the results provided by the impedance matching control theory (only for regular sea states).

Also, some information about the hulls used are provided: it is important to underline that in the present study we have been using a scaled version of the problem: in order to bring the values to a full scale, it is possible to use the Froude scaling theory (see Shmitt et Elsäßer [87]). It is important to note that two hulls have been used: one cylindrical and one spherical.

Finally, also some information about the optimal PTO values for the MSD simulations are provided.

5.1 Wave characteristics

As anticipated, in the present study we used three regular and three irregular waves, which are described in Tab. 5.1.

These wave characteristics are chosen based on the scale of the device; see Dafnakis et al. [44] and Khedkar et al. [69] for discussion.

For each of the hulls used we now provide the optimal values of the PTO for all the sea states studied.

Table 5.1: Sea states.

Regular sea ID	$\mathcal{T}$ (s)	$\mathcal{H}$ (m)	Irregular sea ID	$\mathcal{T}_\mathrm{p}$ (s)	$\mathcal{H}_\mathrm{s}$ (m)
Reg.1	0.625	0.01	Irreg.1	0.625	0.01
Reg.2	0.8	0.02	Irreg.2	0.8	0.02
Reg.3	1.0	0.0075	Irreg.3	1.0	0.0075

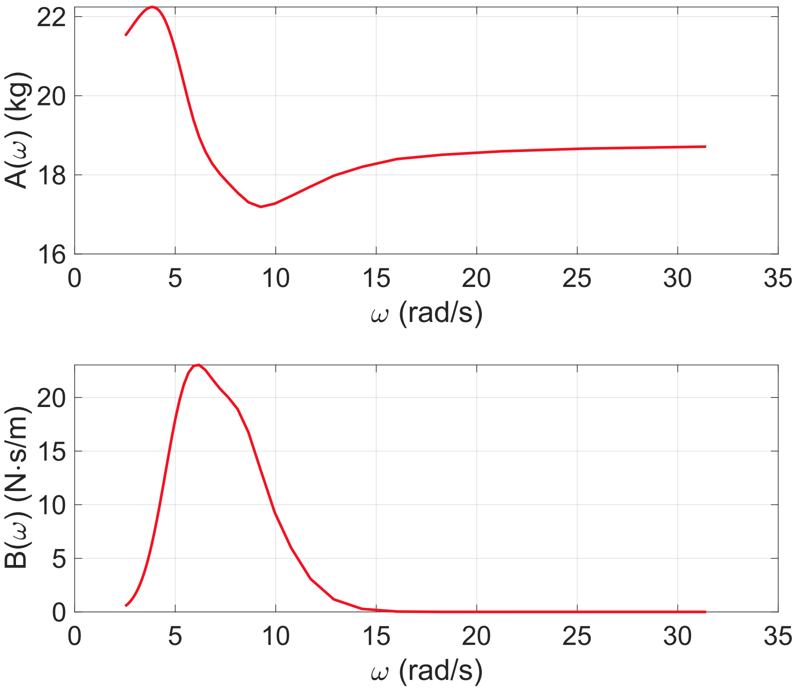

Figure 5.1: Frequency-dependent added-mass $A(\omega)$, and radiation damping $B(\omega)$ for the two-dimensional cylindrical buoy. The coefficients are obtained using BEM-based ANSYS AQWA software.

5.1.1 Optimal PTO parameters values: cylindrical hull

An overview of the optimal PTO values is provided: the brute force search results are provided through reference-to-output maps and, for the regular sea states these results are compared to the ones obtained using 3.27 and 3.28.

Regular sea states

Fig. 5.2 shows the result fo the regular sea states.

Tab. 5.2 contains the comparison between the brute force results and the impedance matching control theory. The optimal coefficients for the impedance matching control theory are obtained according to Fig. 5.1.

Since the theoretical formula ignores the viscous drag force, the tabulated values confirm that the theoretical estimates of the optimal reactive coefficients are quite accurate, whereas the optimal resistive coefficients are under-predicted, missing a drag contribution in 3.28. Moreover, it is evident the dependence of K_{opt} respect to the period (frequency) of the regular wave: if the period $\mathcal{T}$ increases (or correspondingly ω decreases), the optimal stiffness value decreases according to a quadratic relation.

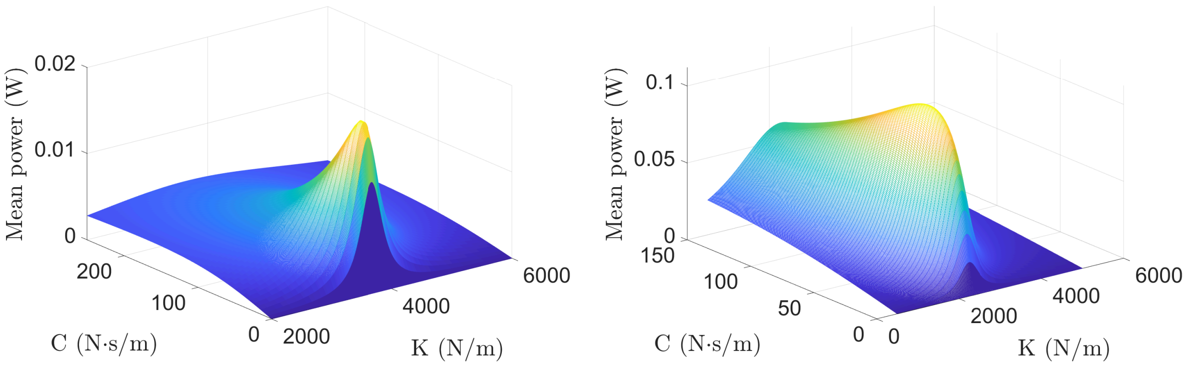

(a) Sea state Reg.1

(b) Sea state Reg.2

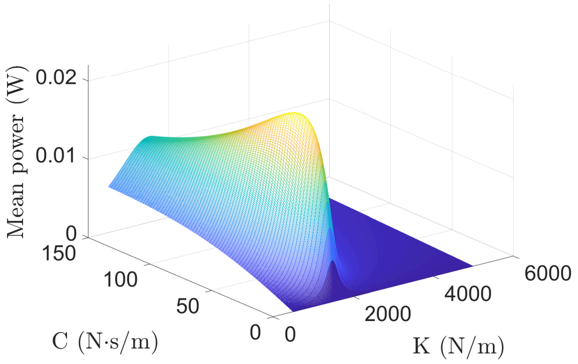

(c) Sea state Reg.3

Figure 5.2: Power vs. PTO coefficients reference-to-output map for a two-dimensional cylinder subject to regular waves. The optimal PTO coefficients are: (a) $K_{\text{opt}} = 3720$ N/m and $C_{\text{opt}} = 18$ N·s/m; (b) $K_{\text{opt}} = 2290$ N/m and $C_{\text{opt}} = 34$ N·s/m; and (c) $K_{\text{opt}} = 1530$ N/m and $C_{\text{opt}} = 30$ N·s/m.

Table 5.2: Optimal PTO coefficients for a two-dimensional cylindrical buoy subject to regular waves using impedance-matching control theory and through a brute-force search. Units: $\mathcal{T}$ is in s, $\mathcal{H}$ is in m, K is in N/m, and C is in N·s/m.

Sea state ID	$\mathcal{T}$	$\mathcal{H}$	$K_{\text{opt,map}}$	$C_{\text{opt,map}}$	$K_{\text{opt,analytical}}$	$C_{\text{opt,analytical}}$
Reg.1	0.625	0.01	3720	18	3717	9
Reg.2	0.8	0.02	2290	34	2302	20
Reg.3	1	0.0075	1530	30	1534	21

Table 5.3: Optimal PTO coefficients for a two-dimensional cylindrical buoy subject to irregular waves using impedance-matching control theory and through a brute-force search. Units: $\mathcal{T}_\text{p}$ is in s, $\mathcal{H}_\text{s}$ is in m, K is in N/m, and C is in N·s/m.

Sea state ID	$\mathcal{T}_\text{p}$	$\mathcal{H}_\text{s}$	$K_\text{opt,map}$	$C_\text{opt,map}$
Irreg.1	0.625	0.01	3440	32
Irreg.2	0.8	0.02	2170	44
Irreg.3	1	0.0075	1480	40

Irregular sea states

A WEC device subject to irregular waves has multiple frequencies in its dynamics. Consequently, a closed-form solution for energy-maximizing PTO coefficients is difficult to obtain analytically. To verify the controller results, we perform a brute-force search of the parametric space to find the optimal values of the PTO coefficients for three irregular sea states. Fig. 5.3 plots power vs. coefficients reference-to-output map, and Table 5.3 lists their optimal values.

Also for the irregular waves it is possible to observe the same behavior of K_opt and C_opt respect to the peak period and significant height of the waves.

Finally, we have that the optimal values of the PTO stiffness are lower than the corresponding regular waves, while the optimal damping is generally higher. This behavior may be due to the higher influence of the components with high periods (low frequencies) in the spectrum. Waves with low frequencies tend to have a lower PTO optimal stiffness and, if in the descending part of the $B(\omega)$ curve in Fig. 5.1, a higher optimal PTO damping.

5.1.2 Optimal PTO parameters values: spherical hull

In this section we provide an overview of the optimal values for the PTO parameters, for both regular and irregular waves. The optimal values obtained for the regular wave cases are compared with the values obtained through the impedance matching control theory for the regular sea states.

Regular sea states

Fig. 5.5 shows the result fo the regular sea states.

Tab. 5.4 contains the comparison between the brute force results and the impedance matching control theory. The optimal coefficients for the impedance matching control theory are obtained according to Fig. 5.4.

Also for the spherical hull, since the theoretical formula in 3.28 ignores the viscous drag force, the tabulated values confirm that the theoretical estimates of the optimal reactive coefficients are quite accurate, whereas the optimal resistive coefficients are under-predicted, missing a drag contribution.

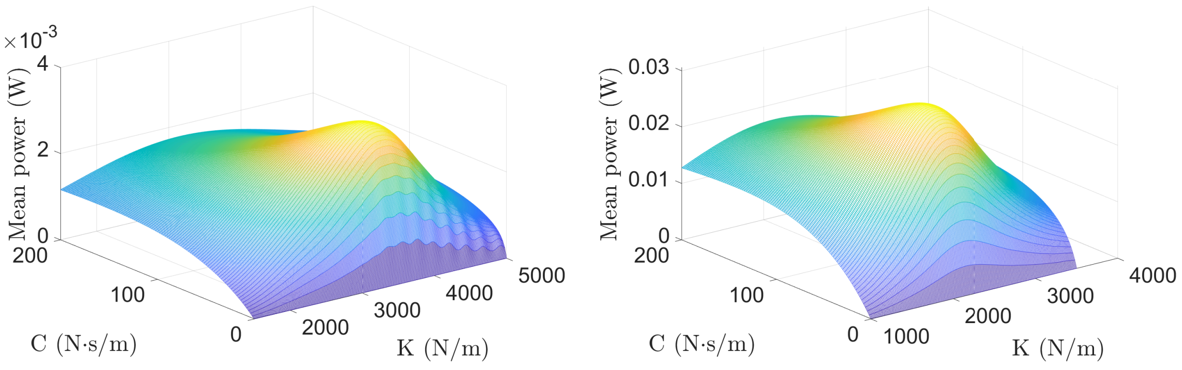

(a) Sea state Irreg.1 (b) Sea state Irreg.2

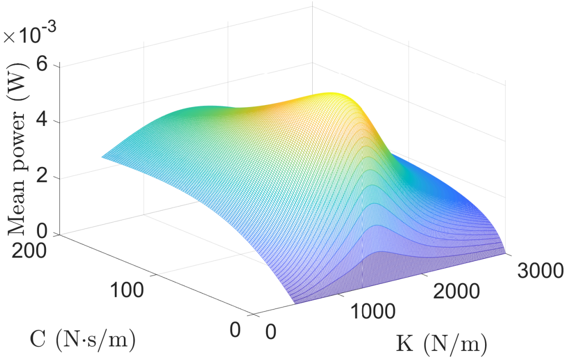

(c) Sea state Irreg.3

Figure 5.3: Power vs. PTO coefficients reference-to-output map for a two-dimensional cylinder operating in an irregular sea. The optimal PTO coefficients are: (a) $K_{\text{opt}} = 3440$ N/m and $C_{\text{opt}} = 32$ N·s/m; (b) $K_{\text{opt}} = 2170$ N/m and $C_{\text{opt}} = 44$ N·s/m; and (c) $K_{\text{opt}} = 1480$ N/m and $C_{\text{opt}} = 40$ N·s/m.

Table 5.4: Optimal PTO coefficients for a three-dimensional spherical buoy subject to regular waves using impedance-matching control theory and through a brute-force search. Units: $\mathcal{T}$ is in s, $\mathcal{H}$ is in m, K is in N/m, and C is in N·s/m.

Sea state ID	$\mathcal{T}$	$\mathcal{H}$	$K_{\text{opt,map}}$	$C_{\text{opt,map}}$	$K_{\text{opt,analytical}}$	$C_{\text{opt,analytical}}$
Reg.1	0.625	0.01	310	6	312	3
Reg.2	0.8	0.02	200	6	203	2
Reg.3	1	0.0075	130	4	132	1

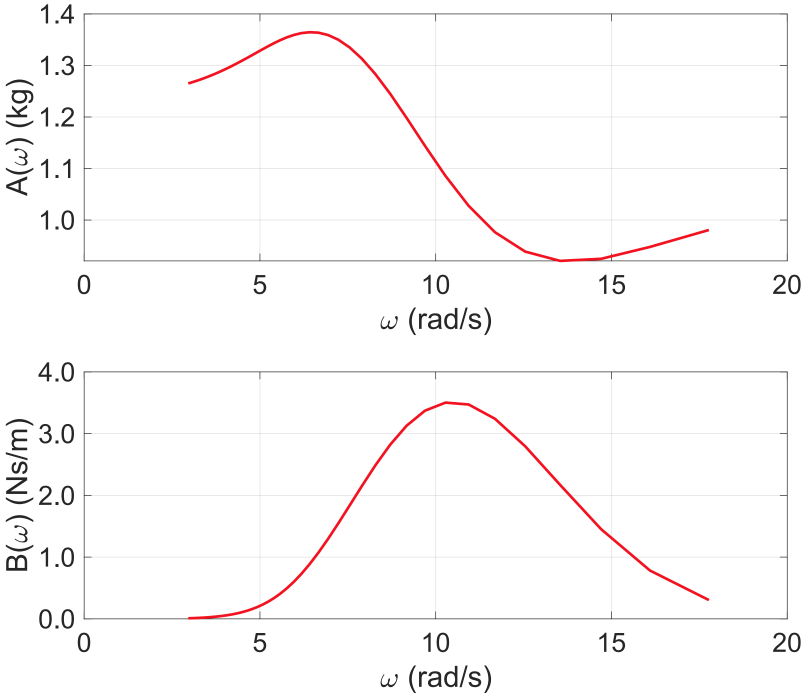

Figure 5.4: Frequency-dependent added-mass $A(\omega)$, and radiation damping $B(\omega)$ for the three-dimensional spherical buoy. The coefficients are obtained using BEM-based ANSYS AQWA software.

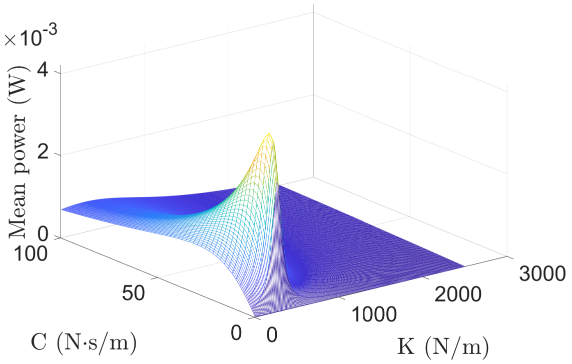

(a) Sea state Reg.1

(b) Sea state Reg.2

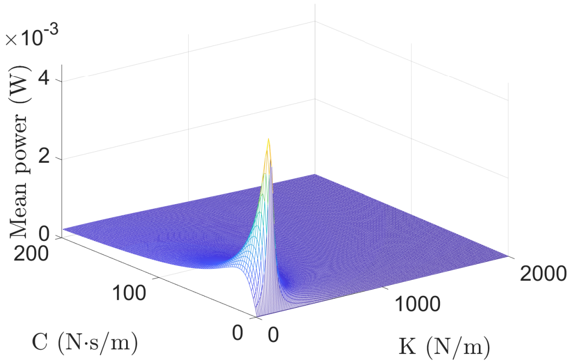

(c) Sea state Reg.3

Figure 5.5: Power vs. PTO coefficients reference-to-output map for a three-dimensional sphere subject to regular waves. The optimal PTO coefficients are: (a) $K_{\text{opt}} = 310$ N/m and $C_{\text{opt}} = 6$ N·s/m; (b) $K_{\text{opt}} = 200$ N/m and $C_{\text{opt}} = 6$ N·s/m; and (c) $K_{\text{opt}} = 130$ N/m and $C_{\text{opt}} = 4$ N·s/m.

Table 5.5: Optimal PTO coefficients for a three-dimensional spherical buoy subject to irregular waves using impedance-matching control theory and through a brute-force search. Units: $\mathcal{T}_\mathrm{p}$ is in s, $\mathcal{H}_\mathrm{s}$ is in m, K is in N/m, and C is in N·s/m.

Sea state ID	$\mathcal{T}_\mathrm{p}$	$\mathcal{H}_\mathrm{s}$	$K_\mathrm{opt,map}$	$C_\mathrm{opt,map}$
Irreg.1	0.625	0.01	290	4
Irreg.2	0.8	0.02	180	4
Irreg.3	1	0.0075	125	4

Irregular sea states

As for the cylindrical hull, a closed-form solution for energy-maximizing PTO coefficients is difficult to obtain analytically. Thus, to verify the controller results, we perform a brute-force search of the parametric space to find the optimal values of the PTO coefficients for three irregular sea states. Fig. 5.6 plots power vs. coefficients reference-to-output map, and Table 5.5 lists their optimal values.

Also for the irregular waves it is possible to observe the same behavior of K_opt and C_opt respect to the peak period and significant height of the waves.
Moreover, we have that the optimal values of the PTO stiffness are lower than the corresponding regular waves. This behavior may be due to the higher influence of the components with high periods (low frequencies) in the spectrum, since waves with low frequencies tend to have a lower PTO optimal stiffness.

5.2 Hull characteristics

Motivated by the prior work on numerical modeling of a fully-submerged axisymmetric point absorber device [44], we simulate a two-dimensional cylindrical, and a three-dimensional spherical buoy to perform extremum-seeking control simulations.
Following the same convention for the symbols used Fig. 3.2, we have:

Table 5.6: Hull dimensions and parameters: the symbols are used according to Fig. 3.2. ρ_s is the hull density, assuming that the hull is homogeneous.

Dimension	Cylindrical Hull	Spherical Hull
D (m)	0.16	0.16
ρ_s (kg/m^3)	922.5	922.5
d_s (m)	0.25	0.25
d (m)	0.65	0.65

Also, it is important to note that in order to conduct a 2D analysis on the cylindrical hull, it has been chosen an axial length of $L = 8D$ =1.28 m to minimize the influence of the ends, while keeping the simulations computationally affordable.
Moreover, the density ρ_s of the hulls, supposed to be homogeneous, is chosen to be 90%

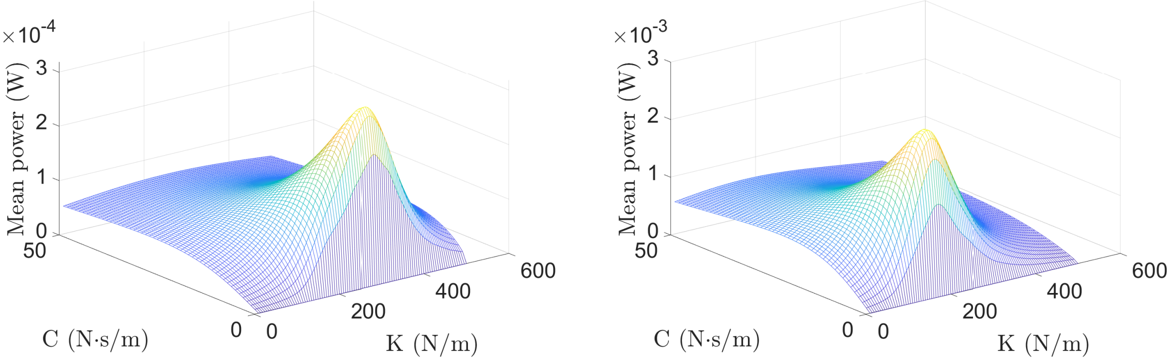

(a) Sea state Irreg.1 (b) Sea state Irreg.2

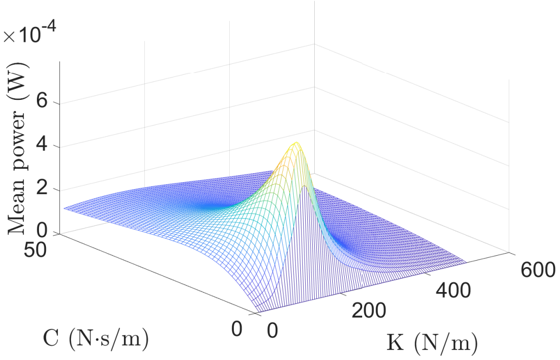

(c) Sea state Irreg.3

Figure 5.6: Power vs. PTO coefficients reference-to-output map for a two-dimensional cylinder operating in an irregular sea. The optimal PTO coefficients are: (a) $K_{\text{opt}} = 290$ N/m and $C_{\text{opt}} = 4$ N·s/m; (b) $K_{\text{opt}} = 180$ N/m and $C_{\text{opt}} = 4$ N·s/m; and (c) $K_{\text{opt}} = 125$ N/m and $C_{\text{opt}} = 4$ N·s/m.

of the sea water density, in order to reduce the static tension of the mooring due to the buoyancy forces according to the Archimedes' principle.

5.3 Optimal PTO parameters values for the *dry oscillator*

As stated in Sec. 3, the MSD system has been used to verify the convergence of the algorithms used, since an analytical solution for the optimal values PTO is easily calculable.
The mass-spring-damper system of Sec. 3.1 is considered here using the parameters tabulated in Table 5.7.
The table also lists the optimal values of K_{opt} and C_{opt} coefficients, obtained analytically according to 3.11 and 3.16.

Table 5.7: Mass-spring-damper parameters.

Parameter	Value
m	18.55 kg
k	200 N/m
c	15 N·s/m
$\mathcal{T}$	0.5 s
f_0	10 N
K_{opt}	2729 N/m
C_{opt}	15 N·s/m

where m is the mass of the of the object, k is the inherent stiffness of the spring, c is the inherent damping of the linear damper, $\mathcal{T}$ is the period of the sinusoidal force $F(t) = f_0 \sin(\omega t)$, while f_0 is the amplitude of the sinusoidal force.

In the case of the mass-spring-damper system the inherent values have been chosen to generate a system which characteristics are similar to the ones of the oscillating buoys. Also the period of the exciting force is chosen to be compatible to the ones used for the point absorber.
After having defined the problem and its characteristics, in the following section are provided the simulation results for both the *dry oscillator* and the PA.

6. Results

In this section are shown the results obtained through the simulation of the systems described in sections 3.1 (*dry oscillator*) and sections 3.2 and 5.2 (point absorber), for the conditions described in sections 3.3, 5.1.2 (point absorber) and 5.3 (*dry oscillator*).
The first results shown regard the demonstration that the algorithms converge to the analytical optimal solution in the MSD case. After that we move to the cylindrical hull, for both regular and irregular sea states. Finally, the results for the sperical point absorber, for both regular and irregular waves, are reported.
It is important to observe that for each of the cases described (i.e. cylindrical hull, sea state Reg. 1), a study have been conducted regarding the optimization of a single PTO parameter (K, C) at one time, and for both parameters simultaneously (K and C). The results for each of these cases will be reported in this chapter.
Finally, note that every case that has been analyzed comprehends different simulations starting with a wide range of initial values: the reason of this choice is to prove that the algorithms converge to the same (optimal) value regardless of the starting value, thus showing that the control laws that lead to the optimal are robust. The starting values are chosen to be the same for each case, in order to compare the results for different algorithms. In some cases initial oscillations are noticeable at the beginning of the simulations: these are due to the fact that during the initial transient (when the controller is not active) an oscillation is imposed to the parameters. This oscillation is useful for example when the gradient is calculated through the least-squares method, in order to fill the ϑ-buffer with non-constant values, thus avoiding numerical problems in the initial estimate of the gradient of the performance function.
It is important to underline that the optimal values for all the point absorber cases analyzed in this study are derived from the reference-to-output maps reported for each sea state. Moreover, the model used for the study includes the effect of the drag forces on the hull.

6.1 *Dry oscillator*

In this section, the results relative to the optimization of the *dry oscillator* (MSD) system are shown.
We begin with single-parameter optimization of either reactive coefficient K or resistive coefficient C, by keeping the other fixed at its optimal value. The optimization results for K with different initial values are shown in Fig. 6.1, whereas Fig. 6.2 shows the optimization results for C. As can be seen in both figures, all ES algorithms convergence to the theory-

predicted optimal value.

Next, we perform simultaneous optimization of both PTO coefficients.
The results are shown in Fig. 6.3 for four ES algorithms; the self-driving ES method did not converge reliably for the two-parameter optimization problem (divergent data not presented). On the other hand, all the other algorithms converge reliably to the optimal values.

It is also possible to observe the increment on the extracted power during the optimization of the parameters, for the Perturbation based algorithm, which presents the least oscillations during the steady state, and for the Sliding Mode ESC, which has the greatest oscillations (see fig.6.4).

In this case we can observe that there is no substantial difference between the two algorithms for the oscillation of the extracted power during the steady-state.
Finally, we have verified that the algorithms used for the optimization of the PTO parameters are steering the values of K and C to their optimal values.

6.2 Cylindrical point-absorber

In the present section are reported the results for the optimization of the PTO parameters K and C first one at a time and then simultaneously.
The simulations have been conducted for both regular and irregular sea states.

6.2.1 Regular sea states

We report the results for each of the regular sea states studied. For every sea state, we present the optimization for the parameters K and C alone, and both K and C simultaneously.

Sea state ***Reg.1***

In fig. 6.5 are shown the results for the optimization of K, while fig. 6.6 reports the results for the optimization of C.

It is possible to observe that all the algorithms tested converge to the optimal values in the case of a single parameter optimization.
In fig. 6.7 are presented the results for the optimization of both the PTO parameters at the same time (the self-driving algorithm is not consistently convergent, thus the results associated are not shown).

Fig. 6.7 shows the convergence history of K and C coefficients using four ES algorithms for the regular sea state “Reg.1”. As can be seen in the figure, all four algorithms converge to the optimum values of the PTO coefficients. Moreover, their convergence behavior is similar to the mechanical oscillator problem of Sec. 3.1. Similar to the mass-spring-damper case, the self-driving ES method did not converge for the two-parameter optimization problem. However, oscillation-free steady-state solutions are obtained, when self-driving ES is used to optimize either K or C. The single-parameter optimization results using self-driving ES method are shown in Fig. 6.8.

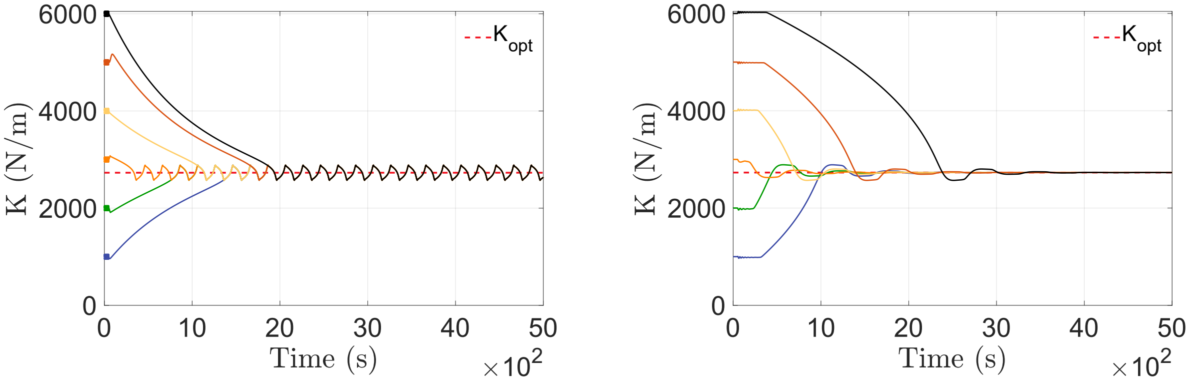

(a) Sliding mode ES (b) Self-driving ES

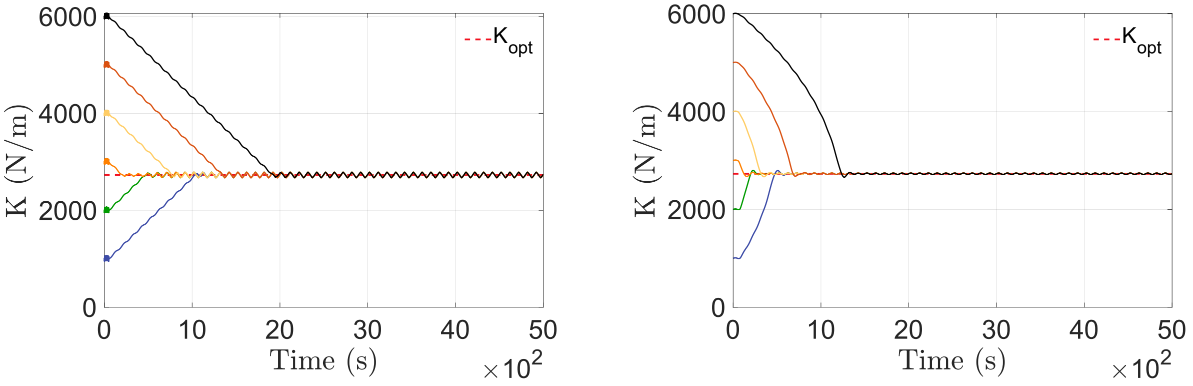

(c) Relay ES (d) LSQ-ES

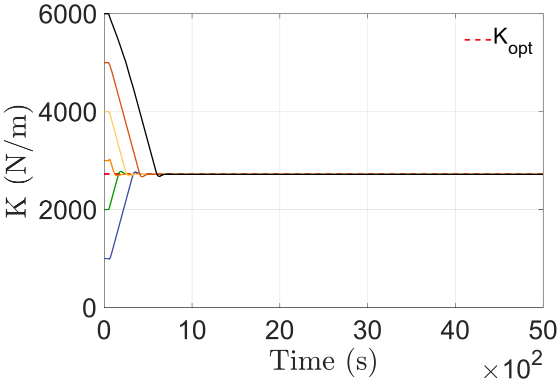

(e) Perturbation-based ES

Figure 6.1: Optimization of reactive coefficient K at a fixed value of resistive coefficient $C = C_{\text{opt}}$ for the mass-spring-damper system using different ES algorithms. The optimal $K_{\text{opt}} = 2729$ N/m value is indicated by the dashed line in the plots.

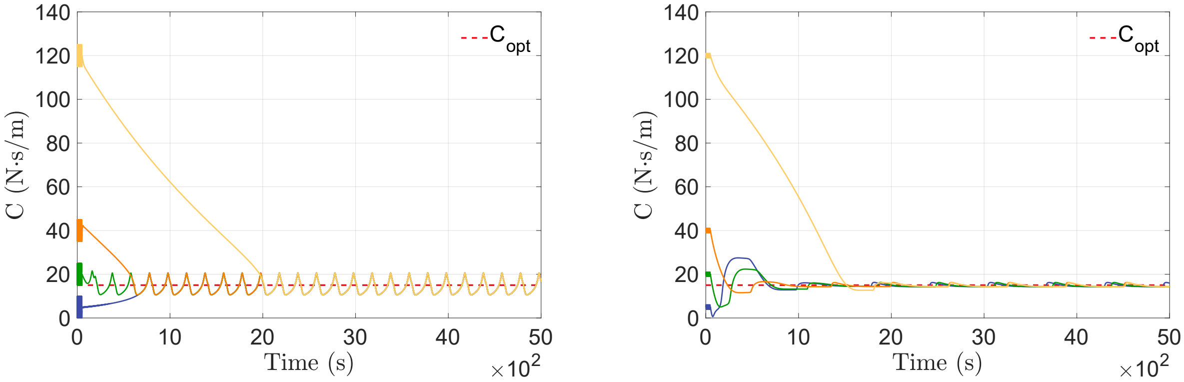

(a) Sliding mode ES

(b) Self-driving ES

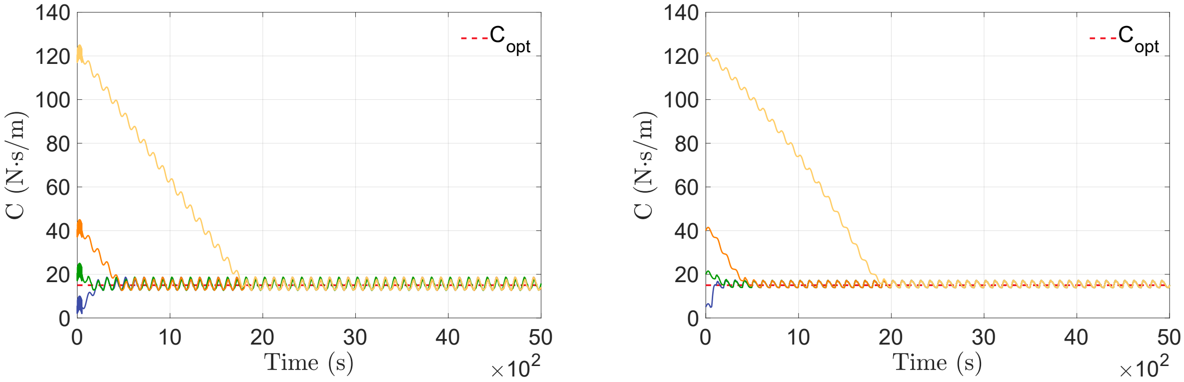

(c) Relay ES

(d) LSQ-ES

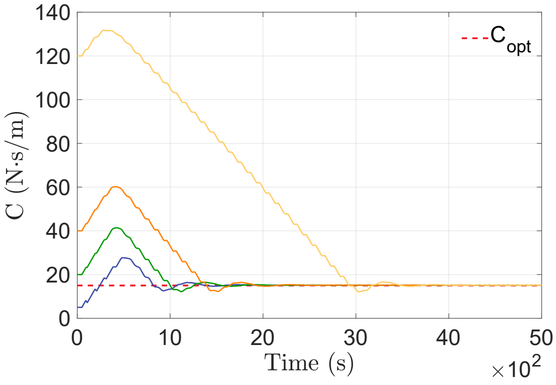

(e) Perturbation-based ES

Figure 6.2: Optimization of resistive coefficient C at a fixed value of reactive coefficient $K = K_{\text{opt}}$ for the mass-spring-damper system using different ES algorithms. The optimal $C_{\text{opt}} = 15$ N·s/m value is indicated by the dashed line in the plots.

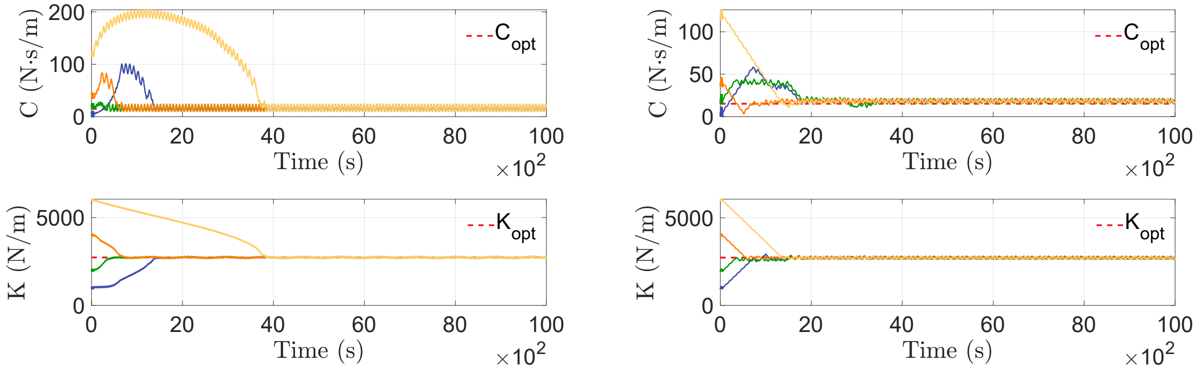

(a) Sliding mode ES

(b) Relay ES

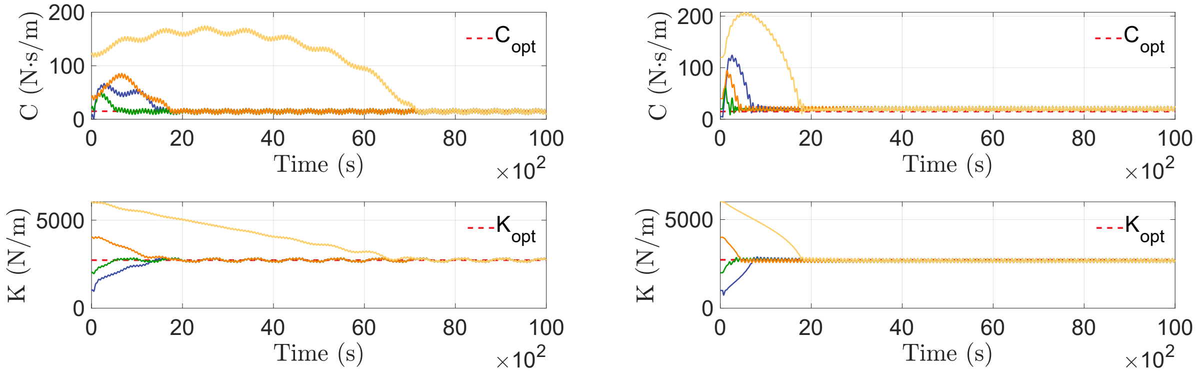

(c) LSQ-ES

(d) Perturbation-based ES

Figure 6.3: Optimization of reactive and resistive coefficients, K and C, respectively, for the mass-spring-damper system using different ES algorithms. The optimal $K_{\text{opt}} = 2729$ N/m and $C_{\text{opt}} = 15$ N·s/m values are indicated by dashed lines in the plots.

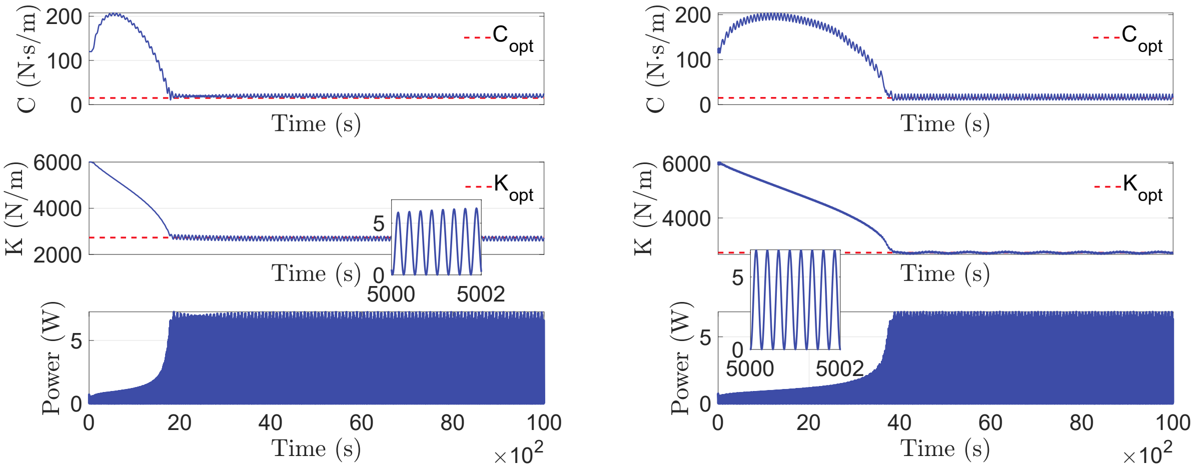

(a) Perturbation-based ES

(b) Sliding mode ES

Figure 6.4: Extracted power $P(t)$ during reactive a resistive coefficients optimization using (a) perturbation-based ES, and (b) sliding mode ES.

Finally, we confront the oscillations in the power extracted, confronting the perturbation-based and the sliding mode algorithms, which present a different behavior in terms of steady-state oscillations.

The differences in terms of oscillations of the extracted power $P(t)$ are not significant moving from perturbation-based to sliding mode. This demonstrates that the algorithm used does not have a significant impact on the performance of the system in terms of stability of the power extraction.

Sea state *Reg.2*

In fig. 6.10 are shown the results for the optimization of K, while fig. 6.11 reports the results for the optimization of C.

Also for sea state *Reg.2* all the algorithms tested converge to the optimal values in the case of a single parameter optimization.

In fig. 6.12 are presented the results for the optimization of both the PTO parameters at the same time (the self-driving algorithm is not consistently convergent, thus the results associated are not shown).

Also in this case, the algorithms lead to the optimization of both the PTO parameters at the same time.

For brevity, results regarding the oscillations analysis of $P(t)$ for sea state *Reg.2* are not presented, being analogous to the ones shown for sea state *Reg.1*.

Sea state *Reg.3*

In fig. 6.13 are shown the results for the optimization of K, while fig. 6.14 reports the results for the optimization of C.

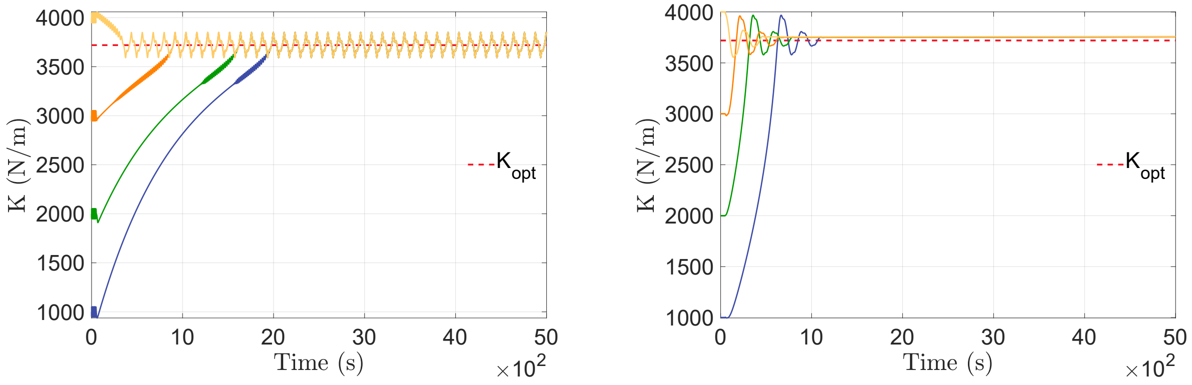

(a) Sliding mode ES

(b) Self-driving ES

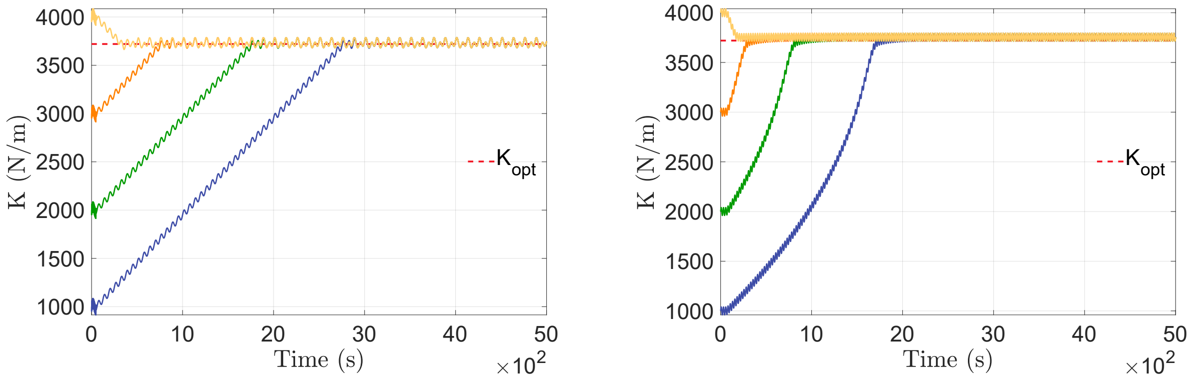

(c) Relay ES

(d) LSQ-ES

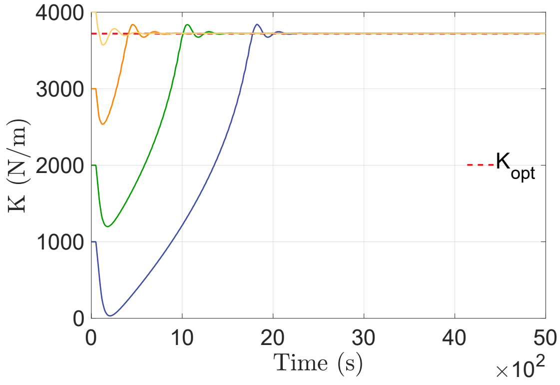

(e) Perturbation-based ES

Figure 6.5: Optimization of reactive coefficient K at a fixed value of reactive coefficient $C = C_{\text{opt}}$ for the cylindrical PA, with sea state *Reg.1*, using different ES algorithms. The optimal $K_{\text{opt}} = 3720$ N/m value is indicated by the dashed line in the plots.

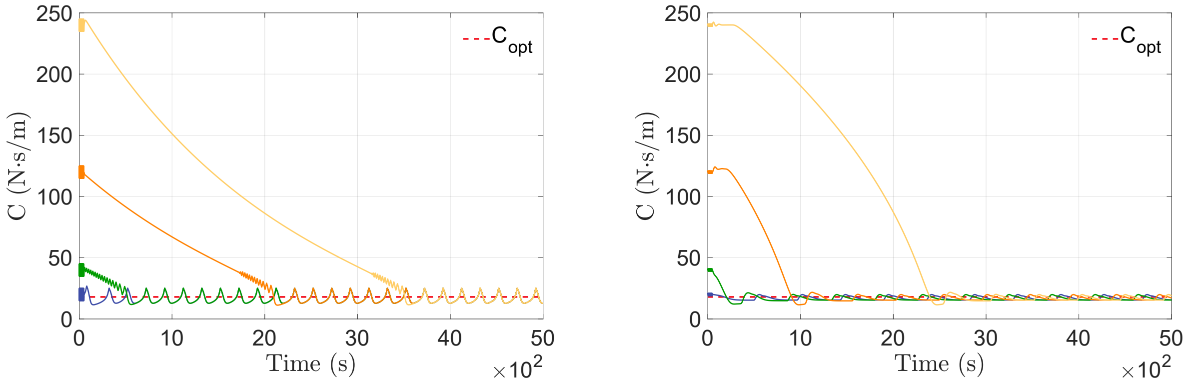

(a) Sliding mode ES

(b) Self-driving ES

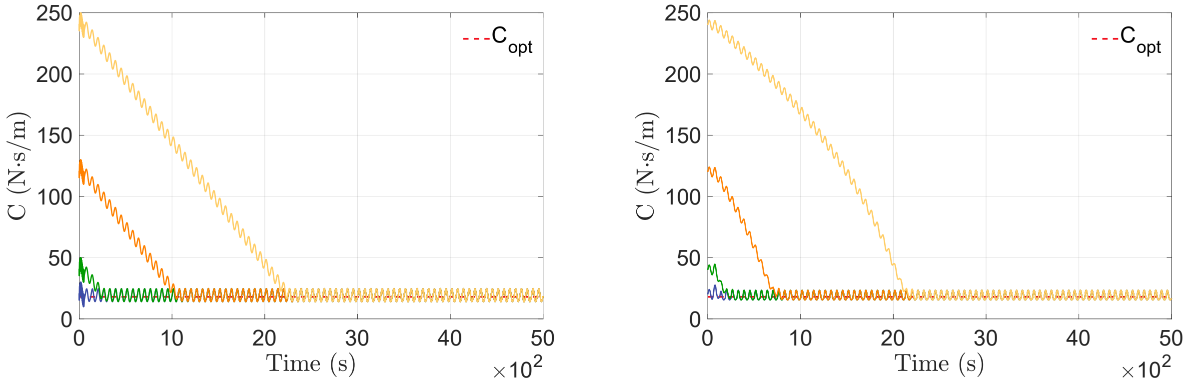

(c) Relay ES

(d) LSQ-ES

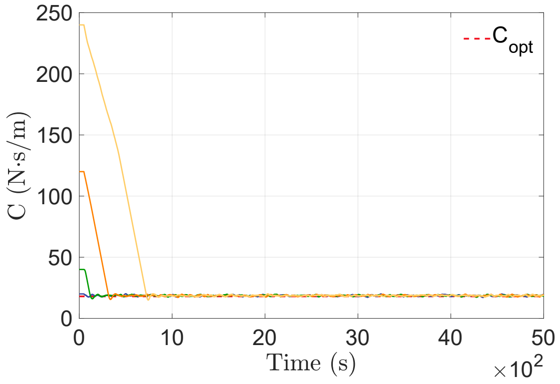

(e) Perturbation-based ES

Figure 6.6: Optimization of resistive coefficient C at a fixed value of reactive coefficient $K = K_{\text{opt}}$ for the cylindrical PA, with sea state *Reg.1*, using different ES algorithms. The optimal $C_{\text{opt}} = 18$ N·s/m value is indicated by the dashed line in the plots.

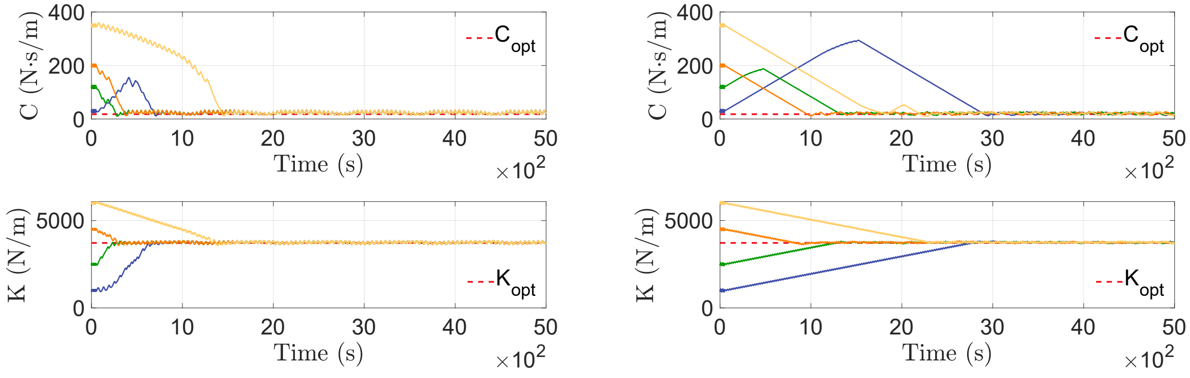

(a) Sliding mode ES

(b) Relay ES

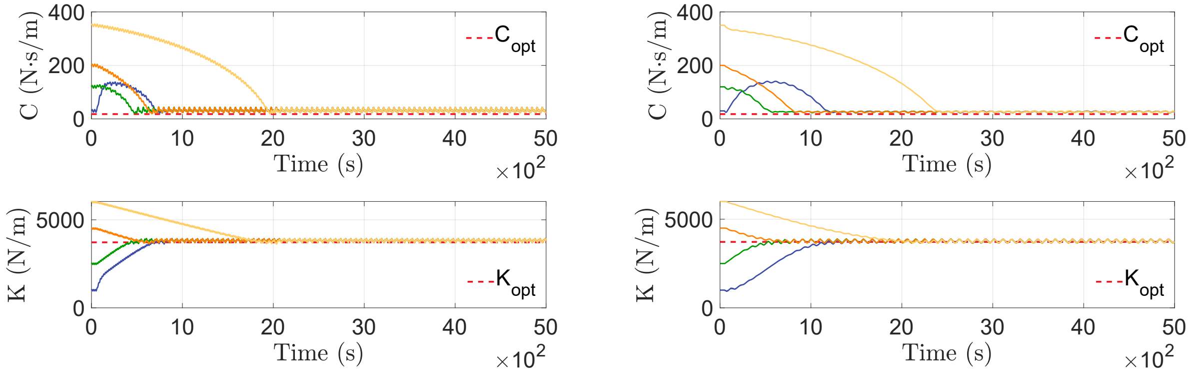

(c) LSQ-ES

(d) Perturbation-based ES

Figure 6.7: Optimization of reactive and resistive coefficients, K and C, respectively, for the cylindrical buoy in regular sea "Reg.1" using different ES algorithms. The optimal $K_{\text{opt}} = 3720$ N/m and $C_{\text{opt}} = 18$ N·s/m values are indicated by dashed lines in the plots.

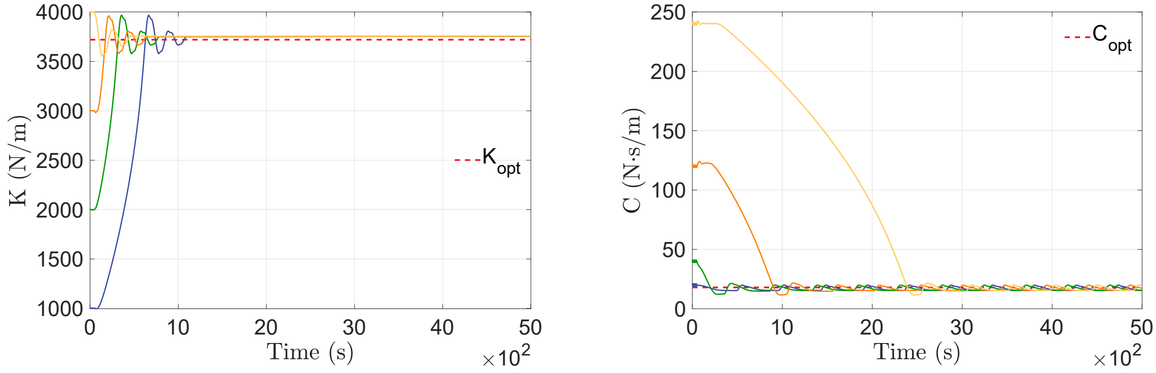

Figure 6.8: Optimization of (a) reactive PTO coefficient K; and (b) resistive PTO coefficient C using self-driving ES algorithm for cylindrical buoy in the regular sea "Reg.1". The optimal $K_{\text{opt}} = 3720$ N/m and $C_{\text{opt}} = 18$ N·s/m values are indicated by dashed lines in the plots.

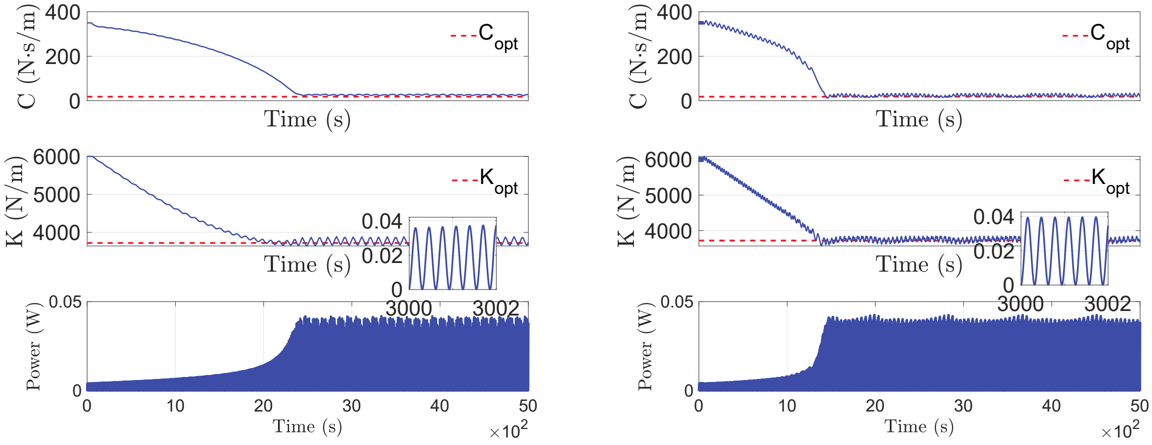

(a) Perturbation-based

(b) Sliding Mode

Figure 6.9: Extracted power $P(t)$ during reactive and resistive coefficients optimization using (a) perturbation-based ES, and (b) sliding mode ES algorithm for cylindrical buoy in the regular sea “Reg.1”. The optimal $K_{\text{opt}} = 3720$ N/m and $C_{\text{opt}} = 18$ N·s/m values are indicated by dashed lines in the plots.

Also for sea state *Reg.3* all the algorithms tested converge to the optimal values in the case of a single parameter optimization.
In fig. 6.15 are presented the results for the optimization of both the PTO parameters at the same time (the self-driving algorithm is not consistently convergent, thus the results associated are not shown).

Also in this case, the algorithms lead to the optimization of both the PTO parameters at the same time.
For brevity, results regarding the oscillations analysis of $P(t)$ for sea state *Reg.3* are not presented, being analogous to the ones shown for sea state *Reg.1*.

Sea states succession

We now demonstrate that the ES schemes proposed are able to adapt to changing sea conditions. The simulation proposed is divided into three equal parts. It starts with a wave described by the sea state *Reg.1*, and then moves to the states *Reg.2* and *Reg.3*. The results are shown in fig. 6.16.

The figure shows that all four ES algorithms can reliably adapt to the changing wave conditions, and adjust the PTO coefficients automatically to achieve optimal performance in each sea state. The results also confirm that extremum-seeking control algorithms do not require any wave forecasting/prediction information to attain the optimum. Indeed, the performance function used in the extremum-seeking algorithm, requires only on-board instrumentation to estimate the absorbed PTO power. Thus, ES can be used as a causal controller for WECs.

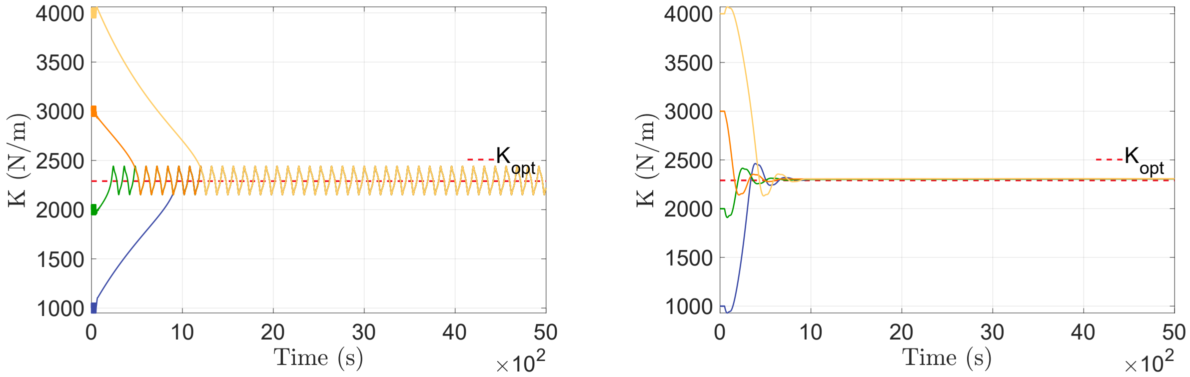

(a) Sliding mode ES

(b) Self-driving ES

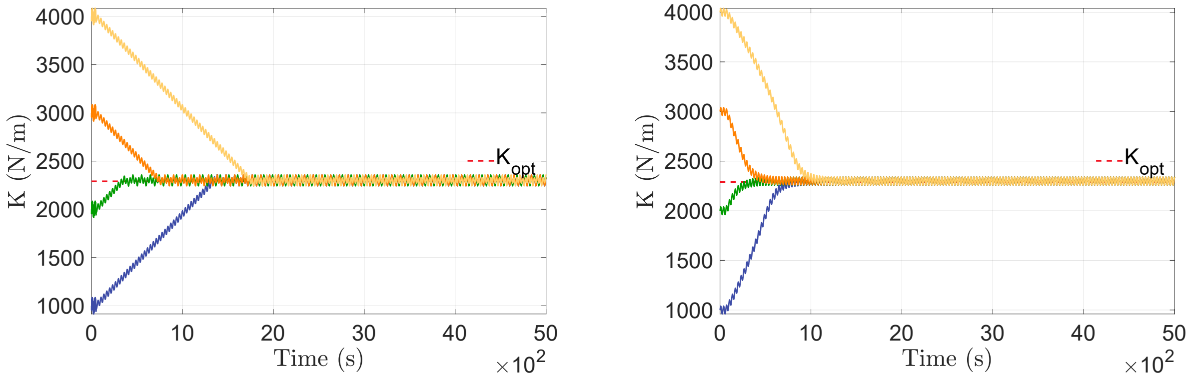

(c) Relay ES

(d) LSQ-ES

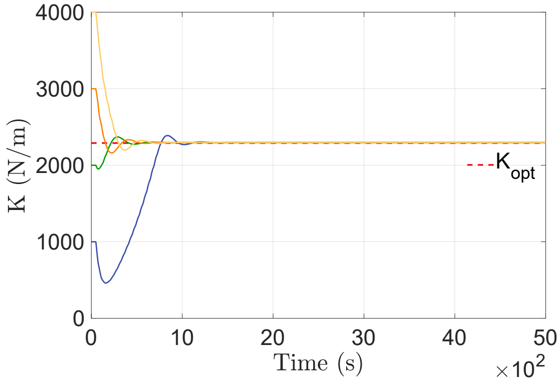

(e) Perturbation-based ES

Figure 6.10: Optimization of reactive coefficient K at a fixed value of reactive coefficient $C = C_{\text{opt}}$ for the cylindrical PA, with sea state *Reg.2*, using different ES algorithms. The optimal $K_{\text{opt}} = 2290$ N/m value is indicated by the dashed line in the plots.

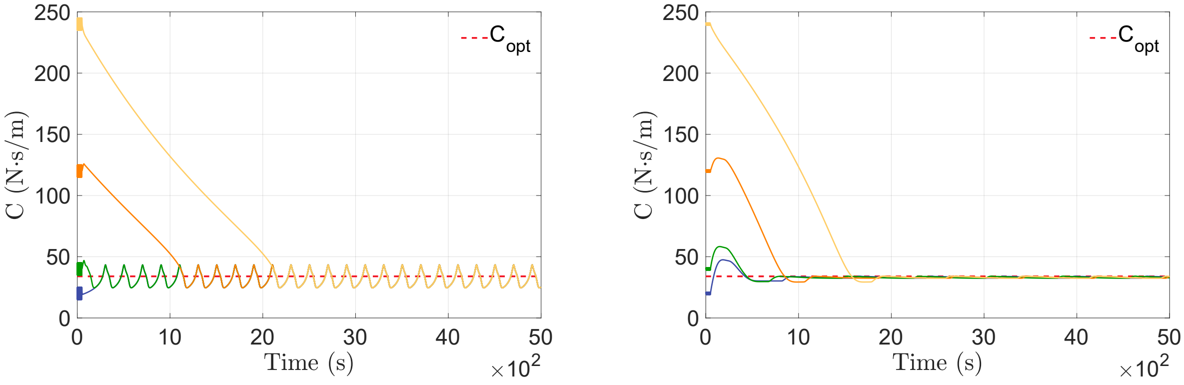

(a) Sliding mode ES (b) Self-driving ES

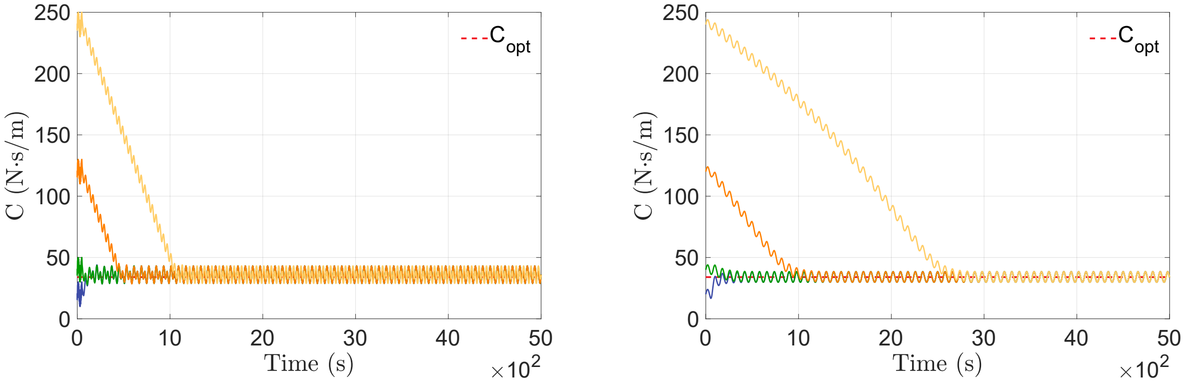

(c) Relay ES (d) LSQ-ES

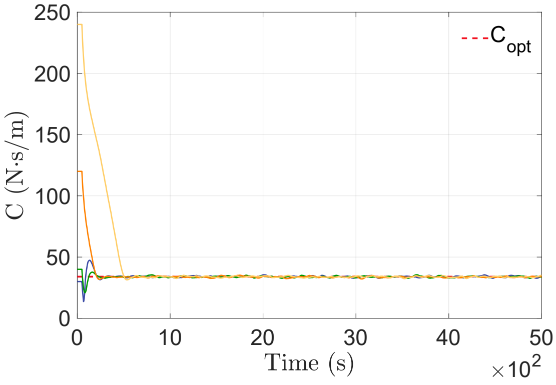

(e) Perturbation-based ES

Figure 6.11: Optimization of resistive coefficient C at a fixed value of reactive coefficient $K = K_{\text{opt}}$ for the cylindrical PA, with sea state *Reg.2*, using different ES algorithms. The optimal $C_{\text{opt}} = 34$ N·s/m value is indicated by the dashed line in the plots.

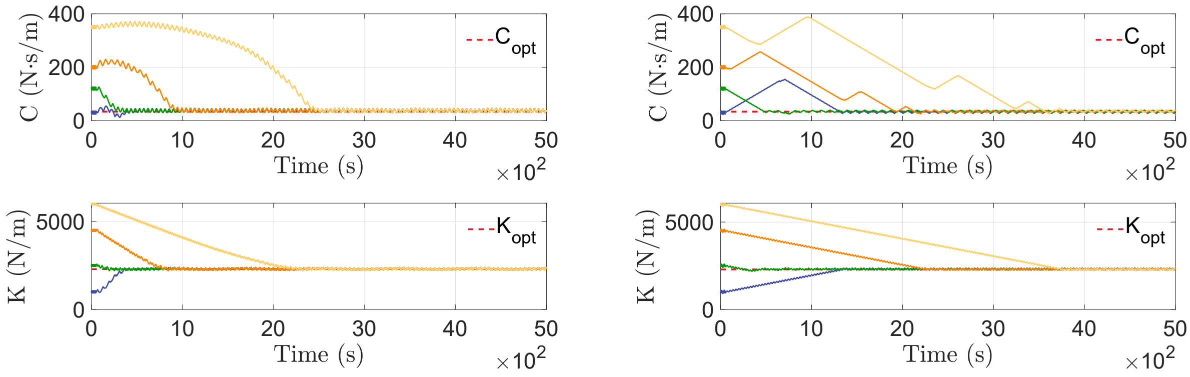

(a) Sliding mode ES (b) Relay ES

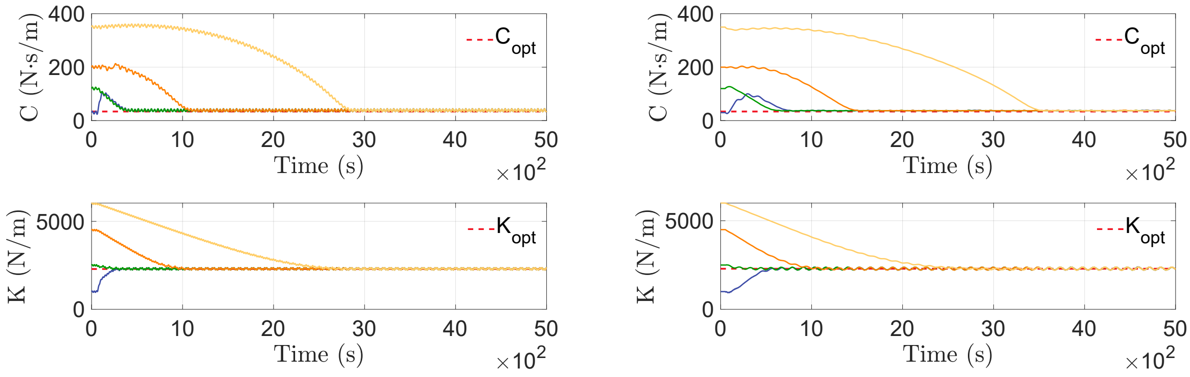

(c) LSQ-ES (d) Perturbation-based ES

Figure 6.12: Optimization of reactive and resistive coefficients, K and C, respectively, for the cylindrical buoy in regular sea "Reg.2" using different ES algorithms. The optimal $K_{\text{opt}} = 2290$ N/m and $C_{\text{opt}} = 34$ N·s/m values are indicated by dashed lines in the plots.

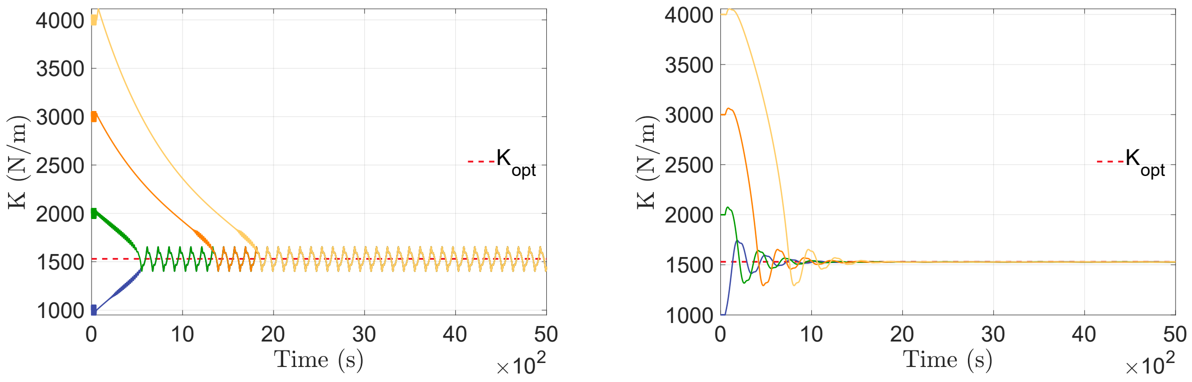

(a) Sliding mode ES

(b) Self-driving ES

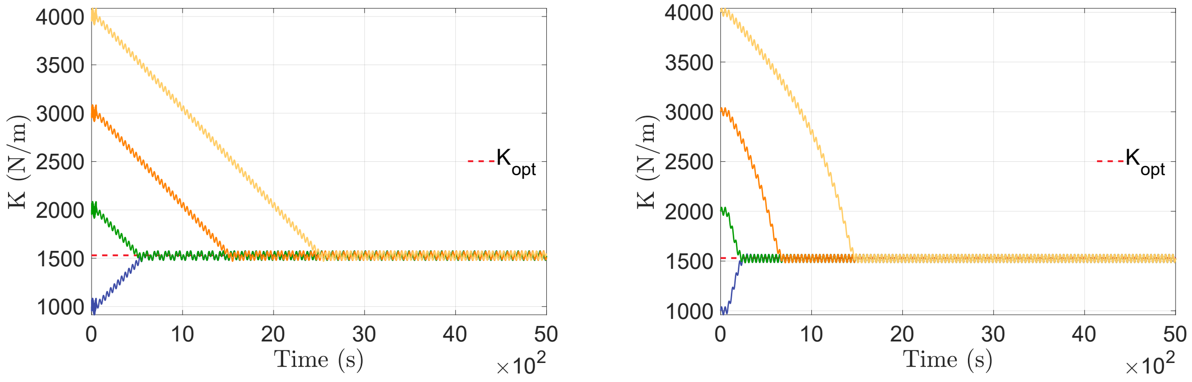

(c) Relay ES

(d) LSQ-ES

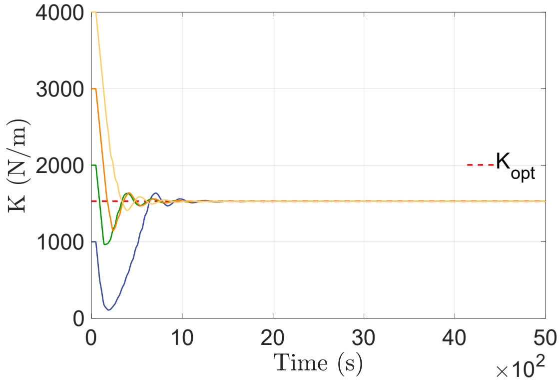

(e) Perturbation-based ES

Figure 6.13: Optimization of reactive coefficient K at a fixed value of reactive coefficient $C = C_{\text{opt}}$ for the cylindrical PA, with sea state *Reg.3*, using different ES algorithms. The optimal $K_{\text{opt}} = 1530$ N/m value is indicated by the dashed line in the plots.

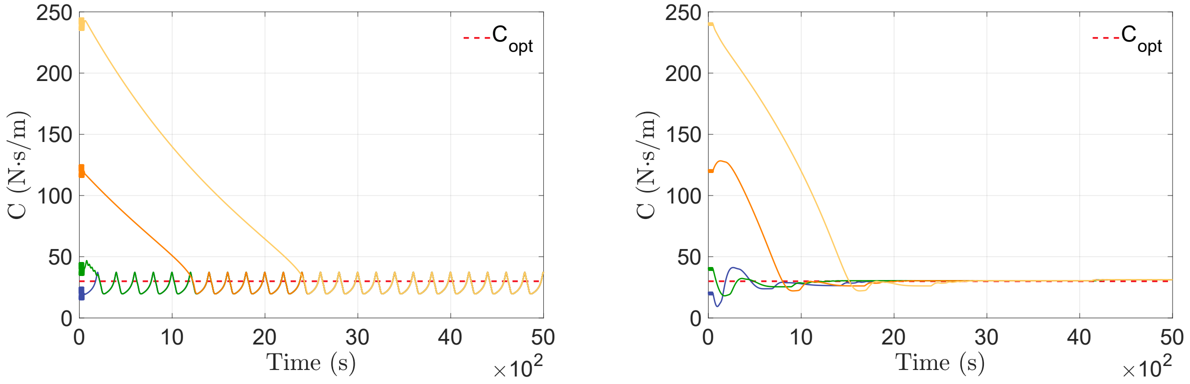

(a) Sliding mode ES

(b) Self-driving ES

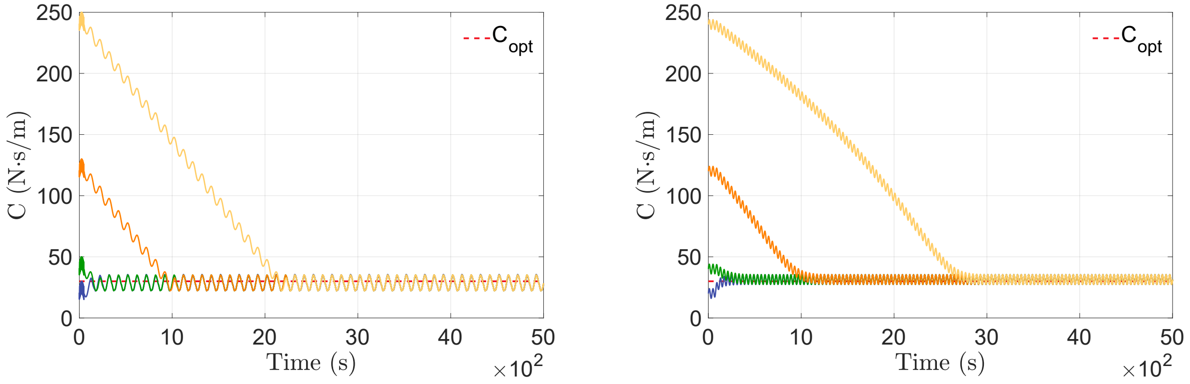

(c) Relay ES

(d) LSQ-ES

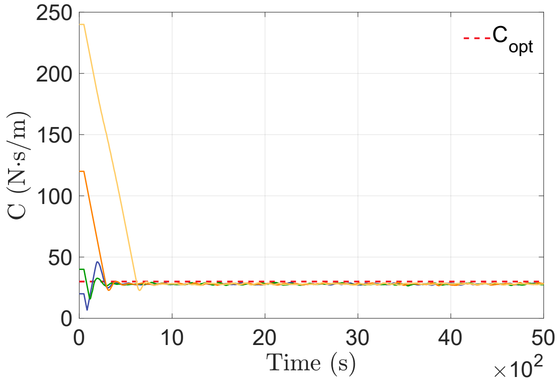

(e) Perturbation-based ES

Figure 6.14: Optimization of resistive coefficient C at a fixed value of reactive coefficient $K = K_{\text{opt}}$ for the cylindrical PA, with sea state *Reg.3*, using different ES algorithms. The optimal $C_{\text{opt}} = 30$ N·s/m value is indicated by the dashed line in the plots.

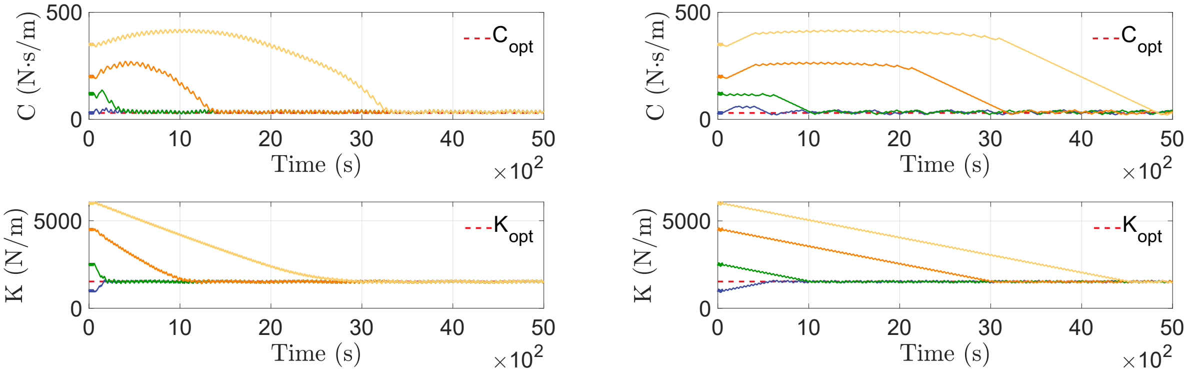

(a) Sliding mode ES (b) Relay ES

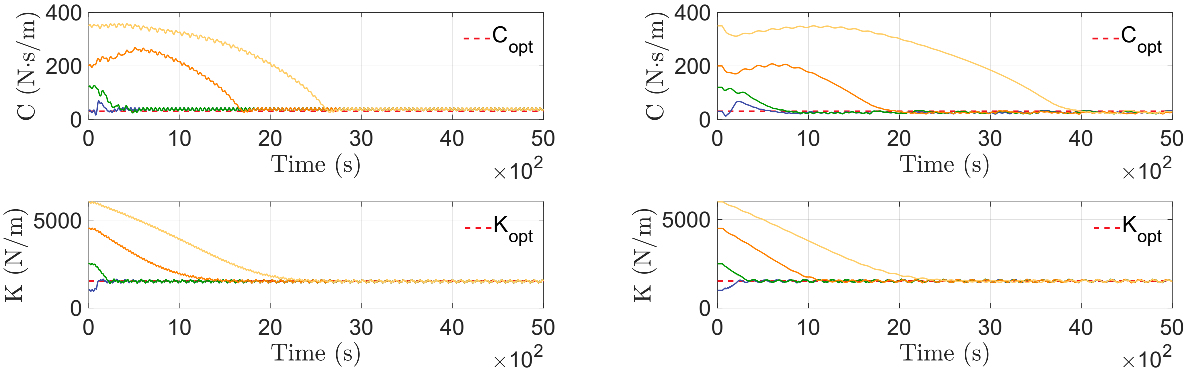

(c) LSQ-ES (d) Perturbation-based ES

Figure 6.15: Optimization of reactive and resistive coefficients, K and C, respectively, for the cylindrical buoy in regular sea “Reg.3” using different ES algorithms. The optimal $K_{\text{opt}} = 1530$ N/m and $C_{\text{opt}} = 30$ N·s/m values are indicated by dashed lines in the plots.

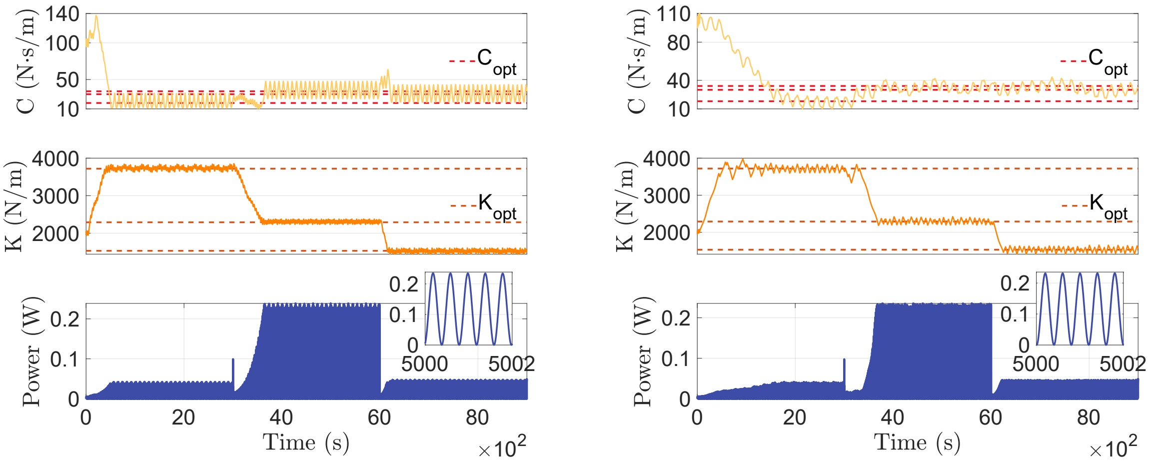

(a) Sliding mode ES (b) Relay ES

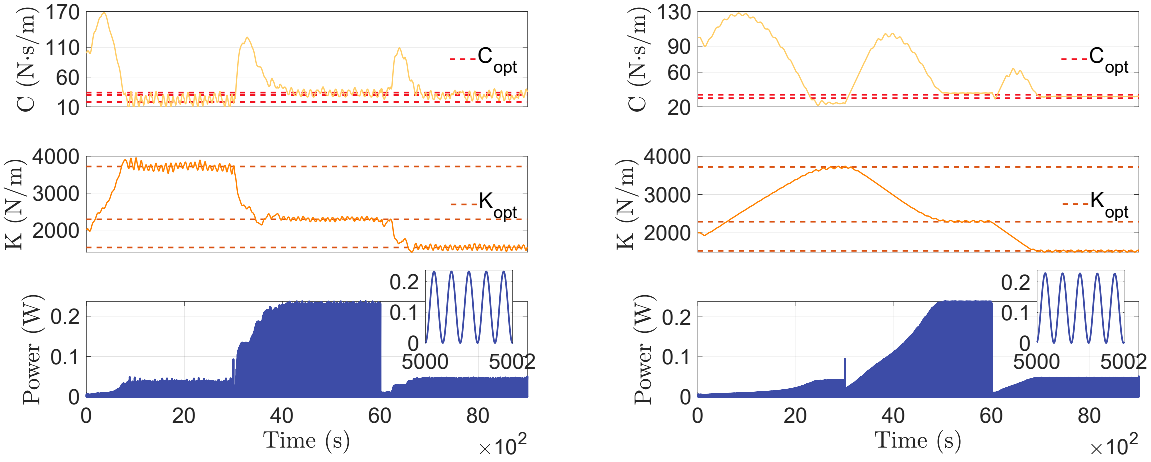

(c) LSQ-ES (d) Perturbation-based ES

Figure 6.16: Optimization of reactive and resistive coefficients, K and C, respectively, for the cylindrical buoy subject to changing sea states using different ES algorithms. The optimal K_{opt} and C_{opt} values in three different sea states from Table 5.2 are indicated by dashed lines in the plots.

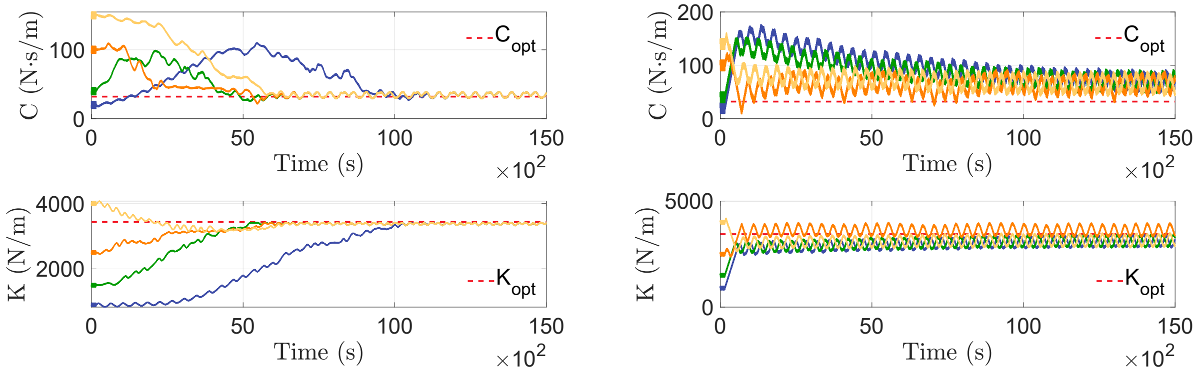

(a) Sliding mode ES (b) Relay ES

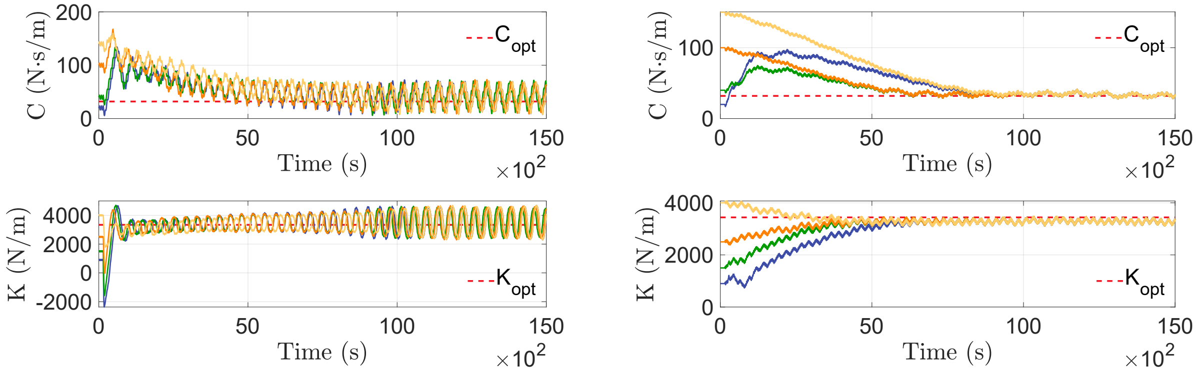

(c) LSQ-ES (d) Perturbation-based ES

Figure 6.17: Optimization of reactive and resistive coefficients, K and C, respectively, for the cylindrical buoy operating in the irregular sea state “Irreg.1” using different ES algorithms. The optimal $K_{\text{opt}} = 3440$ N/m and $C_{\text{opt}} = 32$ N·s/m values are indicated by dashed lines in the plots.

6.2.2 Irregular sea states

After having studied the behavior of the ES algorithms in the case of regular waves for the cylindrical point absorber, we move to the irregular case, which has a more practical interest. We start analyzing the sea state *Irreg.1*, moving to *Irreg.3*, and for each of the sea states studied, for brevity, we present the results of the optimization of both the PTO parameters at the same time.

Figs. 6.17, 6.18, and 6.19 show the convergence history of K and C coefficients using four ES algorithms for sea states “Irreg.1”, “Irreg.2”, and “Irreg.3”, respectively. From the figures, it can be seen that the sliding mode and perturbation-based ES methods outperform the relay and LSQ-ES algorithms. The latter two methods display large oscillations in the steady-state solution. Between the relay and LSQ methods, the former has a better convergence rate. This can be attributed to the fact that the relay ES algorithm does not use the magnitude of the performance gradient, which is noisier compared to its regular sea

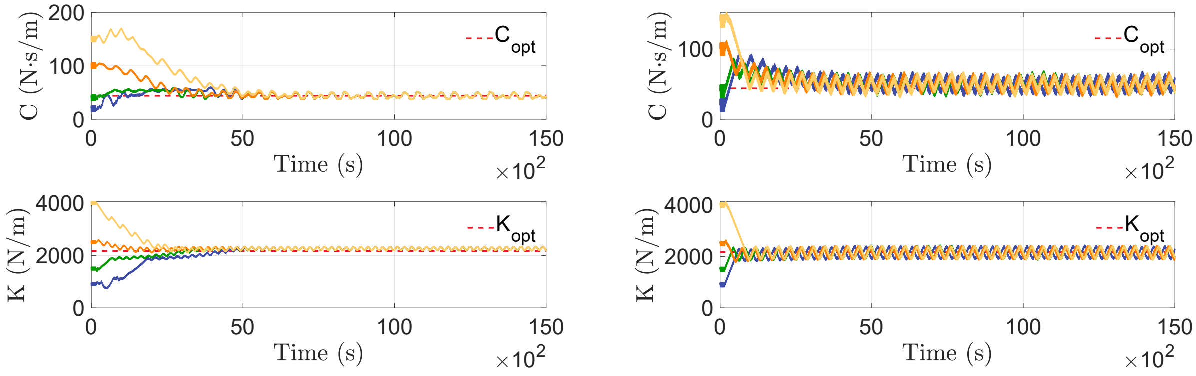

(a) Sliding mode ES

(b) Relay ES

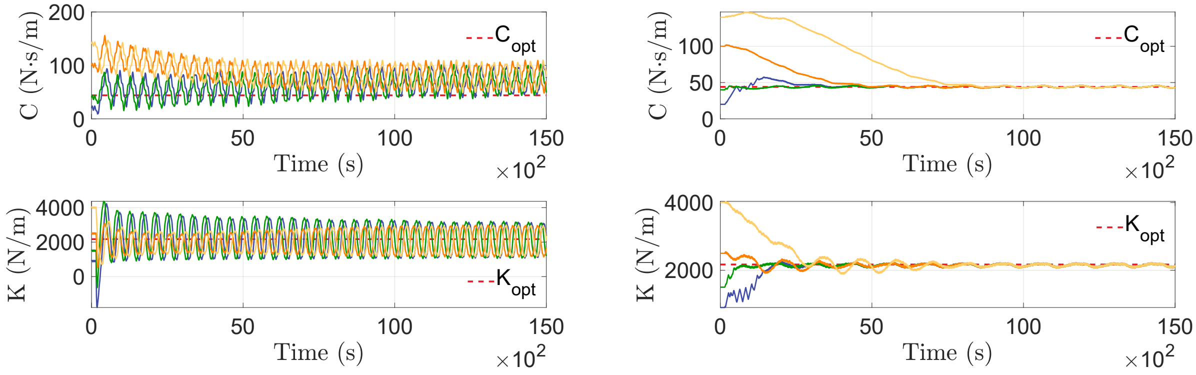

(c) LSQ-ES

(d) Perturbation-based ES

Figure 6.18: Optimization of reactive and resistive coefficients, K and C, respectively, for the cylindrical buoy operating in the irregular sea state "Irreg.2" using different ES algorithms. The optimal $K_{\text{opt}} = 2170$ N/m and $C_{\text{opt}} = 44$ N·s/m values are indicated by dashed lines in the plots.

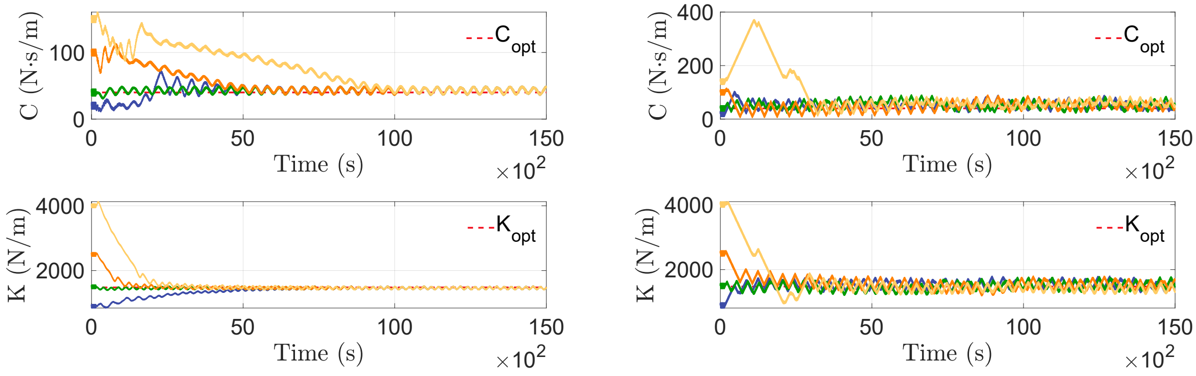

(a) Sliding mode ES

(b) Relay ES

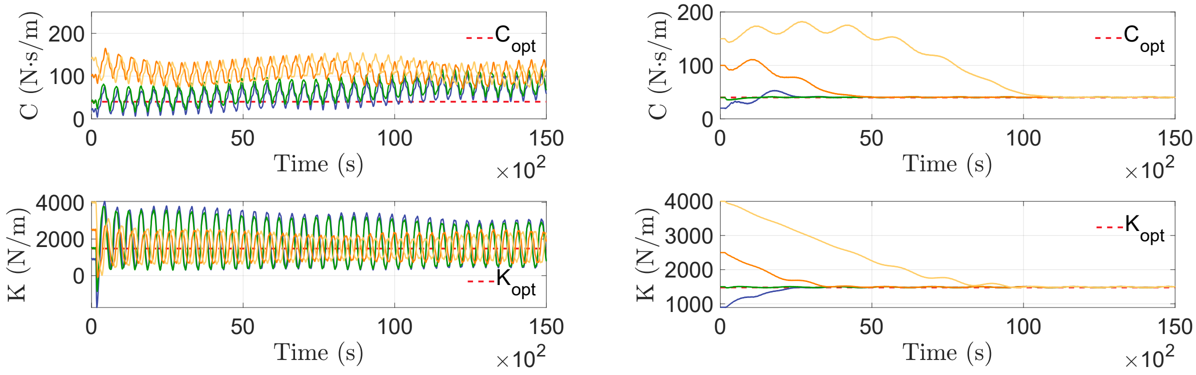

(c) LSQ-ES

(d) Perturbation-based ES

Figure 6.19: Optimization of reactive and resistive coefficients, K and C, respectively, for the cylindrical buoy operating in the irregular sea state "Irreg.3" using different ES algorithms. The optimal $K_{\text{opt}} = 1480$ N/m and $C_{\text{opt}} = 40$ N·s/m values are indicated by dashed lines in the plots.

state counterpart when computed through data buffers. However for regular waves, LSQ-ES convergence is better compared to the relay ES scheme because a more accurate gradient is available in this case; see Fig. 6.7.

For the irregular sea states, there is no need to analyze the concatenation of different sea states, as done for the regular waves, because each sea state already contains a whole spectrum of frequencies, and for this reason it is already demonstrated that the algorithms are able to converge to the optimum in presence of different frequency content of the incident wave. Moreover, the fact that the simulations converge starting from different initial values proves that the convergence is stable no matter of the initial value of the simulation (which can be seen as the optimum of a previous sea state).

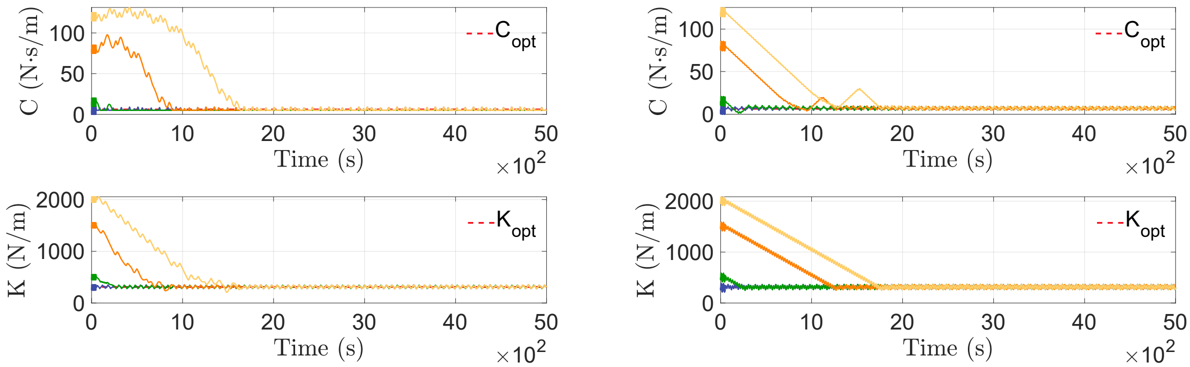

(a) Sliding mode ES

(b) Relay ES

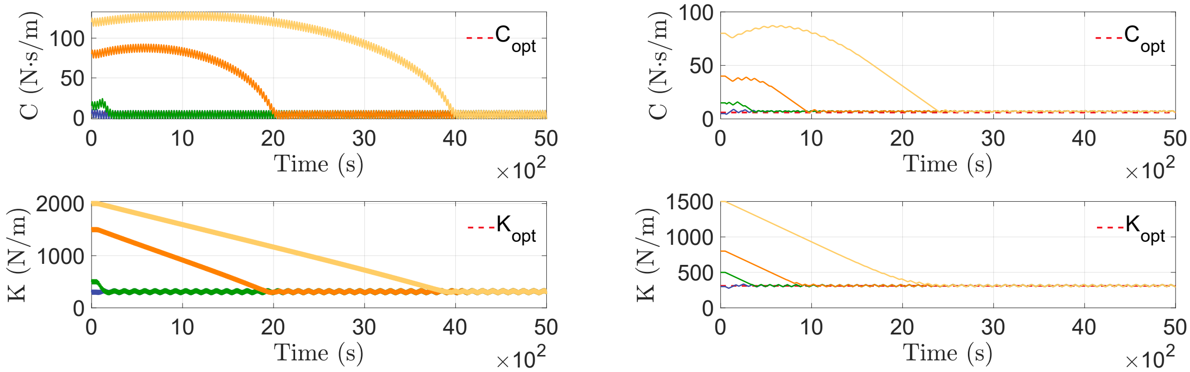

(c) LSQ-ES

(d) Perturbation-based ES

Figure 6.20: Optimization of reactive and resistive coefficients, K and C, respectively, for the spherical buoy operating in the regular sea state "Reg.1" using different ES algorithms. The optimal $K_{\text{opt}} = 310$ N/m and $C_{\text{opt}} = 6$ N·s/m values are indicated by dashed lines in the plots.

6.3 Spherical point-absorber

In the present section are reported the results for the optimization of the PTO parameters K and C for a spherical point absorber. For the sake of conciseness, we only present the results for the simultaneous optimization of K and C, being these of greater practical relevance. The simulations were conducted for both regular and irregular waves.

6.3.1 Regular sea states

We start analyzing the sea state *Irreg.1* (fig. 6.20), moving to *Irreg.2* (fig. 6.21) and *Irreg.3* (fig. 6.22), and for each of the sea states studied, we present the results of the optimization of both the PTO parameters at the same time.

The previous figures show the convergence history of K and C coefficients using four ES algorithms for the regular sea state "Reg.1". As can be seen in the figure, all four

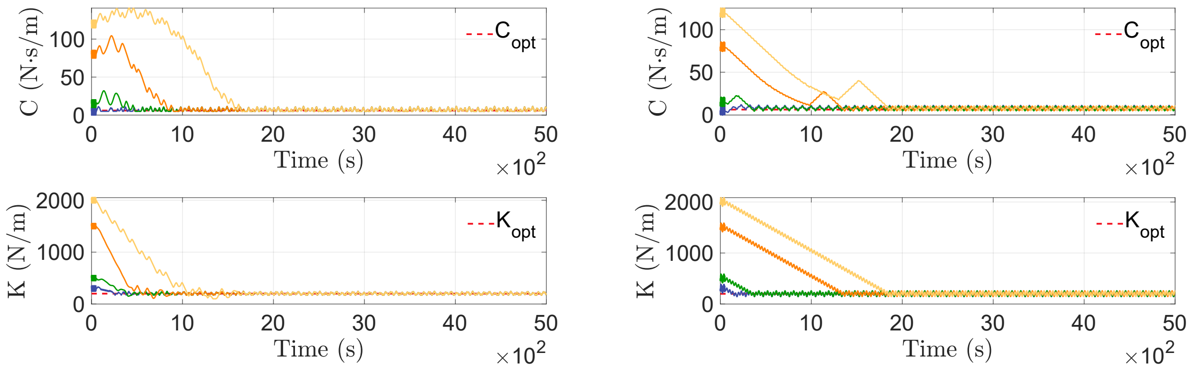

(a) Sliding mode ES

(b) Relay ES

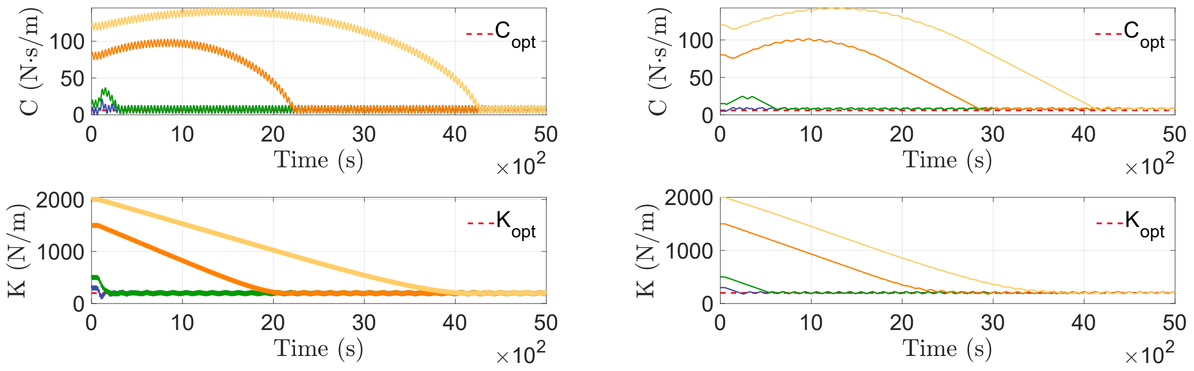

(c) LSQ-ES

(d) Perturbation-based ES

Figure 6.21: Optimization of reactive and resistive coefficients, K and C, respectively, for the spherical buoy operating in the regular sea state “Reg.2” using different ES algorithms. The optimal $K_{\text{opt}} = 200$ N/m and $C_{\text{opt}} = 6$ N·s/m values are indicated by dashed lines in the plots.

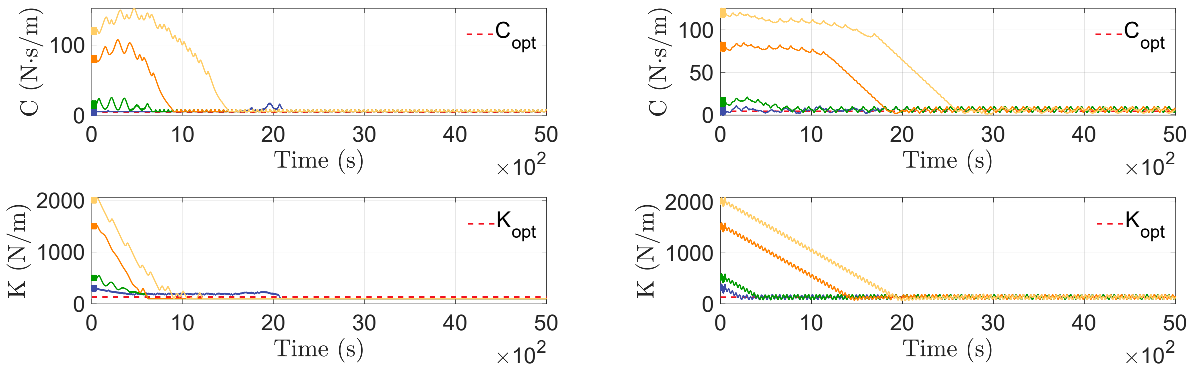

(a) Sliding mode ES

(b) Relay ES

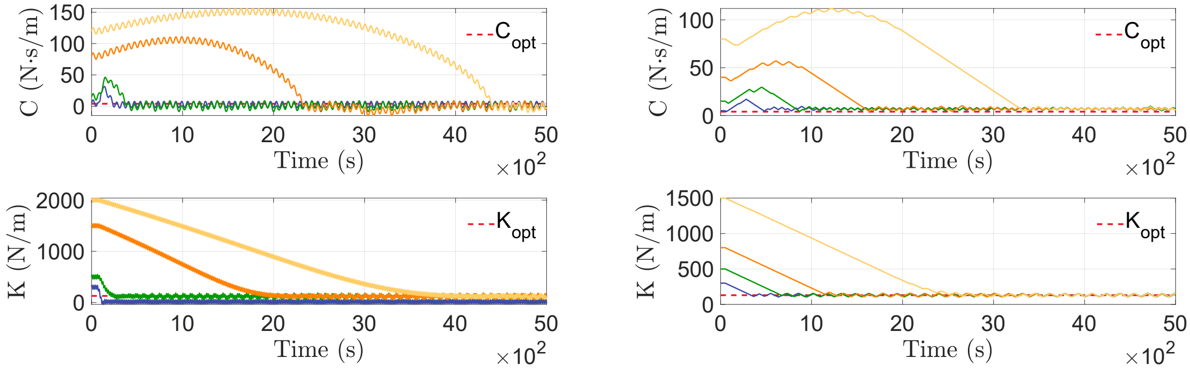

(c) LSQ-ES

(d) Perturbation-based ES

Figure 6.22: Optimization of reactive and resistive coefficients, K and C, respectively, for the spherical buoy operating in the regular sea state "Reg.3" using different ES algorithms. The optimal $K_{\text{opt}} = 130$ N/m and $C_{\text{opt}} = 4$ N·s/m values are indicated by dashed lines in the plots.

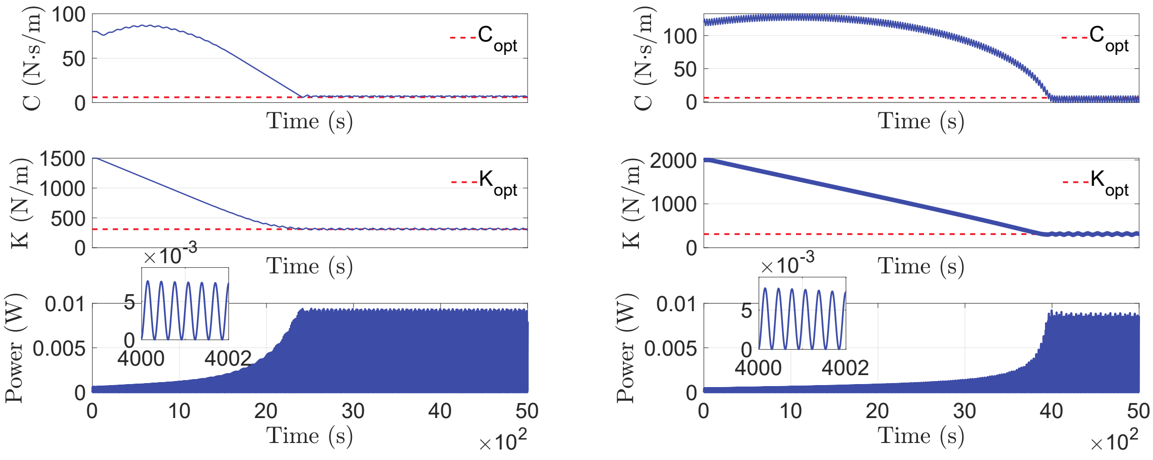

(a) Perturbation-based (b) LSQ

Figure 6.23: Extracted power $P(t)$ during reactive and resistive coefficients optimization using (a) perturbation-based ES, and (b) sliding mode ES algorithm for spherical buoy in the regular sea "Reg.1". The optimal $K_{\text{opt}} = 310$ N/m and $C_{\text{opt}} = 6$ N·s/m values are indicated by dashed lines in the plots.

algorithms converge to the optimum values of the PTO coefficients. Moreover, their convergence behavior is similar to the mechanical oscillator problem of Sec. 3.1. Similar to the mass-spring-damper case, the self-driving ES method did not converge for the two-parameter optimization problem.

Finally, we confront the oscillations in the power extracted, confronting the perturbation-based and the LSQ algorithms, which present a different behavior in terms of steady-state oscillations.

The differences in terms of oscillations of the extracted power $P(t)$ are not significant moving from perturbation-based to sliding mode. This demonstrates that the algorithm used does not have a significant impact on the performance of the system in terms of stability of the power extraction, although the LSQ algorithm in this case is much slower.

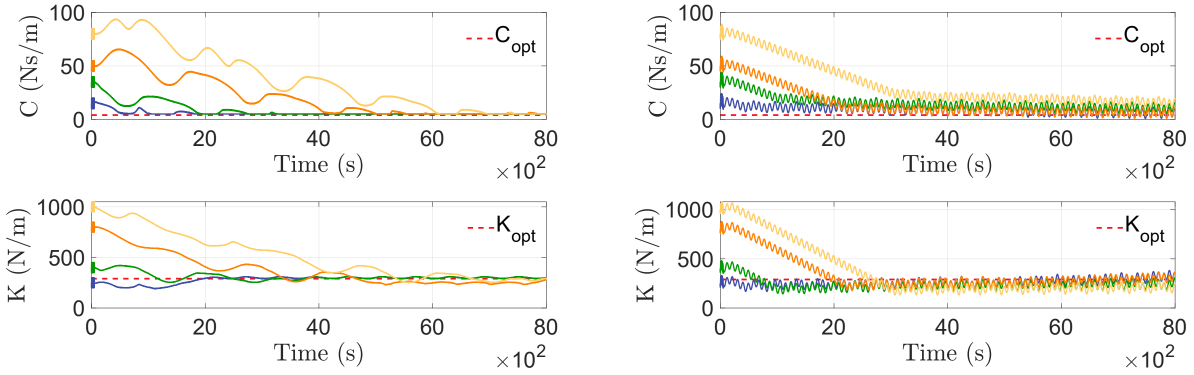

(a) Sliding mode ES (b) Relay ES

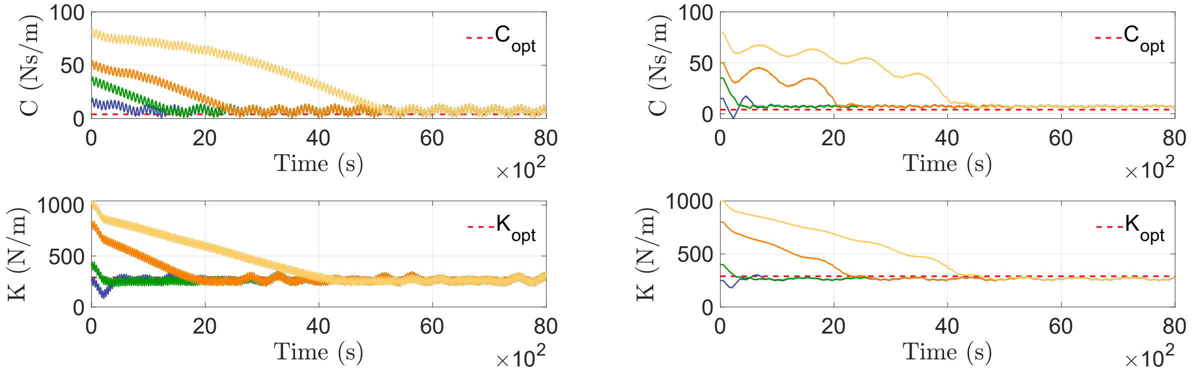

(c) LSQ-ES (d) Perturbation-based ES

Figure 6.24: Optimization of reactive and resistive coefficients, K and C, respectively, for the spherical buoy operating in the irregular sea state "Irreg.1" using different ES algorithms. The optimal $K_{\text{opt}} = 290$ N/m and $C_{\text{opt}} = 4$ N·s/m values are indicated by dashed lines in the plots.

6.3.2 Irregular sea states

In this section we present the results regarding the simultaneous optimization of the PTO parameters K and C for the irregular sea conditions presented in Sec. 5.1.2.

Figure 6.24 shows the convergence of the algorithms for the sea state *Irreg.1*, while figures 6.25 and 6.26 show the convergence for sea states *Irreg.2* and *Irreg.3*.

Although the convergence is more uncertain than the regular wave case, it is undoubtedly possible to state that the algorithms used converge also for an irregular sea state, and that the sliding mode and the perturbation-based converge with the least oscillations to the optimal values.

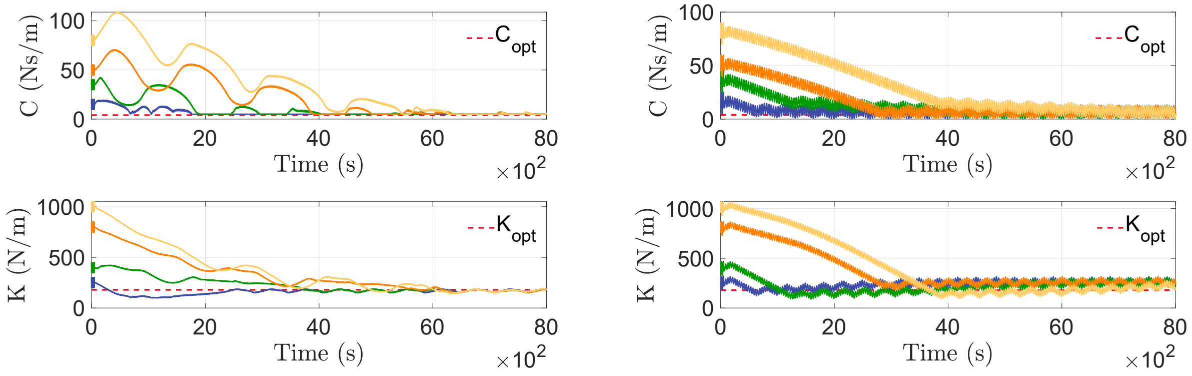

(a) Sliding mode ES

(b) Relay ES

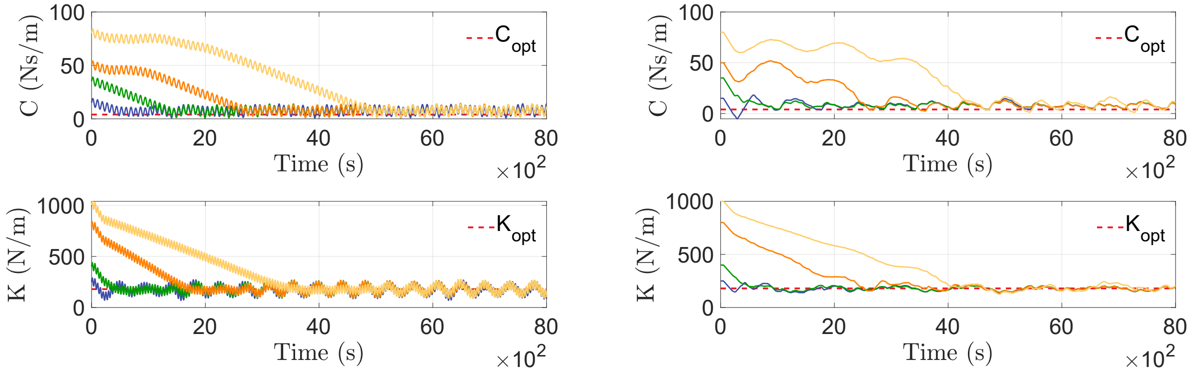

(c) LSQ-ES

(d) Perturbation-based ES

Figure 6.25: Optimization of reactive and resistive coefficients, K and C, respectively, for the spherical buoy operating in the irregular sea state "Irreg.2" using different ES algorithms. The optimal $K_{\text{opt}} = 180$ N/m and $C_{\text{opt}} = 4$ N·s/m values are indicated by dashed lines in the plots.

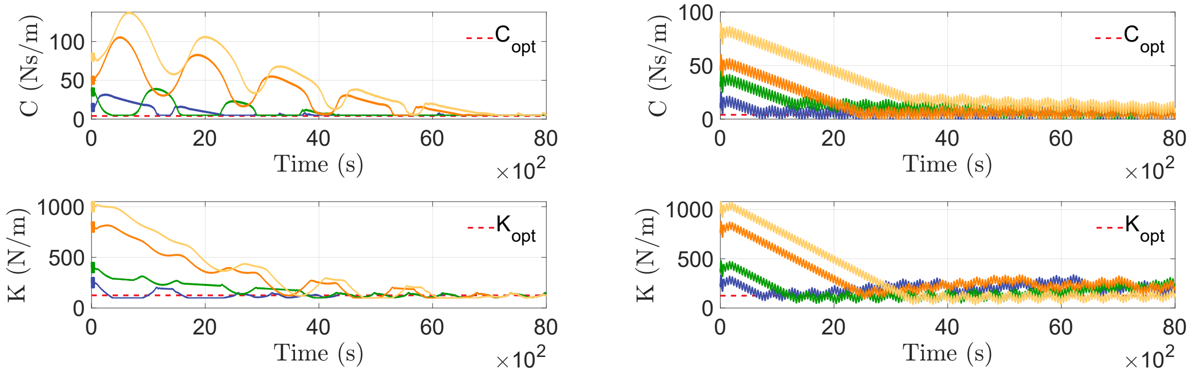

(a) Sliding mode ES

(b) Relay ES

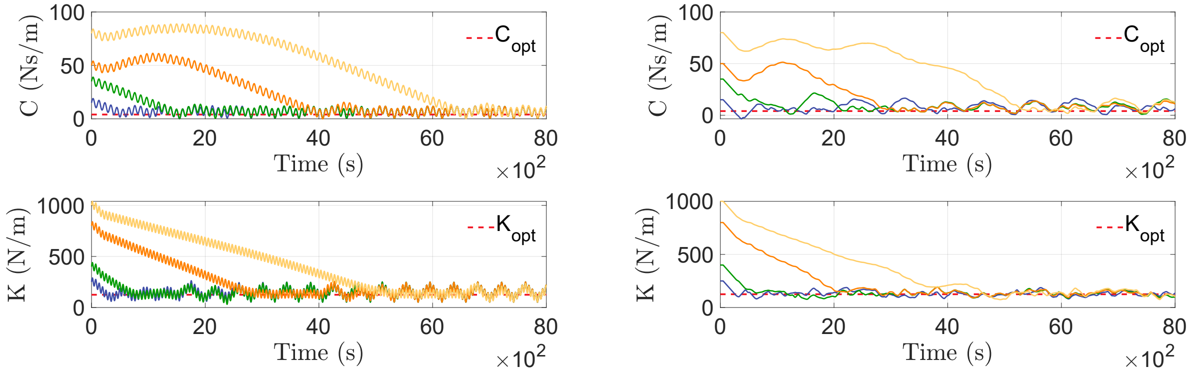

(c) LSQ-ES

(d) Perturbation-based ES

Figure 6.26: Optimization of reactive and resistive coefficients, K and C, respectively, for the spherical buoy operating in the irregular sea state "Irreg.3" using different ES algorithms. The optimal $K_{\text{opt}} = 125$ N/m and $C_{\text{opt}} = 4$ N·s/m values are indicated by dashed lines in the plots.

6.4 Considerations

Based upon the results obtained in this section, we make some remarks about different algorithms:

- The sliding mode ES proved quite robust, and did not require re-tuning of parameters for varying conditions like frequency and/or amplitude of the external force. Moreover, the number of parameters to tune are relatively small. A drawback of the scheme is that the steady-state solution oscillates near the optima, as seen in Fig. 6.1(a). This however, results in a negligible variation in the PTO power, as shown in Fig. 6.4, which compares the extracted power as a function of time using perturbation-based and sliding mode ES methods. The former controller produces negligible oscillation in the steady-state solution of K coefficient.

- The self-driving ES achieves convergence to the optimal value without steady-state oscillations. It is relatively robust, but the main drawback includes tuning of a large number of parameters. Also, it did not converge reliably for the multi-parameter optimization problem using the algorithm described in Sec. 4.3.2.

- The relay ES is also relatively insensitive to the frequency and/or amplitude variation of the external force. It is simple to tune as well. However, it also results in steady-state oscillations in the solution.

- The LSQ-ES proved more robust than the relay ES, having roughly the same number of parameters to tune. It also results in less oscillations in the steady-state solution compared to the relay ES, although they are not completely eliminated.

- Perturbation-based ES is one of the more popular ES schemes used in the literature. The main advantage of this method is its stability, although the choice of cut-off frequencies of the filters largely dictates its performance. The method can achieve a controlled amount of oscillation in the converged solution, as seen in Figs. 6.1(e) 6.2(e), and 6.3(d). The rate of convergence of this method also depends upon the frequency of the external perturbation signal used to estimate the gradient.

7. Conclusions

In this study, we systematically investigated the feasibility of ES control for wave energy converters to improve their conversion efficiency. Five different ES schemes were tested for heaving WECs: (i) sliding mode ES; (ii) relay ES; (iii) least-squares gradient ES; (iv) self-driving ES; and (v) perturbation-based ES. The optimization problem of wave energy absorption in WECs was formulated in terms of finding the optimal PTO coefficients. Alternatively, the ES optimization problem can also be formulated in terms of finding the optimal PTO force directly, as typically done in model predictive control (MPC) of WECs [62]. Direct optimization of PTO force using ES control is deferred to future endeavors.

The performance function for the ES control was defined as the power absorbed by the PTO system over a given period of time, which could be measured through on-board instrumentation, and does not require any wave measurements. Moreover, being ES a causal controller, it is not necessary to predict or forecast the behavior of the wave, and the optimal values for the PTO parameters can be obtained only using present and previous data.

The optimization results were verified against analytical solutions and the extremum of reference-to-output maps. The numerical results demonstrate that except for the self-driving ES algorithm, the other four ES schemes reliably converge for the two-parameter optimization problem. The self-driving ES is more suitable for optimizing a single-parameter of the problem, or when the objective is to find the optimal control force directly, rather than to optimize the gains of the control law. An advantage of the self-driving ES scheme is that it leads to oscillation-free steady-state solution. The results also show that for an irregular sea state, the sliding mode and perturbation-based ES schemes have better convergence to the optimum, in comparison to other ES schemes. The least-squares ES scheme performs better than the relay ES scheme, whenever the gradient estimation through data acquisition is smooth and accurate. This can be concluded by comparing the convergence history of LSQ-ES and relay ES for regular and irregular sea states; LSQ performed better than relay in the case of regular waves and the converse is true for irregular waves. For all ES schemes, the convergence of PTO coefficients towards the performance-optimal values are tested for widely different initial values, in order to avoid bias towards the extremum. We also demonstrated the adaptive capability of ES control, by considering a case, in which wave conditions were changed amidst the simulation, and the ES controller adapted to the new extremum automatically.

All extremum-seeking schemes achieve optimum within a single simulation. This allows for a possibility of using model-free ES algorithms within nonlinear computational fluid dynamics (CFD) framework to simulate wave-structure interaction of WECs. In the CFD literature, evolution-based optimization strategies (e.g. genetic algorithm) are predominantly used for solving optimization problems. However, such evolutionary strategies typically require a large number of function evaluations, which can be prohibitively expensive for fully-resolved wave structure interaction problems [69, 88]. We shall consider such an approach in the future.

Moreover, after having shown that the algorithms studied lead to the optimization of the plant performance, a further step could be to conduct an in-depth analysis of the performances of each algorithm, defining some indicators that could allow a comparison between the different approaches.

Finally, it is conceivable to introduce the force exerted by the mooring line in the definition of the performance/cost function, in order to limit the tension on the mooring lines, allowing a reduction on the weight and cost of the mooring line itself, while harvesting the most energy possible.

A. Appendix

A.1 Power components in performance function

In this section we confront the results obtained using two different definitions for the performance indicator: the first is the one which has been used for the study, and is described by (3.9), while the second definition of the performance indicator is given in (3.17), with f_{PTO} defined in (3.3). Thus we have that the first control approach uses only the damping component of the force exerted by the PTO, which is also the one responsible for the production of the power transferred to the grid, while the second approach also considers the component of the PTO force given by the spring, which does not contribute to the net production of power.

In particular we are proving that the two approaches lead to the same results, since the goal is always to obtain the best performance of the system in terms of extracted power. The comparison has been carried out for the cylindrical hull, using the perturbation based ES, in the cases of sea states Reg. 1 and Irreg. 1: the results are depicted in fig. A.1(a)-(b) and fig. A.1(c)-(d) respectively.

From the previous figures it is possible to numerically verify that including the reactive component of power in the performance function does not affect the optimal values of the PTO coefficients obtained from an ES control scheme. This was also demonstrated theoretically in Eq. (3.18).

Regular sea state Reg.1

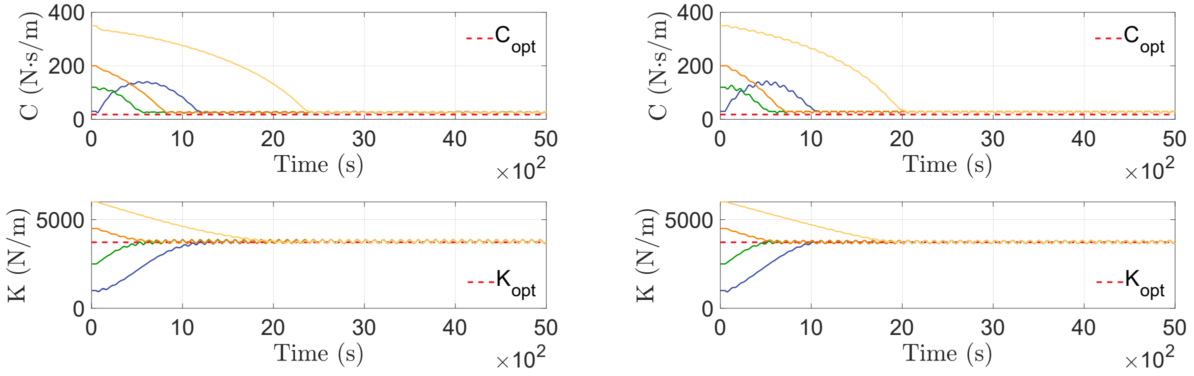

(a) Only resistive power

(b) Both reactive and resistive powers

Irregular sea state Irreg.1

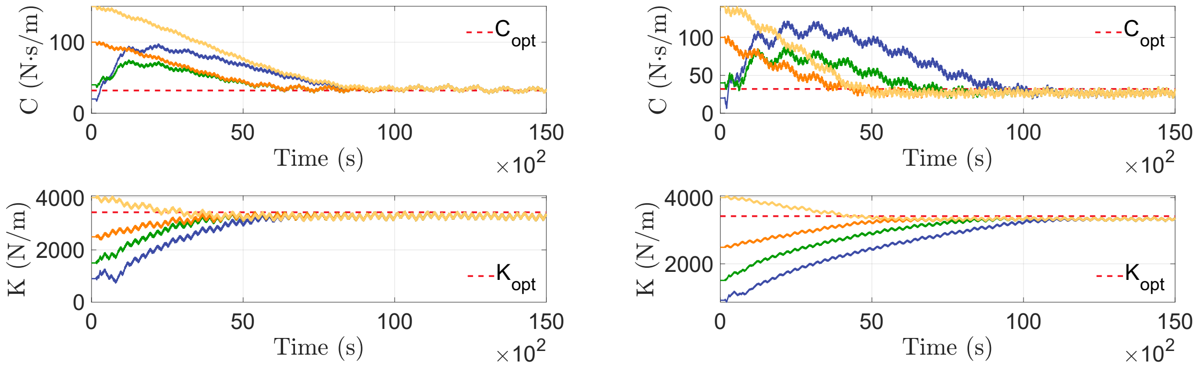

(c) Only resistive power

(d) Both reactive and resistive powers

Figure A.1: Optimization of reactive and resistive coefficients, K and C, respectively, for the cylindrical buoy in regular "Reg.1" (top row), and irregular "Irreg.1" (bottom row) waves, using different power components in the performance function. The optimal $K_{\text{opt}} = 3720$ N/m and $C_{\text{opt}} = 18$ N·s/m values for regular waves, and $K_{\text{opt}} = 3440$ N/m and $C_{\text{opt}} = 32$ N·s/m values for irregular waves are indicated by dashed lines in the plots.

A.2 Review of other control strategies for wave energy converters

In this section are reported some of the most commonly used control techniques for the optimization of the energy extracted by a wave energy converter.

In order to clarify the functioning of some of the following control systems, it is opportune to return to a simplified model of a PA, as done in Sec. 3.1. If the system is not controlled, we can write the equation of motion in the frequency domain as:

$$(-\omega^2 m + k + i\omega c)\bar{x}(i\omega) = \bar{f}_0(i\omega) \tag{A.1}$$

in which $\bar{f}_0(i\omega)$ represents the contribution in terms of magnitude and phase to the generalized external force for the particular frequency ω and $\bar{x}(i\omega)$ has the same meaning for the displacement, as discussed in Sec. 3.1.

If we define explicitly the body velocity as $u(t) = \dot{x}(t)$, it is possible to rewrite the previous equation in terms of Fourier transform as follows:

$$Z(\omega)\bar{u}(i\omega) = \bar{f}_0(i\omega) \tag{A.2}$$

in which $\bar{u}(i\omega)$ is the Fourier transform of the body velocity $u(t)$. Moreover, drawing a similarity between eq. A.2 and the complex form of Ohm's law, it is possible to conceive the term $Z(\omega)$ as a mechanical impedance, in analogy with the electric impedance.

Mechanical impedance is expressed by

$$Z(\omega) = c + i\left(\omega m - \frac{k}{\omega}\right). \tag{A.3}$$

If the system also comprehends a PTO, it is possible to extend eq. A.2 to

$$(Z(\omega) + \Lambda(\omega))\bar{u}(i\omega) = \bar{f}_0(i\omega) \tag{A.4}$$

where in general

$$\Lambda(\omega) = C + i\left(\omega M - \frac{K}{\omega}\right) \tag{A.5}$$

being C, M, K the coefficients of the generalized PTO force as stated in Sec. 3.1. For the purposes of our study we have $M = 0$.

We have already shown that in order to maximize the power extracted by the PTO, two conditions need to be satisfied: the resistive part of the load must be equal to the inherited resistance in the system (eq. 3.16), and the reactive component of the load has to eliminate the reactive effects due to the inherited mass and stiffness of the system (eq. 3.11). This corresponds to what in electrotechnics is called *impedance matching*.

According to Falnes [7], there are two main strategies to achieve this goal:

1) Complex conjugate control

2) Phase and amplitude control

both of these approaches are *anticausal*, so they would require future values of the buoy velocity, and are obviously impossible to implement exactly in practice. The alternative is to adopt reasonable approximations and obtain a sub-optimal control for practical use purposes.
The discussed solutions imply that the PTO machinery is able to handle both the resistive and reactive components of the power flow. It is also important to note that eq. A.4 gives a relation to obtain the optimal velocity $u(t)$ of the buoy in order to extract the most energy. Thus, being the future values of the buoy velocity not known a priori, it is not possible to implement an optimal control with the strategies discussed.
The following list of possible control strategies is redacted according to Todalshaug et al. [89] and Ringwood et al. [8]. We have:

- **Resistive Loading (RL)**: this control strategy derives from the assumption that the PTO force is described by

  $$f_{\text{PTO}} = -R_m u(t) \tag{A.6}$$

  in which R is a resistance coefficient of proportionality, while $u(t)$ is the buoy velocity. This assumption is common since many types of PTO machinery can be modeled linearly as a first step in the analysis/design of a system.
  The optimal set for the resistance coefficient, according to [90] ,is

  $$R_{m,\text{opt}}(\omega) = \sqrt{R^2(\omega) + X^2(\omega)} \tag{A.7}$$

  with $R(\omega)$ and $X(\omega)$ being respectively the intrinsic resistance and reactance of the mechanical system.
  The structure of this control law allows the PTO to work only as a generator, thus simplifying the structure of the machinery and its cost. The drawback of this simple model consists in the fact that if the further is the system from resonance conditions, the larger R_m needs to be to optimize the power extraction. This leads to a reduced phase between force and velocity at the price of a redeced amplitude response of the system: the controller works as a *phase and amplitude control.*

- **Approximate Complex-Conjugate Control (ACC)**. This control is based upon the relation

  $$\bar{f}_{\text{PTO,opt}}(i\omega) = -\Lambda_{\text{opt}}(\omega)\bar{u}(i\omega) = -Z^*(\omega)\bar{u}(i\omega) \tag{A.8}$$

  where Z^* is the complex conjugate of the mechanical impedance Z of the system.
  For a monochromatic wave of frequency ω_k we can write the optimal force exerted by the PTO as

  $$f_{\text{PTO,opt}}(t) = (m + m_r(\omega_k))\ddot{x} - R\dot{x} + Sx \tag{A.9}$$

in which m_r and R are the added mass and the resistive coefficient of the mechanical system, respectively.
If we simplify the equation substituting the frequency-dependant values of $m_r(\omega_k)$ and $R(\omega_k)$ with the constants m_c and R_c, using the Laplace transform of the velocity $v(s) = \mathcal{L}(\dot{x})$ it is possible to write

$$m_c s\ v(s) + R_c\ v(s) + S\frac{v(s)}{s} = F_0(s) + F_{\text{PTO}}(s) \tag{A.10}$$

with $F_0(s) = \mathcal{L}(f_{\text{e}}(t))$ and $F_{\text{PTO}}(s) = \mathcal{L}(f_{\text{PTO}}(t))$.

The intrinsic impedance in the domain of Laplace can be expressed by

$$Z(s) = m_c s + R_c + \frac{S}{s} = \frac{m_c s^2 + R_c s + S}{s}. \tag{A.11}$$

In the same way, the PTO machinery impedance may be written as

$$\Lambda(s) = \frac{m_m s^2 + R_m s + S_m}{s} \tag{A.12}$$

the optimal values of the PTO coefficients being $m_m = -m_c$, $R_m = R_c$ and $S_m = -S$ according to the complex conjugate relation.
The optimal PTO force is therefore expressed by

$$F_{\text{PTO,opt}}(s) = -\Lambda_{\text{opt}}(s)v(s) = -\frac{-m_c s^2 + R_c s - S}{s}v(s). \tag{A.13}$$

Substituting eq. A.13 into eq. A.10 we obtain the optimal response velocity

$$v(s) = \frac{F_0(s)}{2R_c}. \tag{A.14}$$

Finally, the general expression of the force-to-velocity transfer function can be written as

$$H(s) = \frac{1}{Z(s) + \Lambda(s)} = \frac{1}{(m_c - m_m)s^2 + (R + R_m)s + (S - S_m)}. \tag{A.15}$$

It is possible to observe that if m_m and S_m are larger than the intrinsic values m_c and S of the system, the coefficients become negative and the system is unstable. Using this simplification, we may choose the coefficients such as to be sure that the poles are not positive and the system is stable.
This can be done by looking at the minimum values of $m + m_r(\omega)$ and S and choosing suitable values of m_m and S_m with an adequate safety margin.
The parameter R_m may be then considered as the parameter that needs to be optimized for each sea state.

- **Tracking of Approximate Optimal Velocity (AVT).** The *optimal phase and amplitude control* mentioned above allows to obtain an expression for the optimal velocity. Thus, the optimization problem may be regarded as a velocity tracking problem.
  The optimal velocity function in the frequency domain may be obtained according to the complex conjugate formulation (as done above in the Laplace domain), and is

  $$v_{\text{opt}}(\omega) = \frac{\bar{f}_0(\omega)}{2R(\omega)}. \tag{A.16}$$

  As done in the previous case, we simplify the expression substituting $R(\omega)$ with the constant R_c, although an approach using a frequency-dependant estimate of $R(\omega)$ is discussed in Perdigão et Sarmento [91] and Falnes [7].
  Having defined the reference signal

  $$v_{\text{opt}}(\omega) = \frac{\bar{f}_0(\omega)}{2R_c} \tag{A.17}$$

  it is possible to track it using a P or PI control law expressed by

  $$H_{\text{PI}}(s) = \beta K_P \frac{1 + T_I s}{1 + \beta T_I s} \tag{A.18}$$

  in which K_P is the proportional gain and T_I is the integrative time constant (equal to zero if the controller is only proportional).

- **Model-Predictive Control (MPC)**. MPC can be applied to the optimization problem of wave energy extraction, as shown in Todalshaug et al. [92] and Faedo et al. [62].
  The principle on which this strategy is based is to optimized the expected behavior of the plant in a brief future time window T_k using a discrete time model of the PTO machinery and a prevision of the force exerted by the incident wave.
  The maximization of the extracted power,under the chosen constraints, is then achieved by using a *Quadratic Programming (QP)* algorithm.
  As the time runs, the time window moves forward, and the QP problem is solved at definite time intervals, allowing the system to always work in the best conditions.

  Schematically MPC is characterized by three features:

  1) A mathematical model of the system, in order to predict the output of the process at future time instants.
  2) An objective function J, in order to be able to optimize the control parameters inside the time window. Such optimization may be subject to constraints or not, and in general, a variety of optimization algorithms can be used (such as QR).
  3) A receding strategy, by which the time window is moved forward at each instant of the discrete-time sequence. Also, only the first time-step of the calculated optimal control sequence is applied at each discrete instant.

Also, MPC allows to control a multivariable system, possibly with different constraints. A simple form of the quadratic objective function used for MPC is

$$J(k) = \sum_{p=1}^{N} (y_{sp}(k+p|k) - \hat{y}(k+p|k))^2 + \lambda \sum_{p=0}^{N-1} (\Delta u(k+p|k))^2 \tag{A.19}$$

in which k represents each iteration of the algorithm, $\mathbf{u}(k) \in \mathbb{R}^{l,N}$, if the system has l controlled variables, is the vector of the future cotrol signals, calculated online at each time step of the discrete time scale. Thus, $\Delta\mathbf{u}(k) = \mathbf{u}(k) - \mathbf{u}(k-1)$ is the increment vector. This vector can be found at each time stem by optimizing the performance function of the system under the defined constraints, and possibly using a penalization term for encouraging the reduction of excessive changes in the controlled variable. This operation is always conducted inside the time window T_k. Also, referring to A.19, λ is a weighting coefficient, $y_{sp}(k+p|k)$ is the set-point value for each sampling instant $k+p$ inside the time window T_k, known at the current instant k, while $\hat{y}(k+p|k)$ is the expected value of the system output, obtained using the mathematical model, calculated at the iteration k for each sampling instant $k+p$.
Finally, it is opportune to define a convex performance function in order to avoid stability issues when optimizing the plant performance.

- **Phase Control by Latching (PML and TUL)**. The logic behind the functioning of Latching control is that the motion of the body is halted every time that its velocity is zero. The body is then released when a certain condition is satisfied. This allows to have a much better accordance betwwen the phase of the buoy velocity and the phase of the wave force compared with the simple RL control.
  If in the case of regular waves it is possible to define the time intervals of latching, being known the wave period, in the case of irregular wave this is not possible, being variable the time between wave peaks.
  A common strategy, proposed by Budal et al. [93] and Babarit et al. [94], consists in predicting the wave profile in a short time window and releasing the buoy $T_0/4$ before the next wave force peak, being T_0 the resonance period. This strategy is called *y peak-matching latching control* (PML) and is focused on aligning the peaks of the wave excitation with those of the velocity.
  An alternative strategy, developed by Falcão [95] and Lopes et al. [96], is not based on predicted values of the wave excitation but on an estimation of the instantaneous excitation force. The principle behind this strategy is that the buoy should be released once the excitation force reaches a certain threshold, thus the method is known as *threshold unlatching control* (TUL). In the case of regular sea states, the results are the same of the PML method, while for irregular sea states, the unlatching instants are generally different.
  The latching control works best if the period $\mathcal{T}$ of the wave is larger than the resonance period of the system T_0, and this condition is usually satisfied when working with heaving point absorbers. Nevertheless, Babarit et al. [94] have shown that Latching control may also be successful in cases in which $\mathcal{T} < T_0$.
  When the body is free to oscillate (unlatched) the PTO machinery resistance R_m is

kept constant, and the value of the resistance coefficient can be optimized for each sea state.
For design/analysis/simulation purposes, there are two main ways of modeling the system: the first one consists in creating two different models, one for the latched state and one for the unlatched state, and to switch between these two; the other method is to introduce an additional resistance R_l when the body is latched, so there is no need to make assumptions on the latching mechanism in this second case.
The latching system may be given by clamping brakes or hydraulic valves or others.
The two aforesaid modeling methods provide the same results if R_l is chosen to be large enough.

- **Phase Control by Clutching (PMC and TUC)**. The Clutching control method is similar to the latching control method involving the switch of the PTO machinery between the values R_m and $R_m + R_l$, with R_l large enough, virtually infinite.
  The main difference is that for the case of the Clutching control the PTO resistance is switched between zero and a constant finite value.
  Although Latching and clutching seem very similar, they lead to different behaviors of the controlled system: in fact, with latching control the power is harvested when the body is moving (unlatched), while with clutching control the power is extracted when the body is slowly sliding damped by the PTO resistance.
  This control strategy for WEC devices has been discussed in Babarit et al. [97].

A.2.1 Final considerations

After having described the most commonly used control strategies for WEC devices, it is possible to observe that almost all of them rely on the prevision of future values of the wave excitation, and a certain degree of knowledge of the functioning of the system, the machinery and the intrinsic parameters. On the other hand, the ES control strategy explored in the present study does not require a knowledge of future values of the wave excitation, and does not take into account the model of the system, being *causal* and *model-free*. The optimization is therefore reached by the definition of the performance function and its maximization by steering the values of the controlled parameters. It is conceivable that, if further studied, analyzed and optimized, ES control may be regarded as one of the most valuable options when controlling a WEC device.

Bibliography

[1] Energy Information Administration, Renewable energy explained, `https://www.eia.gov/energyexplained/renewable-sources/`, Online (2020).

[2] B. Czech, P. Bauer, Wave energy converter concepts: Design challenges and classification, IEEE Industrial Electronics Magazine 6 (2) (2012) 4–16.

[3] OpenEI, Wave Energy, `https://openei.org/wiki/Wave_Energy`, Online (2015).

[4] A. Babarit, Ocean Wave Energy Conversion: Resource, Technologies and Performance, Ocean Wave Energy Conversion: Resource, Technologies and Performance, 2017. `doi:10.1016/C2016-0-01219-6`.

[5] US Department of Energy, Revolution Now, `https://www.energy.gov/revolution-now`, Online (2013).

[6] K. Gunn, C. Stock-Williams, Quantifying the global wave power resource, Renewable Energy 44 (2012) 296–304.

[7] A. Falnes, J., M. R. Perlin, Ocean Waves and Oscillating Systems: Linear Interactions Including Wave-Energy Extraction, Applied Mechanics Reviews 56 (1) (2003) B3–B3. `arXiv:https://asmedigitalcollection.asme.org/appliedmechanicsreviews/article-pdf/56/1/B3/5439484/b1\_1.pdf`, `doi:10.1115/1.1523355`. URL `https://doi.org/10.1115/1.1523355`

[8] J. V. Ringwood, G. Bacelli, F. Fusco, Energy-maximizing control of wave-energy converters: The development of control system technology to optimize their operation, IEEE control systems magazine 34 (5) (2014) 30–55.

[9] J. V. Ringwood, G. Bacelli, F. Fusco, Control, forecasting and optimisation for wave energy conversion, IFAC Proceedings Volumes 47 (3) (2014) 7678–7689.

[10] A. Maria, A. Garrido, E. Rusu, I. Garrido, Addendum: Maria-arenas, a. et al. control strategies applied to wave energy converters: State of the art. energies 2019, 12, 3115, Energies 13 (2020) 1665. `doi:10.3390/en13071665`.

[11] M. Krstić, H.-H. Wang, Stability of extremum seeking feedback for general nonlinear dynamic systems, Automatica 36 (4) (2000) 595–601.

[12] A. Banaszuk, Y. Zhang, C. A. Jacobson, Adaptive control of combustion instability using extremum-seeking, in: Proceedings of the 2000 American Control Conference. ACC (IEEE Cat. No. 00CH36334), Vol. 1, IEEE, 2000, pp. 416–422.

[13] P. Binetti, K. B. Ariyur, M. Krstic, F. Bernelli, Formation flight optimization using extremum seeking feedback, Journal of guidance, control, and dynamics 26 (1) (2003) 132–142.

[14] Y. Li, M. A. Rotea, G.-C. Chiu, L. G. Mongeau, I.-S. Paek, Extremum seeking control of a tunable thermoacoustic cooler, IEEE Transactions on Control Systems Technology 13 (4) (2005) 527–536.

[15] C. Zhang, A. Siranosian, M. Krstić, Extremum seeking for moderately unstable systems and for autonomous vehicle target tracking without position measurements, Automatica 43 (10) (2007) 1832–1839.

[16] M. Bagheri, M. Krstić, P. Naseradinmousavi, Multivariable extremum seeking for joint-space trajectory optimization of a high-degrees-of-freedom robot, Journal of Dynamic Systems, Measurement, and Control 140 (11) (2018).

[17] L. Luo, E. Schuster, Mixing enhancement in 2d magnetohydrodynamic channel flow by extremum seeking boundary control, in: 2009 American Control Conference, IEEE, 2009, pp. 1530–1535.

[18] I. Munteanu, A. I. Bratcu, E. Ceangă, Wind turbulence used as searching signal for mppt in variable-speed wind energy conversion systems, Renewable Energy 34 (1) (2009) 322–327.

[19] D. Shen, P. Khayyer, A. Izadian, Sliding mode extremum seeking control for maximum power point tracking in wind system, in: 2016 IEEE Power and Energy Conference at Illinois (PECI), IEEE, 2016, pp. 1–6.

[20] L. Hu, F. Xue, Z. Qin, J. Shi, W. Qiao, W. Yang, T. Yang, Sliding mode extremum seeking control based on improved invasive weed optimization for mppt in wind energy conversion system, Applied energy 248 (2019) 567–575.

[21] S. L. Brunton, C. W. Rowley, S. R. Kulkarni, C. Clarkson, Maximum power point tracking for photovoltaic optimization using extremum seeking, in: 2009 34th IEEE Photovoltaic Specialists Conference (PVSC), IEEE, 2009, pp. 000013–000016.

[22] H. Zazo, E. Del Castillo, J. F. Reynaud, R. Leyva, Mppt for photovoltaic modules via newton-like extremum seeking control, Energies 5 (8) (2012) 2652–2666.

[23] A. Kebir, L. Woodward, O. Akhrif, Extremum-seeking control with adaptive excitation: Application to a photovoltaic system, IEEE Transactions on Industrial Electronics 65 (3) (2017) 2507–2517.

[24] P. B. Garcia-Rosa, F. Lizarralde, S. F. Estefen, Optimization of the wave energy absorption in oscillating-body systems using extremum seeking approach, in: 2012 American Control Conference (ACC), IEEE, 2012, pp. 1011–1016.

[25] J. Hals, J. Falnes, T. Moan, A comparison of selected strategies for adaptive control of wave energy converters, Journal of Offshore Mechanics and Arctic Engineering 133 (3) (2011).

[26] M. Leblanc, Sur l'electrification des chemins de fer au moyen de courants alternatifs de frequence elevee, Revue générale de l'électricité 12 (8) (1922) 275–277.

[27] V. Kazakevich, On extremum seeking, Moscow High Technical University (1944).

[28] Y. Pan, Ü. Özgüner, T. Acarman, Stability and performance improvement of extremum seeking control with sliding mode, International Journal of Control 76 (9-10) (2003) 968–985.

[29] C. Olalla, M. I. Arteaga, R. Leyva, A. El Aroudi, Analysis and comparison of extremum seeking control techniques, in: 2007 IEEE International Symposium on Industrial Electronics, IEEE, 2007, pp. 72–76.

[30] B. Hunnekens, M. Haring, N. van de Wouw, H. Nijmeijer, A dither-free extremum-seeking control approach using 1st-order least-squares fits for gradient estimation, in: 53rd IEEE Conference on Decision and Control, IEEE, 2014, pp. 2679–2684.

[31] M. A. Haring, Extremum-seeking control: convergence improvements and asymptotic stability, NTNU (2016).

[32] B. Petroleum, Statistical review of world energy, http://www.bp.com/statisticalreview, Online (2019).

[33] F. S.-U. Centre/BNEF, Global trends in renewable energy investment 2017, http://resourceirena.irena.org/gateway/dashboard/, Online (2017).

[34] F. Lafond, A. G. Bailey, J. D. Bakker, D. Rebois, R. Zadourian, P. McSharry, J. D. Farmer, How well do experience curves predict technological progress? a method for making distributional forecasts, Technological Forecasting and Social Change 128 (2018) 104–117.

[35] Ingvald Straume, World map showing wave energy flux in kW per meter wave front, `https://en.wikipedia.org/wiki/File:World_wave_energy_resource_map.png`, Online (2014).

[36] European Marine Energy Center (EMEC), Wave devices, `http://www.emec.org.uk/marine-energy/wave-devices/`, Online (2020).

[37] K. B. Ariyur, M. Krstic, Real-time optimization by extremum-seeking control, John Wiley & Sons, 2003.

[38] C. Zhang, R. Ordóñez, Extremum-seeking control and applications: a numerical optimization-based approach, Springer Science & Business Media, 2011.

[39] R. Janssen, I. E. A. R. E. W. Party, I. E. A. Secretariat, Renewable energy ... into the mainstream, IEA Renewable Energy Working Party, 2002.

[40] M. E. McCormick, Ocean wave energy conversion, Dover Publications, 1981.

[41] Silvio Marcacci, Renewable Energy Job Boom Creates Economic Opportunity As Coal Industry Slumps, `https://www.forbes.com/sites/energyinnovation/2019/04/22/renewable-energy-job-boom-creating-economic-opportunity-as-coal-industry-slumps/`, Online (2019).

[42] S. H. Salter, Wave power, nature 249 (5459) (1974) 720–724. `doi:10.1038/249720a0`.

[43] J. Todalshaug, Hydrodynamics of WECs, Springer, 2017. `doi:10.1007/978-3-319-39889-1_6`.

[44] P. Dafnakis, A. P. S. Bhalla, S. A. Sirigu, M. Bonfanti, G. Bracco, G. Mattiazzo, Comparison of wave-structure interaction dynamics of a submerged cylindrical point absorber with three degrees of freedom using potential flow and CFD models, arXiv preprint arXiv:1908.04981 (2019).

[45] Ocean Power Technologies (OPT), PowerBuoy, `https://oceanpowertechnologies.com/pb3-powerbuoy/`, Online (2020).

[46] Australian Carnegie Wave Enegry Limited, CETO, `https://www.carnegiece.com/projects/`, Online (2020).

[47] Wavebob Ltd., Wavebob, `https://en.wikipedia.org/wiki/Wavebob`, Online (2017).

[48] Wave Hub, Advancing Offshore Renewable Energy, `https://www.wavehub.co.uk/`, Online (2020).

[49] ABC, WA wave energy project turned on to power naval base at Garden Island, `https://www.abc.net.au/news/2015-02-18/wa-wave-energy-project-turned-on-to-power-naval-base/`, Online (2015).

[50] Financial Review, Portland Victoria Wave Farm, `https://archive.is/20130116153339/http://afr.com/p/business/companies/lockheed_martin_woodside_in_wave_My0jdU2iFjWnsq4gT282EK/`, Online (2013).

[51] Alternative energy news, America's premiere wave power farm sets sail, `http://www.alternative-energy-news.info/wave-power-farm-sets-sail/`, Online (2010).

[52] Karen Graham, First wave-produced power in U.S. goes online in Hawaii, `https://apnews.com/06881ff9027c49d99de16bb8df54384a`, Online (2016).

[53] P. Dafnakis, M. Bonfanti, S. A. Sirigu, G. Bracco, G. Mattiazzo, A submerged point absorber wave energy converter for the mediterranean sea, in: Proceedings of the 13th European Wave and Tidal Energy Conference, EWTEC, 2019.

[54] A. Pecher, J. P. Kofoed, Handbook of Ocean Wave Energy, Springer, 2017.

[55] K. Bubbar, B. Buckham, On establishing an analytical power capture limit for self-reacting point absorber wave energy converters based on dynamic response, Applied Energy 228 (2018) 324–338. `doi:10.1016/j.apenergy.2018.06.099`.

[56] K. Bubbar, B. Buckham, P. Wild, A method for comparing wave energy converter conceptual designs based on potential power capture, Renewable Energy 115 (09 2017). `doi:10.1016/j.renene.2017.09.005`.

[57] M. Gradowski, M. Alves, R. Gomes, J. Henriques, Integration of a hydrodynamic negative spring concept into the owc spar buoy, in: Proceedings of the 12th European Wave and Tidal Energy Conference, EWTEC2017, 2017.

[58] A. Price, C. Dent, A. Wallace, On the capture width of wave energy converters, Applied Ocean Research - APPL OCEAN RES 31 (2009) 251–259. `doi:10.1016/j.apor.2010.04.001`.

[59] J. Todalshaug, G. Ásgeirsson, E. Hjálmarsson, J. Maillet, P. Möller, P. Pires, M. Guerinel, M. Lopes, Tank testing of an inherently phase-controlled wave energy converter, International Journal of Marine Energy (05 2016). `doi:10.1016/j.ijome.2016.04.007`.

[60] N. Tom, M. Lawson, Y. Yu, A. Wright, Development of a nearshore oscillating surge wave energy converter with variable geometry, Renewable Energy 96 (2016) 410 – 424. `doi:https://doi.org/10.1016/j.renene.2016.04.016`.
URL `http://www.sciencedirect.com/science/article/pii/S0960148116303081`

[61] U. A. Korde, J. Ringwood, Hydrodynamic Control of Wave Energy Devices, Cambridge University Press, 2016.

[62] N. Faedo, S. Olaya, J. V. Ringwood, Optimal control, mpc and mpc-like algorithms for wave energy systems: An overview, IFAC Journal of Systems and Control 1 (2017) 37–56.

[63] W. Cummins, The impulse response function and ship motions, Tech. rep., David Taylor Model Basin Washington DC (1962).

[64] C.-H. Lee, WAMIT theory manual, Massachusetts Institute of Technology, Department of Ocean Engineering, 1995.

[65] ANSYS AQWA theory manual (2014).

[66] T. Perez, T. I. Fossen, Joint Identification of Infinite-Frequency Added Mass and Fluid-Memory Models of Marine Structures, Modeling, Identification and Control 29 (3) (2008) 93–102. `doi:10.4173/mic.2008.3.2`.

[67] T. Perez, T. I. Fossen, Time- vs. Frequency-domain Identification of Parametric Radiation Force Models for Marine Structures at Zero Speed, Modeling, Identification and Control 29 (1) (2008) 1–19. `doi:10.4173/mic.2008.1.1`.

[68] S. J. Beatty, M. Hall, B. J. Buckham, P. Wild, B. Bocking, Experimental and numerical comparisons of self-reacting point absorber wave energy converters in regular waves, Ocean Engineering 104 (2015) 370 – 386.
`doi:https://doi.org/10.1016/j.oceaneng.2015.05.027`.
URL `http://www.sciencedirect.com/science/article/pii/S0029801815002115`

[69] K. Khedkar, N. Nangia, R. Thirumalaisamy, A. P. S. Bhalla, The inertial sea wave energy converter (ISWEC) technology: device-physics, multiphase modeling and simulations, arXiv preprint arXiv:2005.06108 (2020).

[70] D. DeHaan, M. Guay, Extremum-seeking control of state-constrained nonlinear systems, Automatica 41 (9) (2005) 1567–1574.

[71] M. Guay, E. Moshksar, D. Dochain, A constrained extremum-seeking control approach, International Journal of Robust and Nonlinear Control 25 (16) (2015) 3132–3153.

[72] N. van de Wouw, M. Haring, D. Nešić, Extremum-seeking control for periodic steady-state response optimization, in: 2012 IEEE 51st IEEE Conference on Decision and Control (CDC), IEEE, 2012, pp. 1603–1608.

[73] M. Haring, N. Van De Wouw, D. Nešić, Extremum-seeking control for nonlinear systems with periodic steady-state outputs, Automatica 49 (6) (2013) 1883–1891.

[74] A. Skafte, An introduction to extremum-seeking controlOnline (2017).

[75] M. Rotea, Analysis of multivariable extremum seeking algorithms, in: Proceedings of the 2000 American Control Conference. ACC (IEEE Cat. No. 00CH36334), Vol. 1, 2000, pp. 433 – 437 vol.1. `doi:10.1109/ACC.2000.878937`.

[76] G. Walsh, On the application of multi-parameter extremum seeking control, in: Proceedings of the 2000 American Control Conference. ACC (IEEE Cat. No. 00CH36334), Vol. 1, 2000, pp. 411 – 415 vol.1. `doi:10.1109/ACC.2000.878933`.

[77] A. R. Teel, D. Popovic, Solving smooth and nonsmooth multivariable extremum seeking problems by the methods of nonlinear programming, in: Proceedings of the 2001 American Control Conference.(Cat. No. 01CH37148), Vol. 3, IEEE, 2001, pp. 2394–2399.

[78] K. B. Ariyur, M. Krstic, Multivariable extremum seeking feedback: Analysis and design, in: Proc. of the Mathematical Theory of Networks and Systems, 2002, pp. 12–16.

[79] F. E. Azar, M. Perrier, B. Srinivasan, Real-time global optimization using multiple units, IFAC Proceedings Volumes 42 (19) (2009) 49–54.

[80] U. Ciri, S. Leonardi, M. A. Rotea, Evaluation of log-of-power extremum seeking control for wind turbines using large eddy simulations, Wind Energy 22 (7) (2019) 992–1002.

[81] S. Chen, L. Wang, K. Ma, H. Zhao, A switching-based extremum seeking control scheme, International Journal of Control 90 (8) (2017) 1688–1702.

[82] J. Sternby, Extremum control system: An area for adaptive control?, in: Preprints of Joint American Control Conference, San Francisco, CA, 1980, 1980, p. 8.

[83] H. K. Khalil, Nonlinear systems, 3rd edition, Prentice Hall, Upper Saddle River, NJ, 2002.

[84] R. Leyva, C. Alonso, I. Queinnec, A. Cid-Pastor, D. Lagrange, L. Martinez-Salamero, Mppt of photovoltaic systems using extremum-seeking control, IEEE transactions on aerospace and electronic systems 42 (1) (2006) 249–258.

[85] G. Frantsuzova, Use of a relay controller for automatic extremum seeking in nonlinear systems, Optoelectronics, Instrumentation and Data Processing 47 (2011) 274–280. `doi:10.3103/S8756699011030101`.

[86] B. T. Powell, Investigation of extremum seeking control for adaptive exercise machines, Ph.D. thesis, Cleveland State University (2017).

[87] P. Schmitt, B. Elsäßer, The application of froude scaling to model tests of oscillating wave surge converters, Ocean Engineering 141 (2017) 108 – 115. `doi:https://doi.org/10.1016/j.oceaneng.2017.06.003`.
URL `http://www.sciencedirect.com/science/article/pii/S0029801817302986`

[88] N. Nangia, N. A. Patankar, A. P. S. Bhalla, A DLM immersed boundary method based wave-structure interaction solver for high density ratio multiphase flows, Journal of Computational Physics 398 (2019) 108804.

[89] J. Todalshaug, J. Falnes, T. Moan, A comparison of selected strategies for adaptive control of wave energy converters, Journal of Offshore Mechanics and Arctic Engineering 133 (03 2011). `doi:10.1115/1.4002735`.

[90] J. Hals, T. Bjarte-Larsson, J. Falnes, Optimum reactive control and control by latching of a wave-absorbing semisubmerged heaving sphere, in: Proceedings of the International Conference on Offshore Mechanics and Arctic Engineering—OMAE, OMAE, 2009, pp. 415–423.

[91] J. N. B. A. Perdigão, A. J. N. A. Sarmento, A phase control strategy for owc devices in irregular seas, in: The Fourth International Workshop on Water Waves and Floating Bodies, Department of Mathematics, University of Oslo, 1989, pp. 251–262.

[92] J. Todalshaug, J. Falnes, T. Moan, Constrained optimal control of a heaving buoy wave-energy converter, Journal of Offshore Mechanics and Arctic Engineering 133 (2011) 011401. `doi:10.1115/1.4001431`.

[93] K. Budal, J. Falnes, T. Hals, L. C. Iversen, T. Onshus, Model experiment with a phase controlled point absorber, in: " Proceedings of the Second International Symposium on Wave and Tidal Energy, BHRA Fluid Engineering Cranford, Bedford, 1981.

[94] A. Babarit, G. Duclos, A. Clément, Comparison of latching control strategies for a heaving wave energy device in random sea, Applied Ocean Research 26 (5) (2004) 227 – 238. `doi:https://doi.org/10.1016/j.apor.2005.05.003`.
URL `http://www.sciencedirect.com/science/article/pii/S0141118705000209`

[95] A. Falcao, Phase control through load control of oscillating-body wave energy converters with hydraulic pto system, Ocean Engineering 35 (2008) 358–366. `doi:10.1016/j.oceaneng.2007.10.005`.

[96] M. Lopes, J. Todalshaug, R. Gomes, T. Moan, L. Gato, A. Falcao, Experimental and numerical investigation of non-predictive phase-control strategies for a point-absorbing wave energy converter, Ocean Engineering - OCEAN ENG 36 (2009) 386–402. `doi:10.1016/j.oceaneng.2009.01.015`.

[97] A. Babarit, M. Guglielmi, A. H. Clément, Declutching control of a wave energy converter, Ocean Engineering 36 (12) (2009) 1015 – 1024. `doi:https://doi.org/10.1016/j.oceaneng.2009.05.006`.
URL `http://www.sciencedirect.com/science/article/pii/S0029801809001115`